

**Measurement of Delamination Crack Tip Displacements in G/E  
Laminates Using Scanning Electron Microscopy**

by

Capt. J. Scott Ferguson, C.D.

B.Eng., Royal Military College, 1980

A THESIS SUBMITTED IN PARTIAL FULFILLMENT OF THE  
REQUIREMENTS FOR THE DEGREE OF  
MASTER OF APPLIED SCIENCE

in

THE FACULTY OF GRADUATE STUDIES  
Department of Metals and Materials Engineering

We accept this thesis as conforming  
to the required standard



THE UNIVERSITY OF BRITISH COLUMBIA

February 1992

© J. Scott Ferguson, 1992

In presenting this thesis in partial fulfilment of the requirements for an advanced degree at the University of British Columbia, I agree that the Library shall make it freely available for reference and study. I further agree that permission for extensive copying of this thesis for scholarly purposes may be granted by the head of my department or by his or her representatives. It is understood that copying or publication of this thesis for financial gain shall not be allowed without my written permission.

(Signature)

Department of Metals + Materials Eng.

The University of British Columbia  
Vancouver, Canada

Date 28 Feb 92

## Abstract

A method of measuring delamination crack tip displacements in graphite/epoxy specimens in a Scanning Electron Microscope (SEM) is presented. The technique involves the application of a grid to the specimen edge by evaporating a layer of gold through a thin mesh. The specimens are then placed into a jig which allows the application of Mode I or II loads individually or simultaneously. The specimen is placed into the SEM and a series of photographs are taken from slightly ahead of the crack tip to approximately 800 microns behind the crack tip. The photos are subsequently enlarged to 8"x10" size, and the gold grid then provides a reference system for making measurement of the relative displacements that occur under load.

This method was used to examine the actual crack tip displacement profiles, which were then compared with the profiles that are predicted by Linear Elastic Fracture Mechanics (LEFM). It was found that LEFM was quite accurately able to predict the shape of the profiles, but that the magnitudes were influenced by a number of physical phenomena that were encountered. The measured displacements in Mode I were nearly always smaller than predicted due to the presence of fibre bridging in the specimens. Mode II displacements appeared to be influenced by variations in the local fibre volume fraction of the specimens which resulted in local modulus changes. Mixed-mode testing revealed an interaction that is not predicted by classical LEFM. The addition of a small Mode I load to a Mode II load resulted in increased shear displacements in nine of ten cases. The addition of a Mode II load to a Mode I load, however, resulted in increased, decreased or unchanged opening displacements. Examination of the displacements at the crack starter insert, prior to any

crack growth, indicated that its behaviour is distinctly different than an actual crack. This is most likely due to the presence of a large resin pocket, which forms during manufacture at the end of the insert .

## Table of Contents

<u>Section</u>	<u>Title</u>	<u>Page</u>
	Abstract .....	ii
	Table of Contents .....	iv
	Table of Figures .....	vii
	Table of Tables .....	xii
	Table of Nomenclature .....	xiii
	Acknowledgement .....	xv
1	Introduction .....	1
1.1	Background .....	1
1.2	Motivation .....	3
1.3	Objectives .....	3
2	Theoretical Foundation .....	4
2.1	Linear Elastic Fracture Mechanics .....	4
2.2	Basic Pure Mode Equations .....	8
2.2.1	Mode I .....	8
2.2.2	Mode II .....	11
2.2.3	Corrections to the Pure Mode Equations .....	12
2.2.3.1	Corrections for Crack Tip Rotation and Deflection ...	12
2.2.3.2	Corrections for Large Displacements and End Block Tilting	13
2.2.3.3	Correction of the Compliance .....	14
2.2.3.4	Corrected Equations .....	14
2.2.3.4.1	Mode I .....	14
2.2.3.4.2	Mode II .....	15
2.3	Orthotropic Equations .....	15
3	Previous Work .....	18

3.1	Mode I .....	18
3.2	Mode II .....	23
3.2.1	Factors Affecting Fracture Energies .....	23
3.2.2	Friction .....	24
3.3	Mixed-Mode .....	25
3.4	Methods for Directly Observing Crack Tip Behaviour ....	29
4	Experimental Method .....	32
4.1	Test Specimens .....	32
4.2	Grid Application .....	32
4.3	Loading Method .....	33
4.4	Data Acquisition .....	33
4.4.1	Alternate Method Attempted .....	35
4.5	Data Reduction .....	36
4.6	R-Curve Measurement .....	39
4.7	Experimental Issues .....	39
4.7.1	Specimen Variability .....	40
4.7.2	Material Properties .....	42
4.7.3	Specimen Preparation and Loading .....	43
4.7.3.1	Grid Application .....	43
4.7.3.2	Delamination Growth .....	43
4.7.3.3	Loading .....	44
5	Results and Discussion .....	46
5.1	Results of Pure Mode Tests .....	46
5.1.1	Shape of the Mode I Displacement Singularity .....	46
5.1.2	Shape of the Mode II Displacement Singularity .....	47
5.1.3	Magnitudes of the Mode I Displacements .....	48

5.1.4	Magnitudes of the Mode II Displacements .....	49
5.2	Assessment of Fibre Bridging .....	50
5.2.1	Insert Behaviour .....	52
5.3	Mixed-Mode Tests .....	53
5.4	Other Phenomena Noted .....	54
6	Conclusions .....	56
7	Recommendations .....	58
	References .....	59
	Appendix 1 - Orthotropic Derivation of Sih, Paris and Irwin	63
	Appendix 2 - $G_{II}$ Corrections for Base Deflection .....	70
	Appendix 3 - Equations for $A_I$ and $A_{II}$ as a function of $V_f$ ...	74

## Table of Figures

<u>Figure</u>	<u>Title</u>	<u>Page</u>
1.1	Typical composite laminate .....	78
1.2	Sources of out-of-plane loads .....	78
2.1	Modes of loading .....	79
2.2	Crack tip coordinate system .....	79
2.3	Cracked plate under load .....	80
2.4	Load-displacement curve for fixed load and fixed displacement crack growth	80
2.5	Double Cantilever Beam (DCB) Mode I test specimen .....	81
2.6	Load-displacement plot for determining $G_{IC}$ .....	81
2.7	Flexural specimens used for measurement of $G_{IIC}$ .....	82
2.8	Definition of variables used in Williams corrections .....	83
2.9	Planes of symmetry in a specially orthotropic laminate .....	84
3.1	Composite Mode I delamination resistance as a function of the resin delamination resistance	84
3.2	Fibre nesting in unidirectional laminates .....	85
3.3	Crack tip damage zones in brittle and ductile matrix systems ...	85
3.4	Crack tip stress contour plots in Mode I and II .....	86
3.5	Some mixed-mode test specimen geometries .....	86
4.1	Loading jig used to apply both Mode I and II loads .....	87
4.2	Photograph of an undeformed grid used for measurements ....	88
4.3	Photograph of a deformed grid used for measurements .....	89
4.4	Cross-section photo of specimen 1 (DREP) used to determine fibre volume fraction	92
4.5	Cross-section photo of specimen 4 (NASA) used to determine fibre volume fraction	93
4.6	Variation of resin fraction found in specimen 1 (DREP) .....	94
4.7	Variation of resin fraction found in specimen 4 (NASA) .....	94



4.8	Effect of fibre volume fraction on orthotropic constants $A_I$ and $A_{II}$	96
5.1	Log-log plot of COD vs $r$ for applied $G_I$ of $33.9 \text{ J/m}^2$ on specimen 4 (NASA)	96
5.2	Log-log plot of CSD vs $r$ for applied $G_{II}$ of $349.9 \text{ J/m}^2$ on specimen 7 (DREP)	98
5.3	Plot of COD vs $r$ for an applied $G_I$ of $14.8 \text{ J/m}^2$ on specimen 1 (DREP)	98
5.4	Plot of COD vs $r$ for an applied $G_I$ of $37.5 \text{ J/m}^2$ on specimen 1 (DREP)	99
5.5	Plot of COD vs $r$ for an applied $G_I$ of $74.5 \text{ J/m}^2$ on specimen 1 (DREP)	99
5.6	Plot of COD vs $r$ for an applied $G_I$ of $111.4 \text{ J/m}^2$ on specimen 1 (DREP)	100
5.7	Plot of COD vs $r$ for an applied $G_I$ of $17.6 \text{ J/m}^2$ on specimen 4 (NASA)	100
5.8	Plot of COD vs $r$ for an applied $G_I$ of $33.9 \text{ J/m}^2$ on specimen 4 (NASA)	101
5.9	Plot of COD vs $r$ for an applied $G_I$ of $34.9 \text{ J/m}^2$ on specimen 4 (NASA)	101
5.10	Plot of COD vs $r$ for an applied $G_I$ of $55.4 \text{ J/m}^2$ on specimen 4 (NASA)	102
5.11	Plot of COD vs $r$ for an applied $G_I$ of $6.3 \text{ J/m}^2$ on a DREP .... specimen [49]	102
5.12	Plot of COD vs $r$ for an applied $G_I$ of $26.7 \text{ J/m}^2$ on a DREP ... specimen [49]	103
5.13	Plot of COD vs $r$ for an applied $G_I$ of $63.4 \text{ J/m}^2$ on a DREP ... specimen [49]	103
5.14	Plot of COD vs $r$ for an applied $G_I$ of $103.7 \text{ J/m}^2$ on a DREP .. specimen [49]	104
5.15	Plot of COD vs $r$ for an applied $G_I$ of $19.9 \text{ J/m}^2$ on a DREP ... specimen [49]	104
5.16	Plot of COD vs $r$ for an applied $G_I$ of $39.7 \text{ J/m}^2$ on a DREP ... specimen [49]	105

5.17	Plot of COD vs r for an applied $G_I$ of 67.2 J/m <sup>2</sup> on a DREP ... specimen [49]	105
5.18	Plot of COD vs r for an applied $G_I$ of 109.4 J/m <sup>2</sup> on a DREP .. specimen [49]	106
5.19	Plot of $G_I$ local vs $G_I$ global .....	106
5.20	Plot of CSD vs r for an applied $G_{II}$ of 101.5 J/m <sup>2</sup> on specimen 7 (DREP)	107
5.21	Plot of CSD vs r for an applied $G_{II}$ of 227.1 J/m <sup>2</sup> on specimen 7 (DREP)	107
5.22	Plot of CSD vs r for an applied $G_{II}$ of 349.9 J/m <sup>2</sup> on specimen 7 (DREP)	108
5.23	Plot of CSD vs r for an applied $G_{II}$ of 469.2 J/m <sup>2</sup> on specimen 7 (DREP)	108
5.24	Plot of CSD vs r for an applied $G_{II}$ of 152 J/m <sup>2</sup> on a DREP .... specimen [49]	109
5.25	Plot of CSD vs r for an applied $G_{II}$ of 256 J/m <sup>2</sup> on a DREP .... specimen [49]	109
5.26	Plot of CSD vs r for an applied $G_{II}$ of 395 J/m <sup>2</sup> on a DREP .... specimen [49]	110
5.27	Plot of CSD vs r for an applied $G_{II}$ of 556 J/m <sup>2</sup> on a DREP .... specimen [49]	110
5.28	Plot of $G_{II}$ local vs $G_{II}$ global .....	111
5.29	R-curve measured for a NASA specimen .....	111
5.30	R-curve measured for a DREP specimen .....	112
5.31	Both R-curves plotted together to show different rate of ..... formation of fibre bridges	112
5.32	Plot of COD vs r for two crack lengths on a DREP ..... specimen [49], at approximately the same applied load	113
5.33	Plot of COD vs r for two crack lengths on a DREP ..... specimen [49], at approximately the same applied load	113
5.34	Plot of COD vs r for two crack lengths on specimen 4 ..... (NASA), at approximately the same applied load	114
5.35	Plot of COD vs r for two crack lengths on specimen 7 ..... (DREP), at approximately the same applied load	114

5.36	Plot of COD vs r for two crack lengths on specimen 3 ..... (DREP), at approximately the same applied load	115
5.37	Plot of COD vs r for two different crack lengths in ..... specimens from the same manufacturer, at approximately the same loads	115
5.38	Plot of COD vs r for two different crack lengths in ..... specimens from the same manufacturer, at approximately the same loads	116
5.39	Schematic of fibre bridge under increasing Mode I load .....	116
5.40	Plot of COD vs r for increasing Mode I loads on specimen 6 ... (NASA), at the insert	117
5.41	Plot of COD vs r for decreasing Mode I loads on specimen 6 .. (NASA), at the insert	117
5.42	Plot of COD vs r for increasing Mode I loads on specimen 9 ... (DREP), at the insert	118
5.43	Plot of COD vs r for decreasing Mode I loads on specimen 9 .. (DREP), at the insert	118
5.44	Plot of COD vs r for an applied $G_I$ of $58.6 \text{ J/m}^2$ on specimen .. 6 (NASA), at the insert, showing shape of the displacement field	119
5.45	Plot of COD vs r for an applied $G_I$ of $78.3 \text{ J/m}^2$ on specimen .. 6 (NASA), at the insert, showing shape of the displacement field	119
5.46	Plot of COD vs r for an applied $G_I$ of $44.9 \text{ J/m}^2$ on specimen .. 6 (NASA), at the insert, showing shape of the displacement field	120
5.47	Photograph of the end of the insert in Specimen 6 (NASA) ....	121
5.48	Photograph of the end of the insert in Specimen 9 (DREP) .....	122
5.49	Plot of CSD vs r for pure Mode II and mixed Mode I and II ... loads on specimen 1 (DREP)	123
5.50	Plot of CSD vs r for pure Mode II and mixed Mode I and II ... loads on specimen 3 (DREP)	123
5.51	Plot of CSD vs r for pure Mode II and mixed Mode I and II ... loads on a DREP specimen [49]	124
5.52	Plot of COD vs r for pure Mode I and mixed Mode I and II .... loads on specimen 3 (DREP)	124

5.53	Plot of COD vs $r$ for pure Mode I and mixed Mode I and II loads on specimen 1 (DREP) ....	125
5.54	Plot of COD vs $r$ for pure Mode I and mixed Mode I and II loads on specimen 1 (DREP) ....	125
5.55	Plot of COD vs $r$ for increasing Mode I loads on specimen 7 (DREP) .....	126
5.56	Plot of COD vs $r$ for decreasing Mode I loads on specimen 7 (DREP) ....	126
5.57	Schematic representation of crack closure at the crack tip .....	127
5.58	Plot of CSD vs $r$ for increasing Mode II loads on specimen 7 (DREP) ....	127
A2.1	Schematic showing actual dimensions of reinforced base for the loading jig, and equivalent sections used to calculate deflection corrections ...	128

## Table of Tables

<u>Table</u>	<u>Title</u>	<u>Page</u>
1	Effect on constants of curve fit of COD vs $r^{1/2}+r^{3/2}$ of moving crack tip location	90
2	Effect on the constants of COD vs $r^{1/2}+r^{3/2}$ of changing range over which curve fit is done	91
3	Specimen variations noted for two DREP and one NASA specimens	95
4	Crack front curvatures measured visually after specimens were pulled apart	97

## Table of Nomenclature

$A_i$	elastic constant for mode $i$ from the equations for calculating local value of $G$ from measured displacement
$a$	crack length
$a_{ij}$	plane stress elastic constants
$B$	width of a cantilever beam specimen
$b_{ij}$	plane strain elastic constants
$C$	material compliance
CLS	Cracked Lap Shear specimen geometry
COD	Crack Opening Displacement
CSD	Crack Shear Displacement
DCB	Double Cantilever Beam specimen geometry
DREP	Defence Research Establishment Pacific
$\delta$	applied deflection
$E$	modulus of elasticity
$\epsilon$	strain
ELS	End Loaded Split specimen geometry
ENCB	End Notch Cantilever Beam specimen geometry
$F$	work performed by an external load; also used by Williams as a correction for large displacements and end block effects
$G_i$	strain energy release rate in mode $i$
$G_{ic}$	critical strain energy release rate in mode $i$
G/E	Graphite/Epoxy composite
$h$	half-thickness of a cantilever beam specimen
$I_i$	Williams' interaction parameter for mixed mode loading
$K_i$	stress intensity factor in mode $i$
$L$	length of a cantilever beam specimen

LEFM	Linear Elastic Fracture Mechanics
LVDT	Linear Variable Displacement Transducer
MMF	Mixed Mode Flexure specimen geometry
N	Williams' correction for stiffening due to end blocks
NASA	National Aeronautics and Space Administration
$\nu$	Poisson's ratio
$r$	radial distance from the crack tip
$r_p^*$	radius of the crack tip plastic zone
SEM	Scanning Electron Microscope
$\sigma$	stress
$\sigma_{ys}$	yield stress
$\theta$	radial angle from the crack plane with zero being ahead of the crack tip
U	stored elastic energy
u	displacement in the x (1) direction
v	displacement in the y (2) direction
$V_f$	volume fraction of fibres in a composite
WDX	Wavelength Dispersive X-ray analysis
$\chi$	Williams' correction for crack tip rotation and deflection

LEFM	Linear Elastic Fracture Mechanics
LVDT	Linear Variable Displacement Transducer
MMF	Mixed Mode Flexure specimen geometry
N	Williams' correction for stiffening due to end blocks
NASA	National Aeronautics and Space Administration
$\nu$	Poisson's ratio
$r$	radial distance from the crack tip
$r_p^*$	radius of the crack tip plastic zone
SEM	Scanning Electron Microscope
$\sigma$	stress
$\sigma_{ys}$	yield stress
$\theta$	radial angle from the crack plane with zero being ahead of the crack tip
U	stored elastic energy
u	displacement in the x (1) direction
v	displacement in the y (2) direction
$V_f$	volume fraction of fibres in a composite
WDX	Wavelength Dispersive X-ray analysis
$\chi$	Williams' correction for crack tip rotation and deflection



### Acknowledgement

The author would like to take the opportunity to express his appreciation to the people who played a part in the experimentation and writing that went into this work. To Dr. Anoush Poursartip, without whose wisdom and guidance this thesis could not have been done. To Dennis, Roger, Livio, Greg, Katherine and Reza who provided intellectual and technical assistance, and friendship, when it was needed. To Mr. Alan Russell and Mr. Ernie Jensen of DREP, who provided the materials.

And lastly, but most importantly, to my parents, and to my wife Catherine and daughter Robyn, who put up with the long hours and lack of attention. Without their love, support and constant encouragement, this thesis would not have been completed.

# 1 INTRODUCTION

## 1.1 Background

Fibre reinforced composites are proving to be highly versatile fabrication materials for many advanced applications. The most visible applications are in the aerospace industry, where composites are now being used to manufacture entire airframes such as the Beech Starship business aircraft. Weight considerations are of extreme importance in this area since a pound that can be removed from an airframe is another pound of fuel, cargo or passengers that can be carried. As the costs associated with composites manufacture are reduced, other applications such as in the automotive industry will begin to be exploited. In order to be able to expand the use of composite materials into primary structural applications, it is essential that their mechanical response be fully characterized. This requires a detailed understanding of what determines material properties such as strength, stiffness, strain to failure, environmental performance and flaw criticality, and how these properties may be improved.

The issue of flaw criticality is extremely important and one on which much effort is being expended. Any component, whether it is metallic, ceramic or composite, will contain stress raisers. These stress raisers are generally one of two types. They may be flaws which are introduced during the manufacturing process or which result from in-service loading, or they may be stress concentrations which arise from the design of the structure. Given sufficiently high loads or numbers of fatigue cycles these stress concentrations will result in the growth of cracks which will eventually lead to failure of the piece. The designer must make allowance for the presence of these flaws in the design of a structure.

Composite materials exhibit various flaws such as matrix cracking and fibre breakage, but the most commonly encountered damage is the delamination of the layers. The desired mechanical properties of a laminate are achieved through the building up of thin layers (laminae) of fibres impregnated with the matrix material. During the subsequent cure cycle the layers never totally merge into a single unit, but remain separated by very thin resin-rich regions at the locations of the original interfaces. Figure 1.1 shows a typical lay-up pattern with layers oriented at  $90^\circ$  to each other. Delaminations will develop and grow through these resin-rich regions, since they provide paths of least resistance. Delaminations may be initiated in a number of ways. There may be incomplete curing of the matrix or a poor bond resulting from foreign materials in the layup. For example, the simple act of placing a bare hand on the laminate during lay-up leaves sufficient oils behind to degrade the bond and act as an incipient delamination. Another major contributor to the start and growth of delamination is out-of-plane loading of the component. While composite structures are not designed with load paths running through the thickness, this condition may be induced when in-plane loads encounter disruptions within the piece. Figure 1.2 illustrates some of the more common sources from which in-plane loads can generate out-of-plane components.

The method most commonly used to characterize the response of delaminated composites to loading is Linear Elastic Fracture Mechanics (LEFM). In applying LEFM, global parameters such as loads and displacements are measured to determine the state of the delamination in terms of a material property. The property that is used in composite materials is the Critical Strain Energy Release Rate ( $G_C$ ).

## **1.2 Motivation**

In applying LEFM to delamination growth in composites the assumption is made that the conditions predicted from the globally measured parameters are accurate in the region near the crack tip. Since all of the existing data has been gathered under this assumption, it would be of interest to examine the local crack tip conditions under various globally applied loading conditions, and then relate the observed behaviour with that predicted by LEFM.

## **1.3 Objectives**

There are two objectives to this study. The primary objective is to develop a means of quantifying the local behaviour of the crack tip region under load. The secondary objective is to apply this method to evaluating the response of a delamination under mode I, mode II and mixed I and II loading, and compare the experimentally measured conditions to those predicted by LEFM.

## 2 THEORETICAL FOUNDATION

### 2.1 Linear Elastic Fracture Mechanics

The occurrence of low stress fractures in high strength materials, caused by the presence of stress concentrations, has led to the development of the field of fracture mechanics. Since the strength of a material will be reduced by the presence and growth of flaws, it is important to be able to predict the manner in which they can be introduced and grown. Through the application of the principles of fracture mechanics, it is possible to predict the behaviour of a structure under a given set of conditions. These conditions include flaw size, type and location, as well as the loading spectrum (magnitude, direction and frequency) and the material. Broek [1] states that fracture mechanics should be able to answer the following questions concerning the suitability of a structure for a given application:

- a) what is the residual strength as a function of crack size?;
- b) what size of crack can be tolerated at the expected service load (critical flaw size)?;
- c) how long does it take for a crack to grow from a certain initial size to the critical size?;
- d) what size of pre-existing flaw can be permitted at the moment the structure enters service, or conversely what size of flaw may be expected due to the manufacturing process?; and
- e) how often should the structure be inspected for cracks, based on the limits of Quality Control and Non-Destructive Inspection methods?

The simplest application of fracture mechanics is on materials which exhibit a global response to loading which is linear and elastic. This methodology is therefore referred to as Linear Elastic Fracture Mechanics (LEFM). Fibre reinforced epoxy composites generally exhibit linear elastic behaviour and so LEFM is used to characterize their delamination resistance to external loads. In applying LEFM to composites, certain assumptions are inherent. These assumptions have been stated by Rybicki et. Al. [2] as:

- a) the material behaviour is in fact linear and elastic, with little or no plasticity;
- b) there is a single dominant flaw;
- c) the growth of the flaw is self-similar in nature; and
- d) the material is homogeneous on some scale along the plane of the crack.

The first three of the assumptions are self-explanatory, but the last one may be re-phrased as meaning that the material behaves homogeneously on the length scale over which the stresses are changing, particularly in the vicinity of stress raisers.

In LEFM the loads, and the resulting stresses, are partitioned into three modes as defined in Figure 2.1. While the general cases of loading that are often encountered in structures will involve the superposition of all three, it is necessary to understand the material behaviour under each mode separately. It is well known that flaws or discontinuities, such as cracks and delaminations, will act as stress concentrations since the load must be redistributed around them. The elastic stress field at the tip of a crack or delamination is described by the following equation [1]:

$$\sigma_{ij} = \frac{K}{\sqrt{2\pi r}} f_{ij}(\theta) \quad (2.1)$$

where  $\sigma_{ij}$  is the stress acting on an area of material,  $dx dy$ , at a distance  $r$  from the crack tip and an angle  $\theta$  from the crack plane, with  $f_{ij}(\theta)$  being a known function of  $\theta$ . This is shown in Figure 2.2.  $K$  is called the stress intensity factor, and a stress intensity factor is defined for each mode of loading present. The stress intensity factor can be used as a criterion for determining whether crack growth will occur under a particular loading condition. This critical value of the stress intensity factor is called the material fracture toughness.

The stress intensity factor is a similitude parameter in LEFM, which is to say that for two bodies of the same material but different dimensions, if the stress intensity factor is the same, the crack will behave in the same manner. Another similitude parameter is derived from the Griffith criterion for crack growth. In this case an energy balance is carried out on the system to determine if there is sufficient energy available for crack growth to occur.

Figure 2.3 illustrates a cracked plate which is subjected to a load. The Griffith criterion for growth of this crack is:

$$\frac{d}{da}(F - U) = \frac{dW}{da} \quad (2.2)$$

where  $U$  is the elastic energy stored in the plate,  $F$  is the work performed by the external load and  $W$  is the energy required for crack growth. The left hand side of (2.2) is defined as  $G$ , while the right hand side represents the material resistance to crack growth. Figure 2.3 shows that the load

application points will undergo a relative displacement  $v$ , due to the load. As the crack grows by an increment of length,  $da$ , the displacement will increase by an amount  $dv$ . This means that the work done by the external force will be  $Pdv$ . The expression for  $G$  then becomes:

$$G = \frac{d}{da} (F - U) = \frac{1}{B} \left( P \frac{dv}{da} - \frac{dU_t}{da} \right) \quad (2.3)$$

where  $B$  is the thickness of the plate, and  $U_t$  is the total elastic energy in the plate. If there is no crack growth the relative displacements are elastic and  $v$  will be proportional to the load.  $C$  is the compliance of the plate and is defined as  $C=v/P$ . The elastic energy stored in the plate will be given by:

$$U_t = \frac{1}{2} P v = \frac{1}{2} C P^2 \quad (2.4)$$

By substituting (2.4) into (2.3)  $G$  becomes:

$$G = \frac{1}{B} \left( P^2 \frac{\partial C}{\partial a} + C P \frac{dP}{da} - \frac{1}{2} P^2 \frac{\partial C}{\partial a} - C P \frac{dP}{da} \right) = \frac{P^2}{2B} \frac{dC}{da} \quad (2.5)$$

This strain energy that is released during crack growth is consumed in breaking molecular bonds, creating new surfaces and performing plastic work. There are two conditions under which crack growth can occur. These cases are shown on the load versus displacement graph shown in Figure 2.4. Consider the case of a steadily increasing displacement being applied on the path OA. In the situation where this displacement is then fixed, the only way in which the energy can be delivered to the crack is through the release of elastically stored energy. As the crack grows under these



conditions the load will decrease until the energy available is no longer sufficient to drive the growth, at which point crack arrest occurs. This is along path AC. The value of  $G$  is then defined as the area OAC. In the case where the load is maintained during growth then this external load does work on the crack to make it grow and the path will be AB. In this case the value of  $G$  will be the area OAB. In the limit as the increment of crack growth becomes infinitesimal, the area ABC will become negligible and the value of  $G$  will be the same under the two conditions.

As with  $K$ , there is a strain energy release rate defined for each mode of loading. The general expression for  $G$  is later adapted for the particular specimen being considered by inserting the appropriate expression for the rate of change of compliance with crack length.

## 2.2 Basic Pure Mode Equations

### 2.2.1 Mode I

The geometry most commonly used for measuring the resistance of composite laminates to delamination growth under Mode I loading is the Double Cantilever Beam (DCB) specimen. Figure 2.5 shows the general configuration of the specimen, and illustrates its similarity to the traditional cantilever beam used in mechanics of materials analyses. It can be seen that by loading each arm of the specimen in opposite directions the tendency will be for the delamination to grow and the specimen will peel apart. The most common method for introducing the load is to adhesively bond end blocks to the top and bottom surfaces at the cracked end. These blocks have holes in them so that a pin can be inserted and a load applied. The applied load and deflection are measured as well as the crack length. From these measurements, the compliance,  $C$  and then  $\frac{dC}{da}$  can be calculated. In order to determine the critical strain energy release rate ( $G_{Ic}$ ), a series of tests are conducted

where the load is increased, under displacement control, until the crack grows and the load drops off. The specimen is then unloaded, the crack length determined and the process is repeated. Figure 2.6 shows a load vs. displacement plot for just such a series of tests. After testing, a plot of compliance as a function of crack length will give the slope from which  $G_{Ic}$  can be calculated.

This method will only provide the value of the critical strain energy release rate,  $G_{Ic}$ . It is also desirable to be able to determine  $G_I$  at any applied load prior to the critical value. To calculate  $G_I$  the term  $\frac{dC}{da}$  must be evaluated analytically. This evaluation is done using classical beam theory to derive an expression for compliance. For the DCB specimen this expression is [1]:

$$C = \frac{8a^3}{Eb h^3} \quad (2.6)$$

When substituted into equation (2.5) and simplified, this gives:

$$G_I = \frac{12P^2 a^2}{EB^2 h^3} \quad (2.7)$$

Equation (2.7) requires the measurement of the globally applied load for the calculation of  $G_I$ . In some instances it may be more advantageous to measure the global deflection of the specimen to determine  $G_I$ . An expression for  $G_I$  in terms of deflection can be determined using  $P=\delta/C$ , along with equation (2.6), to find  $P$  in terms of  $\delta$ . When substituted into equation (2.7) this gives:

$$G_I = \frac{3Eh^3 \delta^2}{16a^4} \quad (2.8)$$

Equations (2.7) and (2.8) allow for the calculation of the mode I strain energy release rate.  $G_I$  can then be related to a displacement field by the following method. The general equations for the two dimensional plane stress mode I displacements as a function of the stress intensity are [3]:

$$\begin{Bmatrix} u \\ v \end{Bmatrix} = \frac{K_I 2(1+\nu)}{E} \sqrt{\frac{r}{2\pi}} \begin{Bmatrix} \cos \frac{\theta}{2} \\ \sin \frac{\theta}{2} \end{Bmatrix} \left( \frac{2}{1+\nu} - \cos^2 \frac{\theta}{2} \right) \quad (2.9)$$

The relationship between  $G_I$  and  $K_I$  for the plane stress condition is:

$$G_I = \frac{K_I^2}{E} \quad (2.10)$$

And when (2.10) is rearranged and substituted into (2.9) we get:

$$\begin{Bmatrix} u \\ v \end{Bmatrix} = 2(1+\nu) \sqrt{G_I} \sqrt{\frac{r}{2\pi E}} \begin{Bmatrix} \cos \frac{\theta}{2} \\ \sin \frac{\theta}{2} \end{Bmatrix} \left( \frac{2}{1+\nu} - \cos^2 \frac{\theta}{2} \right) \quad (2.11)$$

We will be interested in the displacements that occur on the crack faces, at  $\theta=180^\circ$ , such that  $u=0$ . The relative displacement in each arm of the DCB specimen is given by  $v$ , so the crack opening displacement is defined as twice the vertical displacement, and is:

$$COD = 2v = 8 \sqrt{\frac{G_I}{E}} \sqrt{\frac{r}{2\pi}} \quad (2.12)$$

### 2.2.2 Mode II

Whereas in Mode I the DCB specimen is almost exclusively used, there have been several different specimen geometries developed for Mode II loading. Figure 2.7 illustrates a number of them. The flexural specimens are the most widely used and their beam theory analysis is well documented. These specimens are subjected to both flexural loading and transverse shear and each of these mechanisms provide part of the crack driving force. The transverse shear causes distortion of the cross section, while the flexural load results in compressive stresses in the upper half of each beam and tensile stresses in the lower half. The discontinuity in stress at the crack tip results in an interlaminar shear stress singularity. In this investigation, the End-Notch Cantilever Beam (ENCB) specimen, also known as the End Loaded Split (ELS), as attributed to Bradley in Figure 2.7, is used for Mode II testing.

The beam theory expressions for  $C$  and  $G_{II}$  for the ENCB specimen are [4]:

$$C = \frac{L^3 + 3a^3}{2EBh^3} \quad (2.13)$$

$$G_{II} = \frac{9P^2a^2}{4EB^2h^3} = \frac{9\delta^2a^2Eh^3}{(L^3 + 3a^3)^2} \quad (2.14)$$

The mode II displacement field may be determined from  $G_{II}$  by starting with the equations [3]:

$$\begin{Bmatrix} u \\ v \end{Bmatrix} = \frac{K_{II}2(1+\nu)}{E} \sqrt{\frac{r}{2\pi}} \begin{Bmatrix} \sin \frac{\theta}{2} \left( \frac{2}{1+\nu} + \cos^2 \frac{\theta}{2} \right) \\ -\cos \frac{\theta}{2} \left( \frac{2}{1+\nu} - 2 + \cos^2 \frac{\theta}{2} \right) \end{Bmatrix} \quad (2.15)$$

In this case the term for  $v$  will be equal to zero on the crack faces, and since  $u$  is the displacement in only one of the arms of the specimen the CSD is defined as twice the horizontal displacement. By making the substitution for the relationship between  $K_{II}$  and  $G_{II}$ , we arrive at the expression for the CSD:

$$CSD = 2u = 8 \sqrt{\frac{G_{II}}{E}} \sqrt{\frac{r}{2\pi}} \quad (2.15)$$

### 2.2.3 Corrections to the Pure Mode Equations

Equations (2.6), (2.7), (2.13) and (2.14) have been derived using the simplest of strength of materials approaches. The crack tip region is modelled as the built-in end of a cantilever beam and a number of assumptions are implicit. Not all of these assumptions are entirely satisfied by composite laminates and a number of researchers have attempted to modify the simple beam theory analyses to better model the true behaviour. We present the results from Williams [5] who has developed advanced analyses of both the DCB and the ENCB specimens which take into account the rotation and deflection which occurs at the crack tip, the effects of large displacements encountered during testing, and the stiffening effects due to the bonded end blocks. He has derived three correction factors to account for these phenomena.

#### 2.2.3.1 Correction for Crack Tip Rotation and Deflection

Williams has shown that the end rotation effect can be accounted for by adding a length  $\chi h$  to the measured crack length. These corrections for beam root distortion and rotation are based on the analysis of Kanninen [6] who modified the double cantilever beam theory analysis to account for the fact that the crack tip is not a built in end, but rather acts as an elastic foundation with a specified stiffness per unit length of uncracked specimen.  $\chi$  can be determined experimentally or calculated from the material elastic properties as:

$$\chi = \sqrt{\frac{E_{11}}{11G_{12}}} \left[ 3 - 2 \left( \frac{\Gamma}{1 + \Gamma} \right)^2 \right]^{\frac{1}{2}} \quad (2.16)$$

$$\Gamma = \frac{1.18(E_{11}E_{22})^{\frac{1}{2}}}{G_{12}} \quad (2.17)$$

### 2.2.3.2 Correction for Large Displacements and End Block Tilting

Large displacements often result in upward curvature of the load-displacement curve, which is indicative of beam stiffening. Williams attributes this to the effective shortening of the beam length that is occurring. This is accentuated in cases where end blocks are used due to the tilting of the blocks. This can be accounted for with a multiplying factor which corrects the calculated G:

$$F = 1 - \Theta_1 \left( \frac{\delta}{L} \right)^2 - \Theta_2 \left( \frac{\delta l_1}{L^2} \right) \quad (2.18)$$

where the terms  $\Theta_1$ ,  $\Theta_2$  and  $l_1$  are defined in Figure 2.8. For the DCB specimen  $L=a$

### 2.2.3.3 Correction of the Compliance

There is a stiffening caused if the loads are introduced through end blocks. As a result, the measured compliance is less than it should be, but this can be corrected for by the use of a multiplication factor:

$$N = 1 - \Theta_3 \left( \frac{l_2}{L} \right)^3 - \Theta_4 \left( \frac{\delta l_1}{L^2} \right) - \Theta_5 \left( \frac{\delta}{L} \right)^2 \quad (2.19)$$

where the terms  $\Theta_3$ ,  $\Theta_4$ ,  $\Theta_5$  and  $l_2$  are also defined in Figure 2.8. In this instance,  $L$  is the total length of the cantilever from the support to the load point.

### 2.2.3.4 Corrected Equations

When applied to the respective formulas for compliance and strain energy release rate, the corrected expressions become:

#### 2.2.3.4.1 Mode I

$$C = \frac{N8(a + \chi h)^3}{EBh^3} \quad (2.20)$$

$$G_I = \frac{12FP^2(a + \chi h)^3}{EB^2h^3} \quad (2.21)$$

#### 2.2.3.4.2 Mode II

$$C = \frac{N[(L + 2\chi h)^3 + 3(a + \chi h)^3]}{2EBh^3} \quad (2.22)$$

$$G_{II} = \frac{9FP^2(a + \chi h)^2}{4EB^2h^3} \quad (2.23)$$

The Mode I equations given above are the ones that will be used for determining  $G_I$  in the R-curve measurements. For all other tests however, the corrections are not used since the specimens do not have end blocks and the deflections being applied are sufficiently small that the effects are negligible.

### 2.3 Orthotropic Equations

As opposed to an isotropic material which contains an infinite number of planes of symmetry, a unidirectional composite falls into the class of materials known as rectilinearly anisotropic or specially orthotropic. These materials contain two planes of symmetry, the xz and xy planes as defined in Figure 2.9. Sih, Paris and Irwin [7] developed a general set of equations for the crack tip stress fields in anisotropic materials, with emphasis on those containing special orthotropy. The full derivations are contained in Appendix 1, but the resultant equations of interest are presented here.

The displacement fields near the crack tip are given by:



$$COD = 2v = \frac{4}{\sqrt{\pi}} \cdot 2^{\frac{1}{4}} \cdot \left[ \frac{2a_{12} + a_{66}}{2a_{11}} + \sqrt{\frac{a_{22}}{a_{11}}} \right]^{\frac{1}{4}} (a_{11}a_{22})^{\frac{1}{4}} \sqrt{r} \sqrt{G_I} \quad (2.24)$$

and

$$CSD = 2u = 4 \frac{\sqrt{a_{11}}}{\sqrt{\pi}} \cdot 2^{\frac{1}{4}} \cdot \left[ \frac{2a_{12} + a_{66}}{2a_{11}} + \sqrt{\frac{a_{22}}{a_{11}}} \right]^{\frac{1}{4}} \sqrt{r} \sqrt{G_{II}} \quad (2.25)$$

where  $a_{ij}$  are the plane stress elastic constants for the laminate:  $a_{11}=1/E_1$ ,  $a_{22}=1/E_2$ ,  $a_{12}=-\nu_{12}/E_1$  and  $a_{66}=1/G_{12}$ .

Thus we have a means of predicting the shape and magnitude of the displacement fields based on the values of strain energy release rate and elastic constants determined from globally measured loads or displacements. These equations can be rewritten as:

$$COD = \alpha_I \sqrt{r}; \quad \alpha_I = A_I \sqrt{G_I} \quad (2.26)$$

$$CSD = \alpha_{II} \sqrt{r}; \quad \alpha_{II} = A_{II} \sqrt{G_{II}} \quad (2.27)$$

where:

$$A_I = 4 \cdot (2)^{\frac{1}{4}} \cdot \frac{(a_{11}a_{22})^{\frac{1}{4}}}{\sqrt{\pi}} \cdot \left[ \frac{2a_{12} + a_{66}}{2a_{11}} + \sqrt{\frac{a_{22}}{a_{11}}} \right]^{\frac{1}{4}} \quad (2.28)$$

$$A_{II} = 4 \cdot (2)^{\frac{1}{4}} \cdot \sqrt{\frac{a_{11}}{\pi}} \cdot \left[ \frac{2a_{12} + a_{66}}{2a_{11}} + \sqrt{\frac{a_{22}}{a_{11}}} \right]^{\frac{1}{4}} \quad (2.29)$$

In this form, equations (2.26) and (2.27) can be used to predict the magnitudes of the displacements based on the globally applied strain energy release rates. These predictions can then be compared with the displacements measured using the SEM technique to be described later.

### 3 PREVIOUS WORK

As was previously described, there are three modes of loading that can be applied to a delamination. In current applications of composites the most commonly encountered conditions involve modes I, II and mixed I and II. There has been very little work done on mode III loading and so this mode is not being considered in this work.

#### 3.1 Mode I

The critical strain energy release rate is a material property and as such is a valuable quantity for ranking different composites on a common scale. As with any measured property, it is essential that the test conditions are consistent from one researcher to another. Various investigators have encountered physical conditions which affect the values of the critical strain energy release rate obtained for mode I. It has been found that the moisture content of the specimen and the temperature at which the tests are conducted have a marked effect on the value obtained for  $G_{IC}$ . Russell and Street conducted two sets of tests on the same carbon fibre reinforced epoxy material to study the effects of temperature and moisture content. In one set of tests [8] there was no change in  $G_{IC}$  with increasing moisture content, while increasing temperature resulted in a decrease of about 20% in the value of  $G_{IC}$ . In the other set of tests [9] a similar temperature effect was found, but the higher moisture content specimens had  $G_{IC}$  values about 10% higher than the dry specimens. In tests on a toughened resin system, Shah et. al. [10] found that increasing the temperature increased  $G_{IC}$  by 20%, while increasing the moisture content increased  $G_{IC}$  by 10%.

The type of matrix material used will also have an influence on the delamination resistance of the composite. It would be expected that using higher toughness resins will result in a composite

with a higher toughness. Test results [10,11] have confirmed this trend, but it was also found [11] that there is a limit to the amount that the delamination fracture resistance of the composite can be increased by increasing the resin toughness. Figure 3.1 shows a plot of composite delamination fracture toughness, for a variety of composites, as a function of the neat resin fracture toughness. While there is limited data at the higher resin toughnesses, there would appear to be little value in using resins with toughnesses above 3 kJ/m<sup>2</sup>. To understand the reason for this limit one must examine the mechanism which determines the resin toughness. The main method by which a material absorbs energy is through the development of a region of plastically deformed material around the crack tip. The higher the resin toughness, the larger the plastic zone formed. The size of the plastic zone may be estimated using [1]:

$$r_p^* = \frac{K_I^2}{2\pi\sigma_{ys}^2} \quad (3.1)$$

where  $r_p^*$  is the radius of the plastic zone and  $\sigma_{ys}$  is the yield stress of the resin. Typical values for a brittle epoxy resin are  $K_{IC}=0.6$  MPa and  $\sigma_{ys}=65$  MPa. This would result in a plastic zone radius of approximately 14 microns. For a tough thermoplastic resin typical values would be  $K_{IC}=2.7$  MPa and  $\sigma_{ys}=76$  MPa. In this case the radius of the plastic zone would be about 200 microns. The thickness of a perfectly compacted layer in a laminate is typically 125 microns. When fibres are added to the resin they have the effect of constraining the size of the plastic zone. With the small plastic zone which is found in brittle systems, there is little impact from the introduction of the fibres and the resin is allowed to transfer virtually all of its toughness to the composite. In the tougher resins, the plastic zone is constrained and this limits the toughness which can be transferred to the composite. An additional result of the fact that the brittle resins have an extremely small plastic zone is that their overall behaviour then remains linearly elastic, and LEFM is applicable.

Other studies have found that the thickness of the crack starter film will influence the initial values of  $G$ . The general trend is that the thicker the starter film, the higher the initial value of  $G_{IC}$  [15,16]. Another interesting point comes from the work of Davies et. al. [15] where tests were also conducted with specimens that had been pre-cracked in either Mode I or Mode II. In this case the Mode I pre-crack gave the highest value of  $G_{IC}$  while the Mode II pre-crack gave the lowest. It was felt that the thick films acted like a blunt crack and that Mode I pre-cracking caused the initiation of fibre bridging, while the Mode II pre-crack resulted in a well defined crack tip very similar to the thin starter films. The interfacial bond strength between the fibres and the matrix will also affect its resistance to crack growth [17]. Specimen thickness also plays a role in the fracture energy [9,18].

The above emphasizes the importance of maintaining consistent test conditions. Beyond such controllable factors as environment and crack starter thickness, the one phenomenon that has been reported in nearly all Mode I testing is the tendency for unidirectional specimens to develop "fibre bridging" during crack growth [8-10,12,14-24,29]. These bridges are in the form of single and multiple fibres spanning the crack from one face to the other. They may be caused to develop by the fact that the laminae do not remain planar during the curing process. Instead they tend to form wavy interfaces with bundles of fibres from one layer interpenetrating the layers above and below it [29]. Figure 3.2 illustrates this. It has already been shown how the plastic zone developed at the crack tip can be large on the scale of the thickness of a single ply. In the case where the plastic zone grows larger than the interfibre distance, critical stress levels may be reached above or below the crack plane. If this happens then the crack plane will change and bridging fibres will remain. Figure 3.3 compares the cases of a small and large plastic zone in a composite. Various authors have found fibre bridging to be sensitive to the resin toughness, interfacial bond strength and the thickness of the resin-rich region at the interply. The interfacial bond strength should ideally be

just strong enough so that matrix damage just begins before the bond fails, while the thickness of the interply region will be determined by the resin toughness and the size of the process zone that forms during deformation. As the crack continues to grow and the COD increases, these bundles will be debonded from the matrix, subjected to stresses and will eventually break when the stress reaches a sufficient level.

Both of these actions, the formation of the fibre bridges and their subsequent straining, will cause energy to be diverted from the crack tip. This results in an increasing fracture energy with crack length. Typically this R-curve will initially increase rapidly and then become asymptotic to a steady state value [2,9,12,20,25,26]. This steady state value can be significantly higher than the initiation value. As a result it may not be sufficient to report a single value for the critical strain energy release rate, but the initiation and steady state values are needed.

Two studies in particular have been conducted to examine the effects of fibre bridging on the measured values of  $G_{IC}$ . Fibre bridging increases the measured resistance to cracking, which is a desirable effect. But due to the fact that the amount of bridging that develops can vary from one batch to another and even from one specimen to another within the same batch, it is undesirable to have it occur during material characterization testing since this could result in non-conservative estimates. Johnson and Mangalgiri [27] found that the amount of bridging can be reduced by introducing a slight angle between plies during the lay-up. They found that  $3^\circ$  was enough to significantly reduce the amount of bridging, but did not completely eliminate it. Another method that has been tried by Russell [20] is to lay the plies on either side of the center  $0^\circ$  plies at  $90^\circ$ . This will tend to restrict the amount of fibre nesting that occurs in the center plies.

In his investigation of factors affecting the delamination of composites, Russell [8] associated an energy  $G_{br}$  with the bridged fibres. This energy consists of a component due to the peeling of the fibres from the resin, and a component of elastic energy stored in the strained fibre. He derived the following equation to estimate the energy:

$$G_{br} = nl \left( g + \frac{1}{2} \epsilon \sigma A \right) \quad (3.1)$$

where  $n$  is the area density of broken fibres,  $l$  is the mean peel length at fracture,  $g$  is the peel energy per unit length,  $\epsilon$  and  $\sigma$  are the strain and stress in the fibre at fracture and  $A$  is the cross sectional area of the fibres. It would be extremely difficult, however, to determine most of the quantities necessary to calculate this bridging energy. The author uses this equation, combined with his experimental observations to explain some of the behaviour of graphite/epoxy laminates under various loading conditions.

A different method of applying a mode I load is by wedging open the crack faces. Newaz and Ahmad [28] used a small diameter cylindrical rod which was forced into the crack. They found this method to return lower values of  $G_{Ic}$  than the traditional DCB test, but no reason for the difference was proposed. The main advantage of the method is that it avoids the need for corrections for large displacements and end blocks, as required in the traditional test. Glessner et. Al. [29] developed a test jig where the specimen is forced against a stationary wedge incorporating low friction rollers. In this method the only measurement required is the load, and the calculation of strain energy release rate is simply  $G=P/B$ . Another advantage of this technique is that the crack tip remains stationary with respect to any viewing system being used to observe the tip during growth.

## 3.2 Mode II

### 3.2.1 Factors Influencing Fracture Energies

Since any cracked beam which is subjected to a bending moment has a Mode II load imposed, it is equally important to characterize the delamination behaviour in this mode. With brittle resin systems, the Mode II critical strain energy release rate is typically several times that for Mode I. Russell [20] reports a  $G_{IIc}/G_{Ic}$  ratio of about 6.2 for the brittle 3501-6 resin used in the current study. The difference in toughness is related to the way in which the material behaves under the two modes. This is illustrated in Figure 3.4 which shows the size of the damage zone ahead of the crack tip in each. It can be seen that there is a large process zone in Mode II which acts very much like the large plastic zone at the tip of a crack in ductile metals. Large amounts of energy are consumed in creating the damage. What has been found for toughened matrix systems is that the difference between the Mode I and Mode II values is much less dramatic than in the brittle systems. Shah et. al. [10] reported  $G_{IIc}/G_{Ic}$  ratios of 1.5 to 2.4 for 2220-3 and 5245C toughened thermoset resins while Prel et. Al. [18] found a ratio of 1.2 for a PEEK thermoplastic resin.

Mode II values are influenced by many of the same factors as the Mode I values. Static testing of unidirectional carbon/epoxy composites using both the ENF and the ENCB specimens [15,30] revealed that, like the DCB specimen, the thinner the starter film the lower the initiation energy. When Mode I pre-cracks of various lengths were used, Davies et. al. [15] found that the initiation energy was essentially independent of pre-crack length. This will however be influenced by the presence of fibre bridging in the case of extremely long pre-cracks. In testing by O'Brien et. al. [30] specimens were pre-cracked using static and fatigue Mode II loads. They found that the fatigue method was difficult to implement and gave results similar to the static pre-crack. When comparing



the Mode I and Mode II static pre-cracks it was found that the Mode I crack gave a slightly lower energy than the Mode II crack. The authors were unable to offer an explanation as why this should be the case but they felt that the Mode II pre-crack was more accurate in simulating the true conditions in a structure under high shear loading. In a study of glass-fibre epoxy composites using the ENF specimen, Giare [31] noted the existence of an R-curve behaviour similar to that found in Mode I specimens. As the crack is grown the amount of energy required increases. No explanation was offered for this increase.

### 3.2.2 Friction

It is easy to imagine that the application of a Mode II load by bending the cracked end of the specimen will tend to force the crack faces together causing interfacial friction. This friction will oppose the sliding of the faces across each other, increasing the energy required. Gillespie et. al. [32] investigated the effects of friction by conducting a finite element analysis of the ENF specimen. They found that for coefficients of friction up to 0.5, the reduction in  $G_{II}$  calculated is no more than 5%. However, no measured values of an interfacial friction coefficient exist. In an experimental study, Russell and Street [9] estimated the amount of friction by observing the amount of hysteresis that occurred during loading and unloading of ENF specimens. From these observations they concluded that the effect of friction on the calculation of  $G$  based on these loadings was an overestimation of approximately 2%. Mixed-mode testing by Hashemi et. al. [33] showed an increase in the total fracture energy when a small amount of shear load was added to an opening load. The magnitude of the increase varied up to a maximum of about 15%, and they postulated that this increase was due to higher interfacial friction. While it would seem that estimates of frictional effects conducted on a global basis indicate a relatively minor contribution, the local

effect taking place at the crack tip may differ significantly. Localized regions of high friction near the crack tip may lead to highly localized perturbations of the stress and displacement fields, without having any measurable effect on globally measured values such as compliance or hysteresis loops.

### 3.3 Mixed-Mode

Since it is rare that a structure will be subjected to a single mode of loading, recent efforts have turned to characterizing composite performance when subjected to mixed Mode I and II loads. The primary reason for conducting this testing is to derive a failure criterion for the material which will take into account varying amounts of each mode of loading. It would be desirable to have a single equation which is able to predict failure. Thus far a number of different formulas have been proposed which are applicable to specific specimen geometries and materials. A number of test specimen configurations have been developed to simultaneously apply these two modes, as can be seen in Figure 3.5. Some of the configurations, such as the Cracked Lap Shear (CLS) and Mixed Mode Flexure (MMF) rely on eccentricity of the load path to provide the second mode, while the remainder utilize special test jigs to physically apply the two loads. The major drawback with the first two specimens is that in order to achieve different ratios of the two modes you must lay up specimens with different ratios of thicknesses of the two half beams.

Ramkumar and Whitcomb [34] were among the first to attempt to tackle the mixed-mode problem in composite laminates when they used the CLS specimen to characterize the behaviour of the brittle T300/5208 graphite/epoxy system. They measured the value of  $G_{IC}$  separately using the DCB specimen and then applied finite element analysis to decompose the measured total  $G$  from the CLS specimen into its Mode I and Mode II components. Unfortunately, without a value of  $G_{IIC}$  to use, they were unable to propose a single failure criterion but looked at three possibilities:

$$\frac{G_I}{G_{IC}} + \frac{G_{II}}{G_{IIC}} = 1 \quad (3.2)$$

$$\left( \frac{G_I}{G_{IC}} \right)^2 + \left( \frac{G_{II}}{G_{IIC}} \right)^2 = 1 \quad (3.3)$$

$$\left( \frac{G_I}{G_{IC}} \right)^2 + \left( \frac{G_{II}}{G_{IIC}} \right)^2 + \left( \frac{G_I}{G_{IC}} \right) \left( \frac{G_{II}}{G_{IIC}} \right) = 1 \quad (3.4)$$

By inserting the measured Mode I value and the estimated components of load into the formulas they calculated values for  $G_{IIC}$  which varied from 456 to 876 J/m<sup>2</sup>. This study was done with a single Mode I to Mode II ratio.

Russell and Street [9] examined another brittle system of AS1 and HMS fibres in 3501-6 resin, also using the CLS specimen. In this test they examined the effects of temperature and moisture on the fracture energy. They used an equation similar to the first one in the previous study:

$$\left( \frac{G_I}{G_{IC}} \right)^{\frac{m}{2}} + \left( \frac{G_{II}}{G_{IIC}} \right)^{\frac{n}{2}} = 1 \quad (3.5)$$

where m and n are determined through curve fitting of the data. The decomposition of the strain energy release rate may be done through beam theory estimation or by the virtual crack closure technique of finite element modelling. In this work, as well as that of Jurf and Pipes [35] using the Arcan specimen and Johnson and Mangalgiri [23] using the CLS and edge delamination test, it was found that m=n=2 provided a good fit to the data. In a study by Wu [36] however, it was found that m=1 and n=2 was a better fit to the data. While not specifically arriving at a mixed-mode

fracture criterion, the work of Rybicki et. al. [2] would seem to also tend towards the condition of  $n > m$ , since they found that the Mode I component had a larger influence on crack extension than the Mode II component. Benzeggagh et. al. [37] have developed a different mixed-mode specimen wherein the ratio of modes can be varied over a small range, from 44 to 56% Mode II, by changing the specimen free length. Over this range of ratios they found that the behaviour of a glass-fibre epoxy composite showed a dramatic increase in fracture resistance as the Mode II portion was increased. This result differed from those of a previous study in that the magnitude of the increase was much greater. The authors postulate that the large increase was due to the extreme difference in the pure mode critical strain energy release rates,  $230 \text{ J/m}^2$  in Mode I as opposed to  $3000 \text{ J/m}^2$  in Mode II, with an accompanying sensitivity to the amount of Mode I present.

In order to be able to accurately assess the behaviour of materials under mixed-mode loads it is important to be able to determine the individual components that are being applied. The method of decomposing the modes will be determined by the specimen geometry. Numerical methods such as finite element, finite difference, boundary methods and energy calculations depend on certain idealizations of the system to allow them to model the various response variables in the region of interest. Because of these compromises they are not always able to provide the necessary accuracy. Beam theory analysis can be used for several of the specimen geometries, but these global techniques typically have one major drawback in that they cannot account for any interaction that may take place in the presence of the two modes together. This is due to the fact that they rely upon the independent measurement of globally applied loads and displacements to make the calculation of the strain energy release rate in each mode. A further method of analytically assessing a specimen utilizes a ply-by-ply, or sublaminates, technique. It is similar to a finite element analysis in that several plies may be grouped together in areas of lesser interest, corresponding to a coarse element mesh, and in regions where high accuracy is desired the individual plies can be divided

into sub-ply in the same way as a fine element mesh is used near the crack tip. In this method the interlaminar stresses are initially assumed to be unknown, and the enforcement of continuity of displacements and tractions at the ply boundaries will lead to the equations which must be solved. The key to the success of the method rests with the engineering model which is used to analyze the plies or groups of plies. Valisetty and Chamis [38] have used this method to evaluate the stresses and strain energy release rates of the MMF specimen. They were able to estimate the stresses ahead of the crack tip, as well as the total strain energy release rate as a function of crack length.

Hashemi et. al. [33] conducted tests, in pure and mixed-mode conditions, on both thermoset and thermoplastic matrix composites, using both fixed and variable ratio mixed-mode specimens. They used the global beam theory method of partitioning the mixed-mode data, claiming that any method which utilizes stress singularity analyses to predict fracture is invalid due to the small region over which the singularity is dominant. In the cases where mixed modes were present they measured the total critical strain energy release rate, partitioned the data into the individual modes and plotted  $G_I$  vs  $G_{II}$  for various ratios. The resulting curve is the failure locus for that material. They found that for the two systems tested the failure locus was essentially linear in the center portion but that it deviated significantly near the end points (pure  $G_{IC}$  and  $G_{IIC}$ ). The addition of fairly small amounts of Mode I to a Mode II load resulted in a significant lowering of the failure locus, while the addition of small amounts of Mode II to a Mode I load actually resulted in raising the failure locus. They then derived an equation to fit the data, which is of the form:

$$\left( \frac{G_I}{G_{IC}} - 1 \right) \left( \frac{G_{II}}{G_{IIC}} - 1 \right) - I_i \left( \frac{G_I}{G_{IC}} \cdot \frac{G_{II}}{G_{IIC}} \right) = 0 \quad (3.6)$$

where  $I_i$  is an interaction parameter. When  $I_i=1$ , there is a linear relationship, and when  $I_i=0$  there is no interaction and the two modes are entirely independent. In order to be able to fairly closely fit the measured data, they found that it was necessary to make  $I_i$  a function of the proportion of  $G_I$  present, ie. for the epoxy matrix system it was:

$$I_i = 3 - 4 \frac{G_I}{G} \quad (3.7)$$

While for the thermoplastic matrix system it was:

$$I_i = 4 - 3 \frac{G_I}{G} \quad (3.8)$$

### 3.4 Methods for Directly Observing Crack Tip Behaviour

A number of researchers have conducted studies on isotropic, homogeneous materials involving the direct observation of the crack tip in a scanning electron microscope (SEM) during loading and crack growth. Much of the work has been involved with measuring the strain fields ahead of the crack in order to estimate of the associated stress distribution. Theocaris et. al. [39] measured the displacement fields around a crack in a plexiglass specimen as a means of determining the stress intensity factor and COD. So that measurements of the relative displacements before and after loading could be made, they used the electron beam in the SEM to inscribe a pattern of dots in an aluminum coating placed on the edge of the specimen. Photographs of the crack tip were taken at various loads and the measurements were made from these. In a related study, Theocaris

[40] sprayed the aluminum coated edge with a fine powder which then provided the reference points. In both cases the method was able to provide accurate information about the elastic field around the crack tip.

An alternative method of accurately measuring strains in a specimen under load was developed by Kortschot [41] and involves the use of metallic meshes and fibre toggle mechanisms attached to the specimen. In the mesh technique, the specimen edge was coated with a dilute suspension of silver particles in a volatile solvent. When the solvent evaporated, the particles were left behind. A copper mesh with nominal hole spacings of  $65\mu\text{m}$  was then attached to the specimen by gluing one end down, and photos were taken at various loads. Relative distances from pre-selected particles to the edge of the grid holes were measured and converted into strains. The toggle method involves gluing a bent fibre on the specimen edge. As the load is applied, the curvature of fibre will be increased or decreased, and this change can be converted to strain as a function of applied load.

SEM methods have also been extended to observing damage formation and growth in composites. When the SEM is fitted with a motor driven stage and a means of collecting continuous images, then dynamic crack growth and fatigue testing is possible. In a test conducted by Kikukawa et. al. [42] to observe the fatigue crack propagation in a grain-oriented silicon iron plate, a coating of magnesium oxide particles was used to provide the reference points. By observing the movement of the particles it was possible to determine the deformations around the crack tip during loading and unloading of the specimen, as well as the crack growth in each cycle. Another means of applying a reference system to the specimen is through the use of photoresist techniques originally developed for the production of integrated circuits. A thin layer of a light sensitive liquid is put on the specimen. This is then followed by a master grid and the system is subjected to a bright light for a predetermined

period of time. The specimen is then "developed" to remove the unwanted material, leaving the reference grid behind. Mao et. al. [43] used this method to observe the propagation of cracks in brittle materials.

Smith et. al. [44] deposited a grid onto the edge of a specimen through a fine mesh of about  $14\mu\text{m}$  spacing. They were attempting to measure the strains at the tip of a matrix crack in a fibre reinforced composite, and found that the mesh was not fine enough to allow for accurate measurements. Finer grids could be achieved using a method called electron beam lithography. This technique combines the photoresist method with using the SEM to inscribe the specimen edge. An electron sensitive resist is put on the specimen, which is then placed in the SEM where a computer controlled stage is moved in the desired pattern. The unwanted resist is then removed, leaving the reference grid behind. The minimum feature size is a function of the magnification of the SEM, but at 400X magnification grid spacings of  $1\mu\text{m}$  can readily be achieved.



## **4 EXPERIMENTAL METHOD**

### **4.1 Test Specimens**

Tests were conducted on specimens made of 24 unidirectional plies of AS4/3501-6 carbon/epoxy composite manufactured by the Defence Research Establishment Pacific (DREP), and the National Aeronautics and Space Administration (NASA), Langley Research Center. The specimens, as received, had significantly different dimensions. The DREP samples had a nominal thickness of 3.5mm, width of 20mm and length of 115mm. They were manufactured with an embedded teflon crack starter of 30mm length. The NASA specimens, although supposedly made in the same manner as the DREP specimens, had a nominal thickness of only 3mm. The nominal width of the NASA samples was initially 30mm but due to the requirements of the test fixture, they were subsequently trimmed to 20mm. The length was 115mm, and they contained a 45mm teflon crack starter.

### **4.2 Grid Application**

Each specimen is clamped between two plexiglass plates and one edge is polished using standard metallographic techniques, with the final stage being an aqueous suspension of 5 micron alumina. The mesh which is used to create the grid is etched copper with 500 openings to the inch, and a nominal opening size of 27 microns. The grid is applied by attaching a strip of mesh the same width as the specimen to the edge of the specimens using press-on adhesive at each end. Because the center of the strip tends to lift away from the surface, resulting in an indistinct grid, the specimen is then placed into a jig which has a series of 0.102mm wires which can be tightened down across

the mesh. The specimen and jig are then placed into a vacuum evaporator, a vacuum of  $10^{-4}$  torr is established, and a thin layer of gold is evaporated onto the specimen through the mesh. The specimen is then removed from the jig and the mesh is taken off the specimen edge.

### 4.3 Loading Method

A method had been previously developed [45] which allowed for the simultaneous application of mode I and II static loads. This involves a test jig which can hold the specimen while the specimen is wedge loaded with varying numbers of shims, and a bending moment is applied. Figure 4.1 illustrates the configuration of the jig. The entire jig was initially fabricated from aluminum, but it was subsequently found that, due to the high stiffness of the specimens compared to the aluminum, the base of the jig was deflecting when bending moments were applied, resulting in erroneous measurement of the mode II displacements. This was rectified by adding a steel backing plate to the base and calculating its compliance. By knowing the compliance of the base it was then possible to determine the amount of base deflection and correct the mode II loads. The analysis for the bending of the base and the corrections used are contained in Appendix 2. As an example of the magnitude of the errors involved, a  $G_{II}$  of  $614 \text{ J/m}^2$  applied with the aluminum base is corrected to  $556 \text{ J/m}^2$ , while a  $G_{II}$  of  $614 \text{ J/m}^2$  applied to the reinforced base is corrected to  $606 \text{ J/m}^2$ . In percentage terms, the correction for the unreinforced base is 10% and for the reinforced base it is 1.3%.

### 4.4 Data Acquisition

Cracks are grown from the insert by using a Mode I wedge load. Since the wedge tends to disturb the insert, the starter film is generally removed at this time. The specimen is then placed in a Hitachi SEM and an attempt is made to locate the crack tip in the unloaded condition. The tip

is extremely difficult to detect so a series of photos is taken which commence well in advance of the point where the crack is visible, and extend to at least 600 microns behind the tip. These zero load photos are used to determine the distance from the crack tip to the measurement points ( $r$ ), and for determining the distance between measurement points in the unloaded state. From these zero load values COD and CSD are later determined in the loaded case. Also at this time a preliminary measurement of the crack length is made by using the verniers on the SEM stage. At low loads the crack faces near the tip tend to remain closed so it is difficult to observe the actual tip, so this crack length value is continuously updated as the specimen is loaded and the true location of the tip becomes evident. For this study, all photos were taken at a magnification of 500x and a specimen working distance of 25mm. This magnification was selected as a compromise between the highest resolution possible and the number of photographs which could be handled reasonably.

The type of test to be conducted, pure or mixed mode, then determines the method of handling the specimen. The preliminary pure mode I tests are done by wedging the crack open with a number of small pieces of shim stock until a load close to  $G_{IC}$  is reached. A series of SEM photos is then taken at this load, a shim is removed and another set of photos taken at the new load. This is continued until all the shims are removed. In a mixed mode test the specimen is wedge loaded in conjunction with a bending moment. The loading sequence is always: zero load, pure mode I, mixed mode, mixed mode, pure mode II, zero load. In between the two mixed modes, the mode II load is removed and then re-applied and care is taken to ensure that the point of application of the bending moment is directly beneath the end of the wedge load. In a pure mode II test an increasing load is applied by increasing the bending moment and photos are taken at the desired loads.

The SEM photos are subsequently enlarged to 8"x10" size and measurements are then taken from these. Figure 4.2 shows an example of a photo at full magnification. Due to the actual crack

faces frequently being obscured, it is necessary to make COD measurements by determining the difference in distance between surface features which can be found at distances up to 40 microns from the crack face. It was possible to confirm the accuracy of the measurements made by this method by comparing them with measurements taken at the crack face in areas where there was no obscuration. The distance between the selected features is measured in the zero load photos, and this value is subsequently subtracted from the value measured under load to give the COD. CSD's are determined by measuring the relative shift between vertical grid lines which occurs under mode II loading.

#### **4.4.1 Alternate Method Attempted**

An alternative method of collecting the data was attempted before settling with the technique described above. The ideal data collection and analysis method would have involved the use of a PC with a frame grabber and image analysis software. This was not possible with the Hitachi SEM because it uses a scan converter which does not conform to industry standards. However, there is a method by which an image can be taken from the SEM. This involves the use of the KEVEX 8000 Emission Dispersive X-Ray analyser, which has the ability to take over the scan of the SEM and capture a digital image and store it on a removable hard disk. The KEVEX also has some rudimentary image analysis capabilities, including a cursor with a positional readout. By taking an image of an object of known dimensions it is possible to calibrate the cursor steps and then measure displacements in cursor steps, to later be converted into actual measurements. Significant effort was expended on this method but it was eventually discarded for two reasons. Firstly, the image collected by the KEVEX was compressed in the vertical direction as compared to the original picture. Secondly, an excessively high magnification, and hence a very large number of images, were necessary to achieve a reasonable resolution in the measurements.

#### 4.5 Data Reduction

Equations (2.26)-(2.29) have been derived using just the first term of the elastic stress singularity. Since this term is a function of  $r^{-1/2}$  it will dominate in the region close to the crack tip and it is valid to neglect the higher order terms in this region. Since the range over which measurements were made for this study extends up to 800 microns behind the crack tip, one must consider that higher order terms may have an effect. The general expression for the elastic stress field is a polynomial function of  $r$ , and can be written as:

$$\sigma_{ij} = C_1 r^{-1/2} f_{1ij}(\theta) + C_2 r^0 f_{2ij}(\theta) + C_3 r^{1/2} f_{3ij}(\theta) + \dots \quad (4.1)$$

where  $C_n$  are constants which account for the boundary conditions, and  $f_{nij}(\theta)$  are functions of the radial angle from the crack plane. The first coefficient,  $C_1$  is a form of stress intensity factor and is the only term not neglected in the region near the crack tip. It should be noted that the second term of this stress equation is a constant, and will be equal to the far field stresses. In both modes I and II, a boundary condition is that  $\sigma_2$  is zero.

In a similar manner the displacements can be expressed as:

$$u, v = D_1 r^{1/2} g_1(\theta) + D_2 r g_2(\theta) + D_3 r^{3/2} g_3(\theta) + \dots \quad (4.2)$$

where  $D_n$  are constants which account for the boundary conditions and material properties, and  $g_n(\theta)$  are functions of the radial angle from the crack plane. These displacement terms have been

determined by integrating the associated stress terms. In order to maintain as much simplicity in our argument as possible, we will only consider the first two terms of the displacement equations at this time.

In mode I loading, on the crack faces, the shear displacements ( $u$ ) are zero and the vertical displacements are generated by  $\sigma_2$ . The boundary conditions state that the far-field stress will be zero, so the first two terms of the displacement equation will be:

$$COD = 2v = \alpha_I r^{1/2} + \beta_I r^{3/2} + \dots \quad (4.3)$$

where  $\alpha_I$  and  $\beta_I$  are constants which account for the stress intensity and material properties.

In mode II the opening displacements ( $v$ ) are zero on the crack faces and the shear displacements will be generated by  $\sigma_1$ . This means that the second term will be a constant term for the far field stress parallel to the crack plane. Since it is uncertain what the influence of this term is, the first two terms for the displacements could be one of the following two equations:

$$CSD = 2u = \alpha_{II} r^{1/2} + \beta_{II} r \quad (4.4)$$

$$CSD = 2u = \alpha_{II} r^{1/2} + \beta_{II} r^{3/2}$$

Through the application of these equations to the data, it is possible to conduct a curve-fitting exercise, using both one and two term relations, which will yield values for the constants  $\alpha$  and  $\beta$ . The  $\alpha$  constants can in turn be used to determine a strain energy release rate, using Eqns. 2.26 and

2.27, which can be compared with the value determined from LEFM. There are, however, two decisions that must be made in performing the curve fits that can have a significant effect on the results.

The first decision to be made is the location of the crack tip. The position determined by examination of the photos is typically not accurate since it is susceptible to being influenced by features on the specimen surface. Subsequent evaluation of the displacement curves is often sufficient to determine the location to within a few tens of microns, but this apparently small discrepancy can greatly affect the outcome of the curve fit. Table 1 shows the results of a set of curve fits done on a typical set of Mode I data, in which the only thing which was changed was the position of the crack tip. It is readily apparent that by moving the crack tip only 20 microns from -10 to 10, the value of  $\alpha_I$  changes by 15% while  $\beta_I$  changes 86%.

Once the crack tip location has been determined the next decision concerns the region over which the fit should be done. Table 2 contains the values of the curve fit constants which resulted when the fit range was varied from 167.9 microns to 951.5 microns. Once again, relatively small changes to the selected value can result in large variations in the values of  $\alpha_I$  and  $\beta_I$ .

On the basis of the results of this analysis, it was decided that this type of numerical curve-fitting of the data would not be done. Instead, a form of visual curve-fit was used. This involved the superposition of a calculated displacement curve determined using the orthotropic equations previously derived, on the measured data points. Then the crack tip location and the magnitude of the strain energy release rate were varied until a reasonable fit to the data in the first few hundred microns behind the crack tip was achieved. From this a quantity called  $G_{local}$  was determined. For each crack length, once a crack tip position was chosen, it remained fixed for all loadings.

#### 4.6 R-Curve Measurement

The determination of the R-curve behaviour is done by first polishing the edge of a specimen as described above. Two aluminum tabs are then bonded to the sides of the specimen at the end containing the crack starter. These tabs each have a hole drilled in them by which the specimen can be loaded in Mode I in an MTS servo-hydraulic testing machine. Finally, a coating of brittle white correction fluid is applied to the polished edge. This edge is then marked off at 1mm increments from the point of application of the load to a distance of approximately 50mm past the end of the insert.

Testing is then conducted in the MTS under displacement control, with a constant crosshead speed of 0.5mm/min. Throughout the test a PC is used to collect data from the load cell and a Linear Variable Displacement Transducer (LVDT) which monitors the relative movement of the crosshead. The advance of the crack front is monitored using a travelling microscope. As the crack front passes each 1mm mark, a signal is sent to the PC via a hand-held button. In this way it is possible to relate the crack length to the load and displacement data. From the load and displacement the compliance is calculated, and the analysis of Williams [5] is used to determine the increase of  $G_{IC}$  as a function of crack length.

#### 4.7 Experimental Issues

There were a number of areas where difficulties were encountered, or where there was uncertainty as to either repeatability or accuracy of the data. In general, each of these areas is linked to either a step in the specimen manufacture or handling. The sources of these uncertainties are discussed below.



#### 4.7.1 Specimen Variability

Due to the current method of manufacture of composites, there is a certain amount of variability, not just from batch to batch, but also from specimen to specimen in the same panel. The physical characteristics which will tend to vary include the local volume fraction of fibres ( $V_f$ ), the amount of fibre nesting and the thickness of the compacted layers which effects the thickness of the two half beams. The most obvious evidence of this variability is the difference in total thicknesses of the specimens from the two sources (DREP and NASA). This is despite the fact that they are all supposed to have been manufactured using the same materials and method. In order to be able to evaluate the difference in average  $V_f$  between the two sources, photographs of the ends of two specimens were taken. Figures 4.3 and 4.4 show these photographs. After being enlarged, an area method was used to determine  $V_f$  by estimating the area of fibres as a fraction of the total area. It was found that  $V_f$  for the NASA specimen was 0.74, while for the DREP specimen it was 0.66. This is consistent with the noted differences in thickness in that more resin has been removed from the NASA specimens.

It would also be interesting to determine the variation of  $V_f$  through the thickness of the specimen. It was possible to do this using a method called Wavelength Dispersive X-Ray analysis (WDX) in conjunction with the SEM. This technique involves the mapping of the relative concentrations of a selected element, at various locations, using the intensity of the X-rays that are emitted as a result of the electron bombardment as a measure of the amount of the element present [50]. In the case of the 3501-6 resin sulphur was selected as the element to be mapped. The system is first calibrated using a pure sulphur standard, and then a neat resin sample is measured to give the baseline reading of counts per second. The relative quantity of resin is then found by comparing the readings through the thickness with those for the neat sample.

This was done for several specimens and different locations. Figures 4.5 and 4.6 are illustrative of what was found. One is easily able to see the locations of the resin rich regions at the ply interfaces in the specimens. It can be seen that compaction is not uniform and the amounts of resin at the interfaces varies significantly. From Figure 4.5, the value of  $V_f$  for specimen 1 is 0.65, and from Figure 4.6 the  $V_f$  for specimen 4 is 0.76. These values are in good agreement with the optically determined results previously reported.

When the specimens are made, the crack starter is inserted between the twelfth and thirteenth layers and it is assumed that as the specimen is cured the amount of compaction of the layers in the top and bottom halves will be the same. It is on the basis of this assumption that the beam theory equations have been derived. If there is a significant difference in the two thicknesses, then the amount of bending of the beams will not be symmetric. To evaluate the variation of thicknesses in the specimens two DREP and one NASA specimen were selected. The measurements were made using a travelling microscope on a vernier stage at a point as near to the crack tip as possible. The accompanying effect on deflections in Mode I were determined using two methods. The first involved applying a wedge load to the specimen and then tracing the outline. The outlines of the upper and lower surfaces at the uncracked end were then extended and the deviation of the traced lines from the line extensions were measured. The second method involved putting the specimen into the loading jig, measuring the clearance between the bottom of the specimen and the base of the jig, applying a static Mode I load and remeasuring the clearance. This directly gives the deflection of the lower half beam, while the upper deflection is inferred. Table 3 provides a summary of the various measurements for the three specimens.

It can be seen that the thicknesses can vary by as much as 6.4%, as was found in specimen 1. In that case, the bottom beam was the thicker and hence showed a lower deflection than did the

top beam. This is similar to the results for specimen 4, except that the magnitudes of the differences are less. The results from specimen 3 are puzzling in that the measured thicknesses are nearly identical and yet there is a significant difference in deflections. This may be due to the fact that the thickness measurements were taken at a point several millimeters behind the crack tip where it was possible to distinguish the crack under the low magnification of the travelling microscope. The deflections of the beams will be strongly influenced by the relative thicknesses right at the crack tip, and these may have been different than those that were measured.

#### 4.7.2 Material Properties

This variability in the half beam thicknesses and local  $V_f$  will have an accompanying impact on the local elastic behaviour of the composite. This in turn will affect the accuracy of the LEFM predictions. In order to see how great the change in elastic constants would be with variations in local  $V_f$ , an analysis was conducted utilizing a method proposed by Tsai [51]. The details of the analysis are contained in Appendix 3. These estimated elastic moduli were then used in Equations [2.28] and [2.29] to see the variation in  $A_I$  and  $A_{II}$ . The results are contained in Figure 4.7. It can be seen that the variation in  $A_I$  is essentially linear, while for  $A_{II}$  there is a dramatic increase when the value of  $V_f$  falls below about 0.1. From this it would be expected that any local phenomenon which results in a significant variation in the local  $V_f$  will in turn result in a displacement field whose magnitude is different than expected.

### **4.7.3 Specimen Preparation and Loading**

There are a number of potential sources of error that arise during the preparation, handling and loading of the specimens.

#### **4.7.3.1 Grid Application**

Some difficulty was encountered throughout the experiments in achieving a consistently clear grid on the specimen. Due to the tendency of the mesh strip to lift away from the specimen surface the resulting grid contained regions of high clarity with sharp edges near the hold-down wires and less clear areas in between. This problem was not as much of a difficulty in Mode I testing since the surface features being used for the measurements were in focus, but during Mode II tests the poorer the definition of the grid line the greater the uncertainty in the associated measurements. Ensuring that the crack tip was in one of the better regions was not possible. Owing to the amount of discretion being placed on the measurer in ensuring that the same precise points are consistently used for determining displacements it is not possible to conduct a rigorous analysis to determine error bars. Over the course of several hundred photographs and several thousand measurements, a rough estimate of their accuracy would put the error at  $\pm 0.4\text{mm}$  on the photographs, which is equivalent to approximately 0.4 microns of COD or CSD.

#### **4.7.3.2 Delamination Growth**

Delaminations were manually grown using a mode I wedge load. This was typically done with a razor blade being inserted between the crack faces. Despite efforts to ensure that the load was evenly applied across the width of the specimen, there was a tendency for one side to grow further

than the other. This fact could not be determined until the testing on a specimen was completed and it could be ripped apart. At this time the delamination fronts for each of the crack lengths used could be viewed as striations on the specimen surface. Table 4 shows the measured delamination lengths across the specimens. In those instances where there is no center value reported the crack front was a maximum at one edge. In the cases where there is a center value, the front bowed out in the center of the specimen. Front refers to the side of the specimen on which the measurements were taken. It can be seen that the differences in some of the lengths is significant. In these cases the delamination cannot be expected to behave exactly as predicted by LEFM. If the length on the front is longer than the back then the COD's will be smaller than expected. This is due to the fact that the unfractured material will provide a restoring force that opposes the applied load. This was the case in all of the delaminations studied.

This method of growing the delamination will also introduce fibre bridging. In the case of mode I tests this is what would be expected. There has been no reference to fibre bridging in any of the literature concerned with mode II testing, which would imply that it does not normally develop when the delamination is grown under these conditions. It is uncertain what effect this has on the measured CSD's.

#### **4.7.3.3 Loading**

It is important that the jig be made so that the specimen is clamped and the loads are introduced symmetrically. If there is any twisting introduced along the length of the specimen it will result in a different deflection on one side than the other. The end result will be a load which varies across the width of the specimen. In a mode II test there is also the possibility that a mode I component will be induced by this variation of load.

In a mixed-mode test it is essential that the mode II load be applied directly under the end of the mode I wedge. If the mode II is applied farther away from the crack tip then it would tend to pivot the lower arm of the specimen and induce larger COD's than the mode I load alone. If the opposite is true and the mode II is applied nearer to the crack tip, then the tendency will be for the delamination to be closed and the COD's to be smaller. With the jig used for this study the point of application of the loads was done visually to the best ability of the tester.

## **5 RESULTS AND DISCUSSION**

In order to be able to satisfy the motivations of this study a number of related but separate experiments were conducted. The first objective was to determine whether the test method is capable of providing accurate data about crack tip displacements. The second was to assess the applicability of LEFM to predicting these displacement fields. To meet these objectives the form of the displacement singularity and the accuracy of the orthotropic LEFM predictions were determined using pure mode test data. As a result of these findings some additional pure mode testing was conducted in an attempt to answer some further questions that had arisen. The effects of any possible interaction in mixed mode loadings were then examined using a number of specimens, crack lengths and ratios of mixed modes. In addition, comparisons are made to the results of an earlier preliminary study conducted by Poursartip and Gambone [49].

### **5.1 Results of Pure Mode Tests**

#### **5.1.1 Shape of the Mode I Displacement Singularity**

To determine the shape of the displacement field in Mode I, tests were conducted on two specimens. A DREP specimen, designated specimen 1, and a NASA specimen, designated specimen 4. In these tests a series of four wedge loads were used for each specimen, with the loads applied so that the initial strain energy release rates were near the expected critical value and decreasing thereafter. The reason for using decreasing loads as opposed to increasing, was an attempt to limit the influence of any fibre bridging on the magnitudes of the displacements.

Figure 5.1 is a log-log plot of COD as a function of  $r$  behind the crack tip, for a load of  $33 \text{ J/m}^2$  on specimen 4. It is entirely representative of the shape of the displacement field that was found for all eight loads on both specimens. This method of presenting the data was selected since, by plotting a straight line over the data, it is quite easy to determine the slope of the fit as well as the zone of influence of the first term. The straight line represents a slope of  $1/2$ , as would be expected for a stress singularity of order  $r^{-1/2}$ . It can be seen that the data begins to deviate from a slope of  $1/2$  approximately 400 microns behind the crack tip.

### 5.1.2 Shape of the Mode II Displacement Singularity

In a similar manner to that used for Mode I a series of decreasing shear loads was applied to a DREP sample, designated specimen 7. Figure 5.2 shows a log-log plot of CSD as a function of  $r$  behind the crack tip, for a load of  $349.9 \text{ J/m}^2$ . Once again, the straight line has been plotted with a slope of  $1/2$ . It is evident that this line represents a reasonable estimate to the data, and that coincidentally the CSD data also begins to deviate at about 400 microns behind the crack tip.

On the basis of the fact that the displacement singularity that was found is of order  $1/2$ , as is predicted by LEFM, we will conclude that the application of LEFM to this type of composite material is valid. The next point to examine is the accuracy with which the magnitudes of the displacements are predicted.



### 5.1.3 Magnitudes of the Mode I Displacements

At this point, the remainder of the data from specimens 1 and 4 will be presented. Figures 5.3 - 5.10 are the plots of COD vs  $r$  presented on a linear scale. In this form, the expected shape of the  $r^{1/2}$  profile can be seen. Each plot provides the specimen number and the value of  $G_I$  applied, as calculated using equation (2.8). The solid lines have been added using equation (2.24) and the value of  $G_I$  applied. The dashed lines have been plotted using the same equation, however the value of  $G_I$  has been adjusted so that the curve provides a more accurate fit to the data points. This provides us with the value of  $G_{I\text{ local}}$  that was previously mentioned. Six of the eight plots showed a  $G_{I\text{ local}}$  lower than  $G_{I\text{ global}}$ , while in the other two plots the values were the same.

The results of a similar study conducted by Poursartip and Gambone [49] are presented as Figures 5.11 - 5.18. In these plots, four of the eight result in values of  $G_{I\text{ local}}$  lower than  $G_{I\text{ global}}$ , while two plots show the values to be the same and two plots have  $G_{I\text{ local}}$  larger than  $G_{I\text{ global}}$ . The experimental method used in this earlier study was nearly identical to the one presented in this report.

The results of the four sets of tests are presented as a plot of  $G_{I\text{ local}}$  vs  $G_{I\text{ global}}$  in Figure 5.19. The dashed line represents the expected result if the local displacements were exactly as predicted by LEFM. The explanation for the fact that the local displacements were smaller than predicted 10 of the 16 tests may well be a result of fibre bridging, which is often found in Mode I testing of unidirectional specimens. The reason for two of the displacement profiles being higher than expected may also be attributed to fibre bridging, but in a slightly different way. During the course of crack growth under Mode I loading, the fibre bridges will be formed by the pulling out of the fibres from the matrix. These bridges will eventually be strained to the point that either the fibre

breaks, or it is fully peeled from the matrix. This process results in debris being formed on the crack faces and it is possible that, at low loads, the presence of debris near the crack tip will result in the crack faces remaining wedged apart.

### 5.1.4 Magnitudes of the Mode II Displacements

The CSD vs  $r$  data for specimen 7 is presented as Figures 5.20 - 5.23. It can be seen that the value of  $G_{II\text{ local}}$  is lower than  $G_{II\text{ global}}$  in all four plots, and that the difference increases significantly as the load is increased from being 59% of  $G_{II\text{ global}}$  at a load of  $101\text{ J/m}^2$  to being only 32% of  $G_{II\text{ global}}$  at a load of  $469\text{ J/m}^2$ . In this set, the data presented is, as always, for decreasing loads.

Figures 5.24 - 5.27 present the data of the earlier study [49]. In this set of data, the value of  $G_{II\text{ local}}$  is consistently twice the value of  $G_{II\text{ global}}$ . Figure 5.28 is a plot of  $G_{II\text{ local}}$  vs  $G_{II\text{ global}}$ . This apparently large discrepancy between data is puzzling since the source of the specimens and the test procedures were identical in respects, including the fact that the loads were decreasing. One possible explanation for this difference lies in the local fibre volume fraction. Referring back to Figure 4.7 we will recall that the value of  $A_{II}$  is inversely related to  $V_f$ , and that there is a significant increase in the value of  $A_{II}$  at volume fractions less than 0.15. Thus, if the local volume fractions of the two specimens vary dramatically, then it would not be unusual that the local displacement fields would also differ. One aspect of this behaviour that is currently unknown is the distance of influence of such local phenomena as variations in volume fraction and localized fibre bridging.

## 5.2 Assessment of Fibre Bridging

Since it was apparent from the test results that fibre bridging was present in the specimens, it was decided to attempt to determine the extent of the bridging and its affect on the fracture resistance (R-curve) of the specimen. Tests were conducted on a NASA and a DREP specimen to develop an R-curve for each. Figures 5.29 and 5.30 are the resulting plots of critical strain energy release rate as a function of delamination length for the NASA and DREP specimens respectively. From Figure 5.29 for the NASA specimen we see that the initial value of  $G_{IC}$  is  $153 \text{ J/m}^2$ , and that it rapidly increases to  $175 \text{ J/m}^2$  after 10mm of delamination growth.  $G_{IC}$  then continues to increase at a slower rate to a value of  $195 \text{ J/m}^2$  after a total delamination growth of 30mm at the end of the test. The trend at this point is still increasing. In Figure 5.30, the initial value of  $G_{IC}$  for the DREP specimen is  $97 \text{ J/m}^2$ , with a rapid increase to  $120 \text{ J/m}^2$  over the first 4mm of growth. From this point  $G_{IC}$  continues to increase to  $135 \text{ J/m}^2$  over the next 18mm of growth. Beyond 22mm of growth, the value of  $G_{IC}$  is essentially stable for a further 15mm of delamination growth. This indicates that the number of fibre bridges being created is roughly balanced by those being broken. Thus, the NASA specimen exhibits a total increase in  $G_{IC}$  of 27.5%, 14% of it occurring during the initial 33% of the delamination growth. On the other hand, the DREP specimen shows a much larger overall increase of 39%, and it is much more rapid, taking place in the first 18% of growth. This indicates a much more rapid formation of fibre bridging in the DREP specimen. This is shown in Figure 5.31 where the two curves have been superposed.

From the above results it is evident that the amount of crack growth that has already occurred will influence the amount of fibre bridging that has formed and hence the value of the critical strain energy release rate. With this in mind an attempt was made to see if this increased fracture toughness was also manifest in the magnitudes of the COD profiles. Thus a number of graphs were plotted

where a similar  $G_I$  was applied to cracks of different lengths. In order to try and minimize influences other than crack growth, the first criteria for selection was for data from the same specimens. It was also decided to include some cases where data from specimens from the same manufacturer was compared. This data is contained in Figures 5.32 - 5.38. Unfortunately, owing to the lack of control of the manual method used for growing the cracks, there was no data available for very small amounts of crack growth. The smallest amount of growth recorded was 7.23mm on a DREP specimen, but recalling the rapidity with which  $G_{IC}$  increases it is probable that the amount of fibre bridging has almost reached steady state even at this point. It is therefore not surprising that in most of the cases presented there is no apparent influence of crack growth length on the magnitude of the displacement field. This is the case for Figures 5.32 - 5.35. Figure 5.36 and 5.37 illustrate cases where the expected trend is found. It turns out that they represent larger differences in crack lengths than the other cases. It is interesting to note that the data in Figure 5.38 represents a reverse trend, in that the shorter crack has a smaller displacement field. The reason for this may be the fact that they come from two different specimens and it has already been shown that specimen variability can be large.

In examining the methods by which fibre bridging increases the amount of energy required to grow the crack, it becomes apparent that there are two mechanisms involved. The first may be referred to as crack tip shielding, where the presence of fibre bridges reduces the displacements at the crack tip. The second mechanism is one in which the fibre bridges actually provide energy absorption and reduce the amount of energy available to drive the crack. These mechanisms are represented in Figure 5.39. At lower values of  $G_{I\text{applied}}$  the fibre bridges are relatively loose and don't have much of an effect. As the load is increased, the fibres become taut and begin to take up some the load, thus shielding the tip. As the load is further increased, the fibres begin to be ripped out of the matrix and some of the energy is being consumed in this process.

### 5.2.1 Insert Behaviour

As it became apparent that the magnitude of the displacement field was influenced by the amount of fibre bridging present, and that the amount of fibre bridging was related to the amount that the crack had been grown, it was decided to conduct tests on specimens where no crack growth had occurred. Thus, NASA specimen 6 and DREP specimen 9 were subjected to a series of loads, first increasing and then decreasing, to get their COD vs  $r$  profiles at various  $G_I$ . Figures 5.40 and 5.41 contain the profiles for the increasing and decreasing loads on specimen 6, while Figures 5.42 and 5.43 are the data for specimen 9. An examination of the results very quickly revealed that the inserts were exhibiting behaviour that was quite different than that of a true crack. While the profiles from specimen 6 are relatively well behaved, they do not show the profile which is representative of a square root stress singularity. A closer examination of three of the loads, one each on the up and down loadings and the maximum load, are presented in Figures 5.44 - 5.46. It can be seen that the data points are better fit by a linear relationship with  $r$  than with  $r^{1/2}$ . The data from specimen 9 is even further from what would be expected for a crack.

An explanation for this behaviour may be sought by examining photos of the ends of the two inserts. Figure 5.47 is the end of the insert on specimen 6, and Figure 5.48 is from specimen 9. While it is difficult to discern, the insert tip in specimen 6 can be seen to end in a blunt crack, which has a small resin pocket directly in front of it. The end of the insert is more easily seen in specimen 9 as the insert material has been slightly pulled out during the course of the testing. This specimen exhibits a rather large resin pocket ahead of the insert, as shown by the white area, which is due to the charging of the resin in the SEM. This resin pocket ahead of the inserts can act like an elastic foundation, which allows the arms of the specimens to pull apart without forming a typical stress

singularity ahead of the insert. The larger the resin pocket, the more the behaviour differs from that of a typical crack. Thus the behaviour of specimen 9 is considerably different than that of a true crack, or even that of specimen 6.

### 5.3 Mixed-Mode Tests

As another objective of this study, it was desired to use the SEM technique to observe any changes in the displacement fields which occurred under conditions of mixed-mode loading. As was stated previously, LEFM does not consider any interaction to occur when the values of  $G_I$  and  $G_{II}$  are calculated. However, various studies have been done which do report some form of interaction. During this study and the work done in [49] there were ten cases of mixed-mode loads that were examined. The work done in [49] only considered the effect on the CSDs as small opening loads were added to an existing bending load. In all but one of these ten cases, the CSDs were found to increase under mixed-mode loadings. In the other test, the displacements remained approximately the same.

Figures 5.49 - 5.51 show three sets of data which exhibit this increase. In all three cases the increases in the value of  $G_{I \text{ local}}$  determined from the fit lines are significant. One explanation for these increases may be sought from geometric considerations. It can be seen that the addition of a wedge load to an existing bending load will result in an additional bend being applied to the upper arm. Thus the crack would act as if it were in fact seeing a Mode II load which is larger by 1/2 of the wedge opening load applied. However, when calculations are done to determine the new value of  $G_{II}$  based on this larger deflection, the increase is smaller than measured. For example, in Figure 5.51 the fit value of  $G_{II}$  is doubled in the mixed-mode case but the increase that could be attributed to the geometric factor is only 30%. In Figure 5.49, the measured increase is 60% while the

calculated increase would only be 40%. And in Figure 5.50, the measured increase is 80 - 165% but the calculated increase would only be 25%. Clearly there is something else involved. The other factor which should be considered is friction. If there are frictional forces present between the crack faces it is possible that the addition of even a small opening load would be sufficient to unlock all or some of these forces, allowing the displacements to increase.

The COD data was not nearly so consistent. Of the eight tests where CODs were measured, four cases had an increase in CODs, in three they remained the same and in the final test the CODs actually decreased. Figures 5.52 - 5.54 illustrate one of each of these results. One possible explanation for the increases noted under mixed-mode loading would be the presence of interference points on the crack faces. In these cases the application of a bending load to the specimen causes the crack faces to slide across each other and the action of one point riding over another will result in a local opening mode. In the lone case of decreasing displacements it is possible that there was a local region of fibre bridging which, when subjected to Mode II loading, underwent strain and resulted in the crack locally being pulled closed.

#### **5.4 Other Phenomena Noted**

During the course of testing there were two other phenomena that were encountered. The first occurred during a Mode I test where a series of increasing loads was followed by decreasing loads. Figures 5.55 and 5.56 show the displacement profiles for the up and down loads. It appears that, as the loads are increased in Figure 5.55, the location of the crack tip is shifting to the left. This could be indicative of sub-critical crack growth since the applied loads are well below the critical strain energy of the material. But what we then note on the down loads is that the apparent crack tip then moves back to the right again. This is equivalent to crack-closure in metals which have

been plastically strained. Figure 5.57 is a schematic representation of what seems to be happening at the crack tip as the loads are increased. The restoring forces could be supplied by a local region of very strong fibre bridging. The fact that the apparent tip does not return to its original position could indicate that the bridges had been partially pulled out at the higher loads, thus reducing the restoring force.

The other somewhat unusual behaviour that was noted took place during a Mode II test where a similar series of increasing and decreasing loads was applied to the specimen. Figure 5.58 shows the displacement profiles found during the up load portion. Once again it can be seen that the crack tip is moving to the right as the load increases. The distance moved is much greater than that found in the Mode I test, with an apparent 600 microns of growth. Following the application of the highest load and the taking of the SEM photos, the load was left on for approximately 48 hours before the unloading portion of the test was conducted. What was found when the second part of the test was done was that the crack tip had moved an additional 180 microns under the static load. The crack tip then remained stationary during the unloading portion of the test. This unloading data was previously presented as Figures 5.20 - 5.23. There are two possible explanations for this behaviour. The first is that there was actually some sub-critical crack growth. The second is that there was interfacial friction which was gradually overcome as the Mode II load was increased. The case for sub-critical growth is perhaps more strongly supported by the observation of overnight crack growth, as this took place under a static load which was only about  $2/3$  of  $G_{IIC}$  for the material.



## 6 CONCLUSIONS

The following conclusions may be drawn from the work presented here:

- a) The SEM technique which was used was effective in allowing direct observation and measurement of the displacement fields at the crack tip;
- b) The shapes of the displacements, as a function of distance behind the crack tip, were satisfactorily described by an  $r^{1/2}$  profile. This implies that the corresponding stress singularity is of order  $r^{-1/2}$ , as predicted by Linear Elastic Fracture Mechanics;
- c) The orthotropic LEFM equations used for predicting displacements were not able to provide accurate estimates of the magnitudes based on the applied deflections. This was due to a number of physical phenomena encountered during the testing, including:
  - i) the formation of fibre bridging in Mode I tests which resulted in smaller local opening displacements than predicted;
  - ii) variability of the specimens, both on a macro scale as seen in the differences in thicknesses found in the samples from the two sources, and on a micro scale where the volume fraction of fibres varied by as much as 40% through the thickness. It was shown that this local variation can dramatically affect the local moduli, and thus it would also be expected to influence the displacements; and

- iii) difficulties in producing a linear crack front when growth was done by a Mode I load. The presence of curvature will also influence the effective modulus and crack length, thus influencing the predicted displacements.

d) Mixed-mode testing indicates that there is interaction occurring when the two modes are present. In the case of the addition of a Mode I load to an existing Mode II, the magnitudes of the shear displacements were increased in all but one out of ten cases. This effect can be explained in terms of decreasing friction between the crack faces as a Mode I load is applied. The addition of Mode II loads to existing Mode I loads however was found to increase, decrease or have no effect on the magnitudes of the opening displacements. This would indicate that the form of the interaction is influenced by some physical characteristics of the individual crack tips which could not be isolated in this study;

e) Tests conducted at the insert, with no crack growth, showed that the displacement fields that resulted from Mode I loadings were not similar to those found at a sharp crack. Thus, an insert does not behave like a crack. In both cases the presence of a resin pocket ahead of the insert tip caused the half-beams to behave as if they were on a highly compliant foundation;

f) One set of Mode I data displayed behaviour similar to that found in crack closure in metals. These results could be caused by a local region of very strong fibre bridging which effectively locks the crack tip closed until the applied loads reach a sufficient level; and

g) One case of sub-critical crack growth was found in a Mode II test. At loads much lower than critical the location of the crack tip was found to advance. In this test the crack also grew under conditions of static loading over a period of about 48 hours.

## 7 RECOMMENDATIONS

The following recommendations are made for future work in this area:

- a) A study should be conducted utilizing narrower specimens. The use of narrower specimens should result in a straighter crack front across the specimen width, thus giving a more accurate measure of the crack length. It would also minimize any anticlastic effects which may have manifest in the wider specimens.
- b) An investigation into the presence of anticlastic bending under Mode I loading could be done. This could be accomplished using a photoelastic technique or possibly a Moire fringe method.
- c) Tests should be conducted with loads proceeding to the point of fracture. This would allow the assessment of variations of local and global strain energies as a function of applied load.
- d) A more controllable method of crack growth must be used so that cracks may be grown in 1mm or less increments. This will allow for the observation of the development of fibre bridging and its affect on the local vs. global strain energies.
- e) A more extensive study of mixed mode loadings should be conducted. This should include different variations in the ratio of the Mode I to Mode II component to establish an differences in the interactions.

## REFERENCES

- [1] Broek, D., *Elementary Engineering Fracture Mechanics*, 4<sup>th</sup> revised edition, Martinus Nijhoff Publishers, 1986
- [2] Rybicki, E.F., Hernandez, T.D., Deibler, J.E., Knight, R.C. and Vinson, S.S., "Mode I and Mixed Mode Energy Release Rate Values for Delamination of Graphite/Epoxy Test Specimens", *Journal of Composite Materials*, Vol.21, 1987, pp.105-123
- [3] Tada, H, Paris, P.C. and Irwin, G.R., *The Stress Analysis of Cracks Handbook*, Paris Productions Inc. and Del Research Corporation, 226 Woodbourne Dr., St.Louis, Missouri, 63105, 1985
- [4] Russell, A.J. and Street, K.N., "The Effect of Matrix Toughness on Delamination: Static and Fatigue Fracture Under Mode II Shear Loading of Graphite Fibre Composites", ASTM STP 937, N.J. Johnson, Ed., American Society for Testing and Materials, 1987, pp.275-294
- [5] Williams, J.G., "The Fracture Mechanics of Delamination Tests", *Journal of Strain Analysis*, Vol.24, No.4, 1989, pp.207-214
- [6] Kanninen, M.F., "An Augmented Double Cantilever Beam Model for Studying Crack Propagation and Arrest", *International Journal of Fracture*, Vol.9, No.1, 1973, pp.83-91
- [7] Sih, G.C., Paris, P.C. and Irwin, G.R., "On Cracks in Rectilinearly Anisotropic Bodies", *International Journal of Fracture Mechanics*, Vol. 1, 1965, pp.189-202
- [8] Russell, A.J., "Factors Affecting the Opening Mode Delamination of Graphite/Epoxy Laminates", Defence Research Establishment Pacific Materials Report 82-Q, Dec. 1982
- [9] Russell, A.J. and Street, K.N., "Moisture and Temperature Effects on the Mixed-Mode Delamination Fracture of Unidirectional Graphite/Epoxy", ASTM STP 876, W.S. Johnson, Ed., American Society for Testing and Materials, 1985, pp.349-370
- [10] Shah, R.C., Miliziano, G. and Viswanathan, A.V., "Interlaminar Fracture Characteristics of Tougher Thermoset Materials", *Journal of Aircraft*, Vol.23, No.7, 1986, pp.599-605
- [11] Bradley, W.L., "Relationship of Matrix Toughness to Interlaminar Fracture Toughness", *Application of Fracture Mechanics to Composite Materials*, Chap. 5, K. Freidrich, Ed., Elsevier Applied Science, 1989
- [12] Hunston, D.L., Moulton, R.L., Johnston, W.J. and Bascom, W.D., "Matrix Resin Effects in Composite Delamination: Mode I Fracture Aspects", ASTM STP 937, N.J. Johnston, Ed., American Society for Testing and Materials, 1987, pp.74-94
- [13] Bradley, W.L. and Cohen, R.N., "Matrix Deformation and Fracture in Graphite Reinforced Epoxies", ASTM STP 876, W.S. Johnson, Ed., American Society for Testing and Materials, 1985, pp.389-410
- [14] Lee, S.M., "Failure Mechanism of Delamination Fracture", ASTM STP 972, J.D. Whitcomb, Ed., American Society for Testing and Materials, 1988, pp.356-365
- [15] Davies, P., Moulin, C., Kausch, H.H. and Fischer, M., "Measurement of  $G_{IC}$  and  $G_{IIC}$  in Carbon/Epoxy Composites", *Composites Science and Technology*, 39, 1990, pp.193-205
- [16] Martin, R.H. and Murri, G.B., "Characterization of Mode I and Mode II Delamination Growth and Thresholds in Graphite/PEEK Composites", NASA Technical Memorandum 100577, April 1988

- [17] Russell, A.J. and Street, K.N., " Factors Affecting the Interlaminar Fracture Energy of Graphite/Epoxy Laminates", *Progress in Science and Engineering of Composites*, T. Hayashi, K. Kawata and S. Umekawa, Eds., ICCM-IV, 1982, pp279-286
- [18] Prel, Y.J., Davies, P., Benzeggagh, M.L. and DeCharentenay, F.X., "Mode I and Mode II Delamination of Thermosetting and Thermoplastic Composites", ASTM STP 1012, P.A. Lagace, Ed., American Society for Testing and Materials, 1987
- [19] Russell, A.J. and Street, K.N., "A Constant  $\Delta G$  Test for Measuring Mode I Interlaminar Fatigue Crack Growth Rates", ASTM STP 972, J.D. Whitcomb, Ed., American Society for Testing and Materials, 1988, pp.
- [20] Russell, A.J., "Micromechanisms of Interlaminar Fracture and Fatigue", NRCC/IMRI, 1986
- [21] Kageyama, K., Kobayashi, T. and Chou, T.-W., "Analytical Compliance Method for Mode I Interlaminar Fracture Toughness Testing of Composites", *Composites*, Vol. 18, No. 5, 1987
- [22] Bascom, W.D., Boll, D.J., Hunston, D.L., Fuller, B. and Phillips, P.J., "Fractographic Analysis of Interlaminar Fracture", ASTM STP 937, N.J. Johnston, Ed., American Society for Testing and Materials, 1987, pp.131-149
- [23] Johnson, W.S. and Mangalgiri, P.D., "Influence of the Resin on Interlaminar Mixed-Mode Fracture", ASTM STP 937, N.J. Johnston, Ed., American Society for Testing and Materials, 1987, pp.295-315
- [24] Phillips, D.C. and Wells, G.M., "The Stability of Transverse Cracks in Fibre Composites", *Journal of Materials Science Letters*, 1, 1982, pp.321-324
- [25] DeCharentenay, F.X., Harry, J.M., Prel, Y.J. and Benzeggagh, M.L., "Characterizing the Effect of Delamination Defect by Mode I Delamination Test", ASTM STP 836, 1984, 1984, pp.84-103
- [26] DeCharentenay, F.X. and Benzeggagh, M.L., "Fracture Mechanics of Mode I Delamination in Composite Materials,
- [27] Johnson, W.S. and Mangalgiri, P.D., "Investigation of Fiber Bridging in Double Cantilever Beam Specimens", NASA Technical Memorandum 87716, April 1986
- [28] Newaz, G.M. and Ahmad, J., "A Simple Technique for Measuring Mode I Delamination Energy Release Rate in Polymeric Composites", *Engineering Fracture Mechanics*, Vol.33, No.4, 1989, pp.541-552
- [29] Glessner, Takemori, Vallance and Gifford, " Mode I Interlaminar Fracture Toughness of Unidirectional Carbon Fiber Composites Using a Novel Wedge-Driven Delamination Design", ASTM STP 1012, P.A. Lagace, Ed., American Society for Testing and Materials, 1989, pp.181-200
- [30] O'Brien, T.K., Murri, G.B. and Salpekar, S.A., "Interlaminar Shear Fracture Toughness and Fatigue Thresholds for Composite Materials", ASTM STP 1012, P.A. Lagace, Ed., American Society for Testing and Materials, 1989, pp.222-250
- [31] Giare, G.S., "Fracture Toughness of Unidirectional Fibre Reinforced Composites in Mode II", *Engineering Fracture Mechanics*, Vol.20, No.1, 1984, pp.11-21
- [32] Gillespie, J.W., Carlsson, L.A. and Pipes, R.B., "Finite Element Analysis of the End Notch Flexure Specimen for Measuring Mode II Fracture Toughness", *Composites Science and Technology*, 27, 1986, pp.177-197

- [33] Hashemi, S., Kinloch, A.J. and Williams, J.G., "The Analysis of Interlaminar Fracture in Uniaxial Fiber-Polymer Composites", Proceedings of the Royal Society of London, A427, 1990, pp.173-199
- [34] Ramkumar, R.L. and Whitcomb, J.D., "Characterization of Mode I and Mixed Mode Delamination Growth in T300/5208 Graphite/Epoxy", ASTM STP 876, W.S. Johnson, Ed., American Society for Testing and Materials, 1985, pp.315-335
- [35] Jurf, R.A. and Pipes, R.B., "Interlaminar Fracture of Composite Materials", Journal of Composite Materials, 16, 1982, pp.386-394
- [36] Wu, E.M., "Application of Fracture Mechanics to Anisotropic Plates", Journal of Applied Mechanics, 34, 1967, pp.967-974
- [37] Benzeggagh, M.L., Davies, P., Gong, X.J., Roelandt, M., Mourin, M. and Prel, Y.J., "A Mixed Mode Specimen for Interlaminar Fracture Testing", Composites Science and Technology, 34, 1989, pp.129-143
- [38] Valisetty, R.R. and Chamis, C.C., "Sublaminar- or Ply-Level Analysis of Composites and Strain Energy Release Rates of End-Notch and Mixed-Mode Fracture Specimens", ASTM STP 972, J.D. Whitcomb, Ed., American Society for Testing and Materials, 1988, pp.41-56
- [39] Theocaris, P.S., Stassinakis, C.A. and Kytopoulos, V., "Stress Intensity Factors and COD's Defined by In-Plane Displacements Measured by Scanning Electron Microscopy", Journal of Materials Science, Vol.23, 1988, pp.3992-3996
- [40] Theocaris, P.S., "The Elastic Field Around the Crack Tip Measured by Scanning Electromicroscopy", Engineering Fracture Mechanics, Vol.37, No.4, 1990, pp.739-751
- [41] Kortschot, M.T., "High Resolution Strain Measurements by Direct Observation in the Scanning Electron Microscope", Journal of Materials Science Letters, 7, pp.3970-3972
- [42] Kikukawa, M., Jono, M. and Adachi, M., "Direct Observation and Mechanism of Fatigue Crack Propagation", ASTM STP 675, 1979, pp.234-253
- [43] Mao, T.H., Beaumont, P.W.R. and Nixon, W.C., "Direct Observations of Crack Propagation in Brittle Materials", Journal of Materials Science Letters, 2, 1983, pp.613-616
- [44] Smith, P.A., Gilbert, D.G. and Poursartip, A., "Matrix Cracking of Composites Inside a Scanning Electron Microscope", Journal of Materials Science Letters, 4, 1985, pp.845-847
- [45] Ferguson, J.S., Gambone, L.R. and Poursartip, A., "The Influence of Mode of Loading on the Local Crack Tip Behaviour of Delaminations", presented at CANCOM 91, 4-8 Sep. 1991, Montreal, Canada
- [46] Carlsson, L.A. and Gillespie, J.W., "Mode-II Interlaminar Fracture of Composites", *Application of Fracture Mechanics to Composite Materials*, Chap. 4, K. Freidrich, Ed., Elsevier Science Publishers, 1989, pp.113-157
- [47] Corleto, C., Bradley, W.L. and Henriksen, M., "Correspondence Between Stress Fields and Damage Zones Ahead of the Crack Tip of Composites Under Mode I and Mode II Delamination", ICCM & ECCM, Proceedings of 6<sup>th</sup> International Conference on Composite Materials, 1987, Elsevier Applied Science Publishers, pp.3.378-3.387
- [48] Crews, J.H. and Reeder, J.R., "A Mixed Mode Bending Apparatus for Delamination Testing", NASA Technical Memorandum 100662, Aug. 1988
- [49] Poursartip, A.P. and Gambone, L.R., unpublished data, Department of Metals and Materials Engineering, University of British Columbia, Vancouver, Canada

- [50] Poursartip, A., Riahi, G. and Smith, G., "Resin Flow During Autoclave Processing of Composite Laminates", Presented at ICCM8, Honolulu, 1991
- [51] Tsai, S.W., *Composites Design*, 4th Edition, Chap. 10, Think Composites Publishers, 1988

## APPENDIX 1

### Orthotropic Derivation of Sih, Paris and Irwin

The authors derived the characteristic equations for a crack in a rectilinearly anisotropic body in the following manner:

The deformations are given by the generalized Hooke's Law as:

$$\varepsilon_i = \sum_{j=1}^6 a_{ij} \sigma_j, a_{ij} = a_{ji} (i = 1, 2 \dots 6) \quad (A1.1)$$

In plane problems such as these, symmetry reduces the number of independent elastic constants to 6, namely  $a_{ij} (i, j = 1, 2, 6)$ . When the case is one of two-dimensional anisotropy, the problem can be formulated as an analytic function  $\phi_j(z_j)$ , where  $z_j$  is the complex variable:

$$z_j = x_j + iy_j, (j = 1, 2) \quad (A1.2)$$

And the components are given by:

$$x_j = x + \alpha_j y \quad (A1.3)$$

$$y_j = \beta_j y \quad (A1.4)$$



$\alpha_j$  and  $\beta_j$  are the real and imaginary parts of  $\mu_j = \alpha_j + \beta_j$ , and  $\mu_j$  are the roots of the characteristic equation:

$$a_{11}\mu^4 - 2a_{16}\mu^3 + (2a_{12} + a_{66})\mu^2 - 2a_{26}\mu + a_{22} = 0 \quad (A1.5)$$

In the case of a specially orthotropic material, such as the unidirectional composite being tested, the elastic constants  $a_{16}$  and  $a_{26}$  are zero. This reduces the characteristic equation to the form:

$$a_{11}\mu^4 + (2a_{12} + a_{66})\mu^2 + a_{22} = 0 \quad (A1.6)$$

where  $a_{11}=1/E_1$ ,  $a_{22}=1/E_2$ ,  $a_{12}=-\nu_{12}/E_1$  and  $a_{66}=1/G_{12}$  for plane stress. There is a corresponding set of elastic constants for the plane strain case which are given by:

$$b_{ij} = a_{ij} - \frac{a_{i3}a_{j3}}{a_{33}}; (i, j = 1, 2, 6) \quad (A1.7)$$

Equation (A1.6) will have two complex and two wholly imaginary roots, which can be determined using the standard quadratic solution:

$$\mu^2 = \frac{-b \pm \sqrt{b^2 - 4ac}}{2a} \quad (A1.7)$$

where  $a=a_{11}$ ,  $b=(2a_{12}+a_{66})$  and  $c=a_{22}$ .

$$\therefore \mu^2 = \frac{-(2a_{12} + a_{66}) \pm \sqrt{(2a_{12} + a_{66}) - 4a_{11}a_{22}}}{2a_{11}} \quad (A1.8)$$

$$\therefore \mu_1^2 = \frac{-(2a_{12} + a_{66}) + \sqrt{(2a_{12} + a_{66}) - 4a_{11}a_{22}}}{2a_{11}} = \frac{-d + e}{2a_{11}} \quad (A1.9)$$

$$\therefore \mu_1^2 = \frac{-(2a_{12} + a_{66}) - \sqrt{(2a_{12} + a_{66}) - 4a_{11}a_{22}}}{2a_{11}} = \frac{-d - e}{2a_{11}} \quad (A1.10)$$

where  $d = 2a_{12} + a_{66}$  and  $e = \sqrt{(2a_{12} + a_{66}) - 4a_{11}a_{22}}$ .

$$\therefore \mu_1 = \pm \sqrt{\frac{-d + e}{2a_{11}}}; \mu_2 = \pm \sqrt{\frac{-d - e}{2a_{11}}} \quad (A1.11)$$

We are interested in the displacement fields generated in Mode I, opening, and Mode II, in-plane shear, loadings, which can be determined from:

Mode I:

$$u = K_I \sqrt{2r} \operatorname{Re} \left[ \frac{1}{\mu_1 - \mu_2} (\mu_1 p_2 \sqrt{\cos \theta + \mu_2 \sin \theta} - \mu_2 p_1 \sqrt{\cos \theta + \mu_1 \sin \theta}) \right] \quad (A1.12)$$

$$v = K_I \sqrt{2r} \operatorname{Re} \left[ \frac{1}{\mu_1 - \mu_2} (\mu_1 q_2 \sqrt{\cos \theta + \mu_2 \sin \theta} - \mu_2 q_1 \sqrt{\cos \theta + \mu_1 \sin \theta}) \right] \quad (A1.13)$$

where:

$$p_1 = a_{11}\mu_1^2 + a_{12}; p_2 = a_{11}\mu_2^2 + a_{12} \quad (A1.14)$$

$$q_1 = a_{12}\mu_1 + \frac{a_{22}}{\mu_1}; q_2 = a_{12}\mu_2 + \frac{a_{22}}{\mu_1} \quad (A1.15)$$

Mode II:

$$u = K_{II}\sqrt{2r} \operatorname{Re} \left[ \frac{1}{\mu_1 - \mu_2} (p_2\sqrt{\cos\theta + \mu_2\sin\theta} - p_1\sqrt{\cos\theta + \mu_1\sin\theta}) \right] \quad (A1.16)$$

$$v = K_{II}\sqrt{2r} \operatorname{Re} \left[ \frac{1}{\mu_1 - \mu_2} (q_2\sqrt{\cos\theta + \mu_1\sin\theta} - q_1\sqrt{\cos\theta + \mu_1\sin\theta}) \right] \quad (A1.17)$$

Our area of interest is on the crack face behind the crack tip, at  $\theta = 180^\circ$ . Thus  $\sin\theta=1$ , and  $\cos\theta=-1$ . In Mode I,  $u = 0$  at  $\theta = 180^\circ$ , so solving for  $v$ :

$$v = K_I\sqrt{2r} \operatorname{Re} \left[ \frac{1}{\mu_1 - \mu_2} (\mu_1 q_2 i - \mu_2 q_1 i) \right] \quad (A1.18)$$

Substituting for  $q_1$  and  $q_2$  and simplifying:

$$v = K_I\sqrt{2r} \operatorname{Re} \left[ \frac{\mu_1 + \mu_2}{\mu_1\mu_2} a_{22} i \right] \quad (A1.19)$$

Recalling the expressions for  $\mu_1$  and  $\mu_2$ , it is apparent that the solutions for  $\mu_1 + \mu_2$  and  $\mu_1\mu_2$  must be determined. Initially both positive roots of  $\mu_1$  and  $\mu_2$  will be selected:

$$\mu_1 + \mu_2 = \left( 2\sqrt{\frac{a_{22}}{a_{11}}} - \frac{2a_{12} + a_{66}}{a_{11}} \right)^{\frac{1}{2}} \quad (A1.20)$$

$$\mu_1\mu_2 = \sqrt{\frac{d^2 + e^2}{4a_{11}^2}} \quad (A1.21)$$

where  $d$  and  $e$  are as previously defined. So simplifying:

$$\mu_1\mu_2 = \sqrt{\frac{a_{22}}{a_{11}}} \quad (A1.22)$$

Substituting these into the equation for  $v$  and simplifying yields:

$$v = K_f \sqrt{2r} \sqrt{2} \sqrt{a_{11}a_{22}} Re \left[ \left( \frac{2a_{12} + a_{66}}{2a_{11}} - \sqrt{\frac{a_{22}}{a_{11}}} \right)^{\frac{1}{2}} \right] \quad (A1.23)$$

This term will not always give real solutions, therefore we select the negative root of either  $\mu_1$  or  $\mu_2$ :

$$\mu_1 + \mu_2 = \left( -2\sqrt{\frac{a_{22}}{a_{11}}} - \frac{2a_{12} + a_{66}}{a_{11}} \right)^{\frac{1}{2}} \quad (A1.24)$$

$$\mu_1\mu_2 = -\sqrt{\frac{a_{22}}{a_{11}}} \quad (A1.25)$$

$$v = K_I \sqrt{4ra_{11}a_{22}} \left[ \frac{2a_{12} + a_{66}}{2a_{11}} + \sqrt{\frac{a_{22}}{a_{11}}} \right]^{\frac{1}{2}} \quad (A1.26)$$

In Mode II,  $v = 0$  at  $\theta = 180^\circ$ , so solving for  $u$ :

$$u = K_{II} \sqrt{2r} \operatorname{Re} \left[ \frac{1}{\mu_1 - \mu_2} (p_2 i - p_1 i) \right] \quad (A1.27)$$

Substituting and simplifying:

$$u = K_{II} \sqrt{2r} a_{11} \operatorname{Re} [-(\mu_1 + \mu_2) i] \quad (A1.28)$$

Substituting the previously derived expression for  $\mu_1 + \mu_2$ , we have:

$$u = K_{II} \sqrt{2r} a_{11} \left[ 2 \sqrt{\frac{a_{22}}{a_{11}}} + \frac{2a_{12} + a_{66}}{a_{11}} \right]^{\frac{1}{2}} \quad (A1.29)$$

which is always real. These equations can be shown to reduce to the isotropic solutions when the appropriate constants are inserted. Sih, Paris and Irwin provide relationships between the strain energy release rate and the stress intensity factor as follows:

$$G_I = \pi K_I^2 \sqrt{\frac{a_{11}a_{22}}{2}} \left[ \sqrt{\frac{a_{22}}{a_{11}}} + \frac{2a_{12} + a_{66}}{2a_{11}} \right]^{\frac{1}{2}} \quad (A1.30)$$

$$G_{II} = \pi K_{II}^2 \frac{a_{11}}{\sqrt{2}} \left[ \sqrt{\frac{a_{22}}{a_{11}}} + \frac{2a_{12} + a_{66}}{2a_{11}} \right]^{\frac{1}{2}} \quad (A1.31)$$

Then solving these equations for  $K_I$  and  $K_{II}$  and substituting them into equations (A1.27) and (A1.30), we can relate the predicted COD and CSD field as a function of the applied  $G$ :

$$COD = 2v = \frac{4}{\sqrt{\pi}} \cdot 2^{\frac{1}{4}} \cdot \left[ \frac{2a_{12} + a_{66}}{2a_{11}} + \sqrt{\frac{a_{22}}{a_{11}}} \right]^{\frac{1}{4}} (a_{11}a_{22})^{\frac{1}{4}} \sqrt{r} \sqrt{G_I} \quad (A1.32)$$

$$CSD = 2u = 4 \frac{\sqrt{a_{11}}}{\sqrt{\pi}} \cdot 2^{\frac{1}{4}} \cdot \left[ \frac{2a_{12} + a_{66}}{2a_{11}} + \sqrt{\frac{a_{22}}{a_{11}}} \right]^{\frac{1}{4}} \sqrt{r} \sqrt{G_{II}} \quad (A1.33)$$

## APPENDIX 2

### $G_{II}$ Corrections for Base Deflection

During early testing in Mode II and mixed mode conditions it was noticed that the aluminum base of the test fixture was deflecting. Since the amount of bend being applied to the specimen was determined in relation to the base, this resulted in an over-estimation of the value of  $G_{II}$ . The base was subsequently reinforced with a steel backing plate but it was necessary to determine the effective stiffness of the base so that an accurate value of  $G_{II}$  could be calculated.

In order to be able to determine the stiffness of the base, it was necessary to estimate the effective moment of inertia for the reinforced beam. Figure A2.1 shows the actual dimensions of the base and the equivalent section based on a modulus for steel of 210 GPa and for aluminum of 70 GPa. The analysis for the true deflection of the specimen is as follows:

$$\bar{y} = \frac{\int y da}{A} \quad (A2.1)$$

where  $\bar{y}$  is the distance from the bottom of the base to the centroid of the area,  $y da$  are the first moments of inertia of each element of area, and  $A$  is the total area.

$$\bar{y} = \frac{(45 \cdot 6.5 \cdot 8.05) + (120 \cdot 4.8 \cdot 2.4)}{(45 \cdot 6.5) + (120 \cdot 4.8)} \quad (A2.2)$$

$$\bar{y} = 4.30mm \quad (A2.3)$$

Application of the transfer formula then allows us to calculate the moment of inertia of the total section about the centroid,  $I_x$ :

$$I_{\bar{y}} = \Sigma(I_x + Ad_y^2) = \Sigma\left(\frac{1}{12}bh^3 + A\bar{y}^2\right) \quad (A2.4)$$

$$I_{\bar{y}} = \frac{1}{12} \cdot 120 \cdot 4.8^3 + 120 \cdot 4.8 \cdot 1.6^2 + \frac{1}{12} \cdot 45 \cdot 6.5^3 + 45 \cdot 6.5 \cdot 3.75^2 \quad (A2.5)$$

$$I_{\bar{y}} = 7723.6mm^4 = 7.72 \times 10^{-9}m^4 \quad (A2.6)$$

The moment of inertia for the un-reinforced aluminum base is simply:

$$I_{\bar{y}} = \frac{1}{12}bh^3 = \frac{1}{12} \cdot 45 \cdot 6.5^3 = 1029.84mm^4 \quad (A2.7)$$

$$I_{\bar{y}} = 1.03 \times 10^{-9}m^4 \quad (A2.8)$$

The measured deflection will be a combination of specimen and base deflections, but the load applied to each will be the same. Thus the load can be determined from the compliance of each part as follows:

$$\delta = C \cdot P \quad (A2.9)$$

$$\delta_m = \delta_s + \delta_b \quad (A2.10)$$



where  $\delta_m$  is the measured deflection,  $\delta_s$  is the actual deflection of the specimen, and  $\delta_b$  is the deflection of the base.

$$\delta_s = C_s \cdot P \quad (A2.11)$$

$$\delta_b = C_b \cdot P \quad (A2.12)$$

where  $C_s$  and  $C_b$  are given by:

$$C_s = \frac{L^3 + 3a^3}{2Eb h^3} \quad (A2.13)$$

$$C_b = \frac{L^3}{3EI_y} \quad (A2.14)$$

$$\delta_m = C_s \cdot P + C_b \cdot P = P(C_s + C_b) \quad (A2.15)$$

$$P = \frac{\delta_m}{C_s + C_b} \quad (A2.16)$$

$$P = \frac{\delta_m}{\frac{(L^3 + 3a^3)}{2E_s b_s h_s^3} + \frac{L^3}{3E_b I_y}} \quad (A2.17)$$

Once  $P$  is determined, then it can be used to determine the actual deflection of the specimen, and subsequently the value of  $G_{II}$ . As an example, for a specimen with  $a = 44.39\text{mm}$ ,  $L = 99.96\text{mm}$ ,

$h = 1.76\text{mm}$  and  $E_s = 126\text{ GPa}$ , and an applied deflection of  $7.9\text{mm}$ , the load will be  $169.6\text{N}$ , the deflection of the base will be  $0.114\text{mm}$  and the true deflection of the specimen will be  $7.786\text{mm}$ . Thus, instead of the initial calculated value of  $478.0\text{ J/m}^2$  for  $G_{II}$ , the corrected value is  $464.3\text{ J/m}^2$ . If the same calculation is done using the moment of inertia for the un-reinforced base the deflection of the base is  $0.723\text{mm}$  giving a true deflection of the specimen of  $7.177\text{mm}$ , and a corrected  $G_{II}$  of  $394.6\text{ J/m}^2$ .

## APPENDIX 3

### Equations for Determining $A_I$ and $A_{II}$ as a Function of $V_f$

In order to be able to determine the values of  $A_I$  and  $A_{II}$  as a function of the fibre volume fraction, it is necessary to determine how the elastic moduli vary. The book by Tsai [51] provides us with a means of estimating this variation. There are three moduli which must be estimated:  $E_1$ , the longitudinal elastic modulus;  $E_2$ , the transverse modulus; and,  $E_s$ , the longitudinal shear modulus. During the calculation of these properties, there is a need for elastic properties of the fibres which are not possible to measure. In these cases the author has presented a method of back-calculating the necessary numbers from measured laminate data.

### Longitudinal Elastic Modulus

The longitudinal elastic modulus is determined using a simple rule of mixtures formula:

$$E_1 = V_f E_f + V_m E_m \quad (A3.1)$$

where  $V_f$  is the volume fraction of fibres in the composite,  $E_f$  is the longitudinal modulus of the fibres,  $V_m$  is the volume fraction of matrix (equal to  $1 - V_f$ ) and  $E_m$  is the modulus of the isotropic matrix.

In order to be able to use this equation we must know the values for the longitudinal elastic moduli for the fibres and the matrix. The value for an epoxy resin is available in literature and

is reported as 3.45 GPa. To determine the modulus of AS4 fibres, we will back-calculate from the literature value of the longitudinal modulus for a laminate with a fibre volume fraction 0.66, of 138 GPa.

$$E_f = \frac{E_1 - (1 - V_f)}{V_f} \quad (A3.2)$$

When the appropriate values are inserted we get  $E_f = 207.3$  GPa. Thus the formula for determining the longitudinal shear modulus as a function of fibre volume fraction is:

$$E_1 = 207.3V_f + 3.45(1 - V_f) \quad (A3.3)$$

### Longitudinal Shear Modulus

Here, the equation is given as:

$$\frac{(1 + V^*)}{E_s} = \frac{1}{G_{fx}} + \frac{V^*}{G_m} \quad (A3.4)$$

where  $G_{fx}$  is the longitudinal shear modulus of the fibres,  $G_m$  is the shear modulus of the matrix and  $V^*$  is the reduced matrix/fibre volume fraction, found from the equation:

$$V^* = \eta_s \frac{V_m}{V_f} \quad (A3.5)$$

where  $\eta_s$  is a stress partitioning parameter which has been introduced to correct for the fact that the values predicted by using the actual volume fraction are lower than measured experimentally. This indicates that the fibres carry more of the load than predicted by a simple ratio of the volumes. Tsai recommends the use of 0.316 as the value of  $\eta_s$  for graphite/epoxy systems. Once again we must use a back-calculation to determine the value of  $G_{fx}$ . To do this we will use the reported values of  $E_s=7.17$  GPa for the laminate and  $G_m=1.28$  GPa. This gives a value for  $\eta_s$  of 0.163 and for  $G_{fx}$  of 28.7 GPa. The equation for calculating the longitudinal shear modulus as a function of fibre volume fraction is:

$$E_s = \frac{(1 + V^*)}{\left(\frac{1}{28.7}\right) + \left(\frac{V^*}{1.28}\right)} \quad (A3.6)$$

where  $V^*=0.316(1-V_f)/V_f$ .

### Transverse Modulus

The transverse modulus is calculated from the equation:

$$E_2 = \frac{(1 + V_y^*)}{\left(\frac{1}{E_{fy}}\right) + \left(\frac{V_y^*}{E_m}\right)} \quad (A3.7)$$

where  $V_y^*=\eta_y(1-V_f)/V_f$  is the reduced matrix/fibre volume fraction in the transverse direction, and  $E_{fy}$  is the transverse elastic modulus of the fibres. Tsai recommends the use of  $\eta_y=0.516$ .

The value of the fibre transverse elastic modulus will be back-calculated using the transverse laminate modulus of 8.96 GPa. This gives  $E_{fy}=15.58$  GPa. This results in an equation for calculating the transverse modulus of the laminate as a function of fibre volume fraction as:

$$E_2 = \frac{(1 + V_y^*)}{\left(\frac{1}{15.58}\right) + \left(\frac{V_y^*}{3.45}\right)} \quad (A3.8)$$

These three equations were used in determining the compliance coefficients for assessing the effect of local volume fraction changes on the values of  $A_I$  and  $A_{II}$ , and hence the expected magnitudes of the COD and CSD profile.

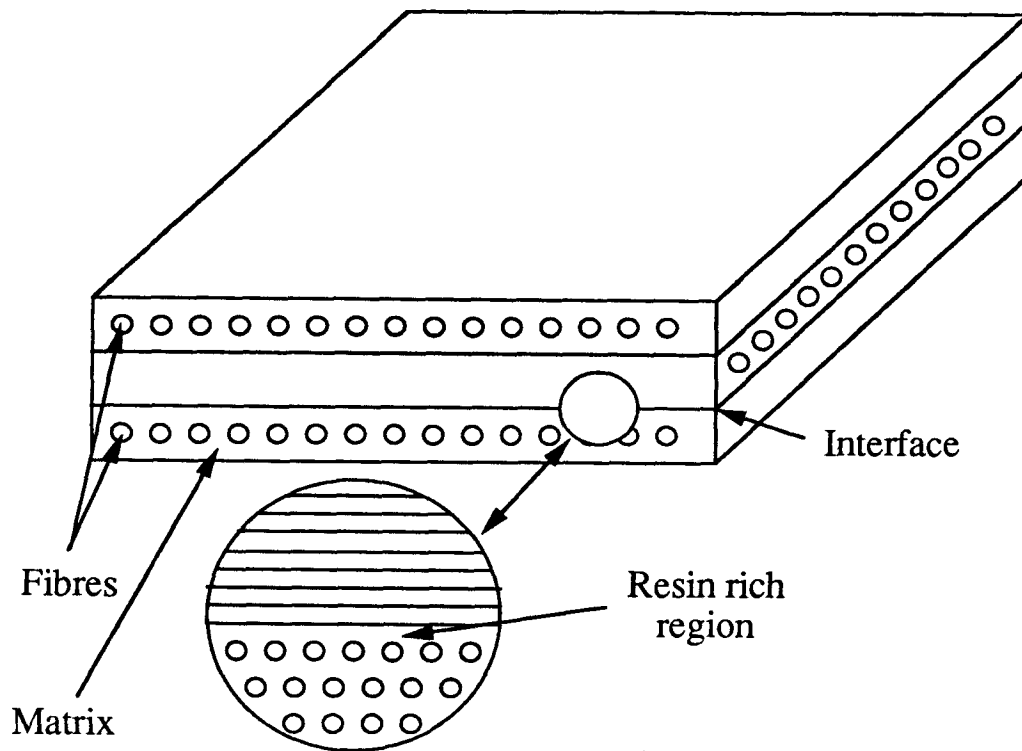


Fig. 1.1 - A typical composite laminate made up of unidirectional plies of fibres in a matrix. Individual layers are oriented to provide desired strength.

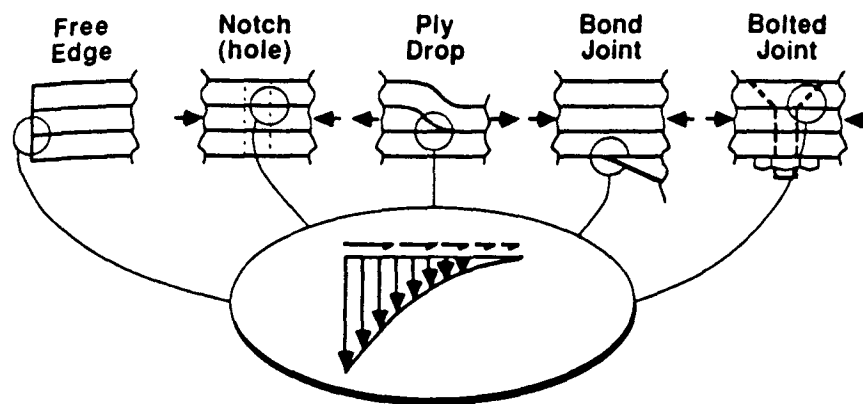


Fig. 1.2 - Examples of cases where in-plane loads can generate out-of-plane components.  
[44]

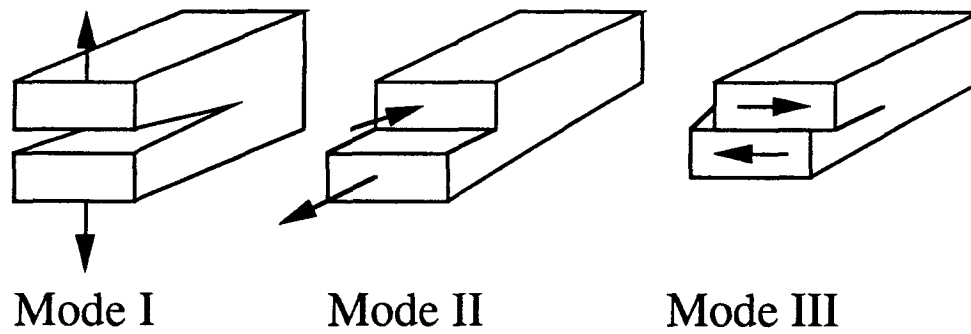


Fig. 2.1 - The three modes of loading that can be imposed on a crack tip. [44]

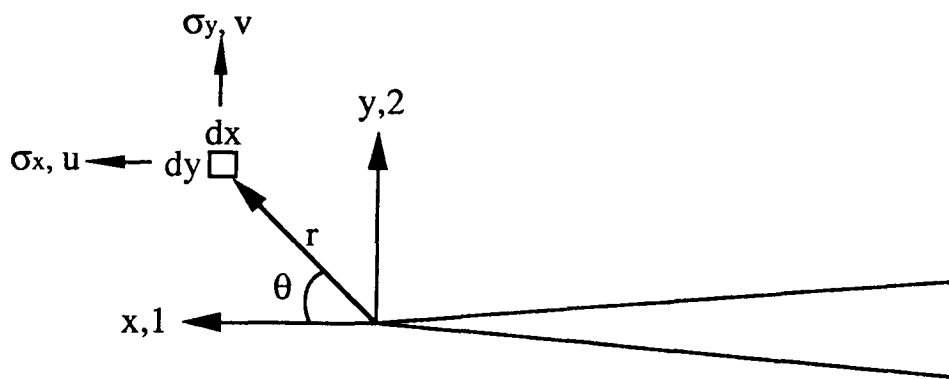


Fig. 2.2 - Crack tip coordinate system identifying directions, and showing a representative element of material near the crack tip.



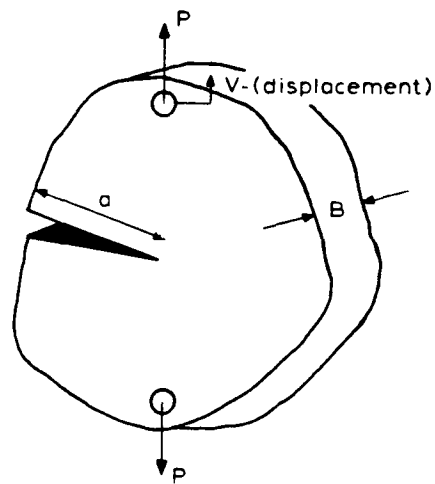


Fig. 2.3 - Schematic of a cracked plate loaded by a force  $P$ . Load points then undergo displacement  $v$ . [1]

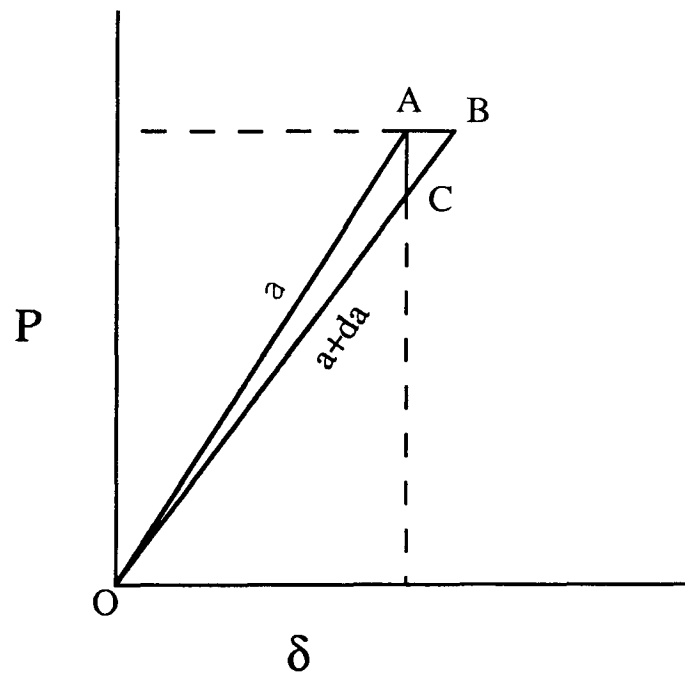


Fig. 2.4 - A load-displacement curve showing what takes place when crack growth occurs under fixed load ( $AB$ ) and fixed displacement ( $AC$ ) conditions.

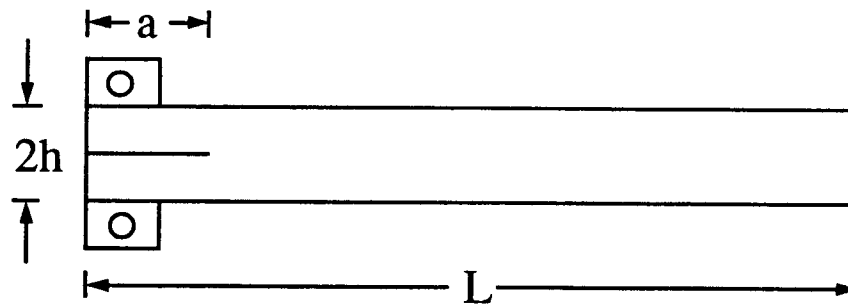


Fig. 2.5 - The typical configuration of the Double Cantilever Beam (DCB) specimen, which is most often used for Mode I testing.

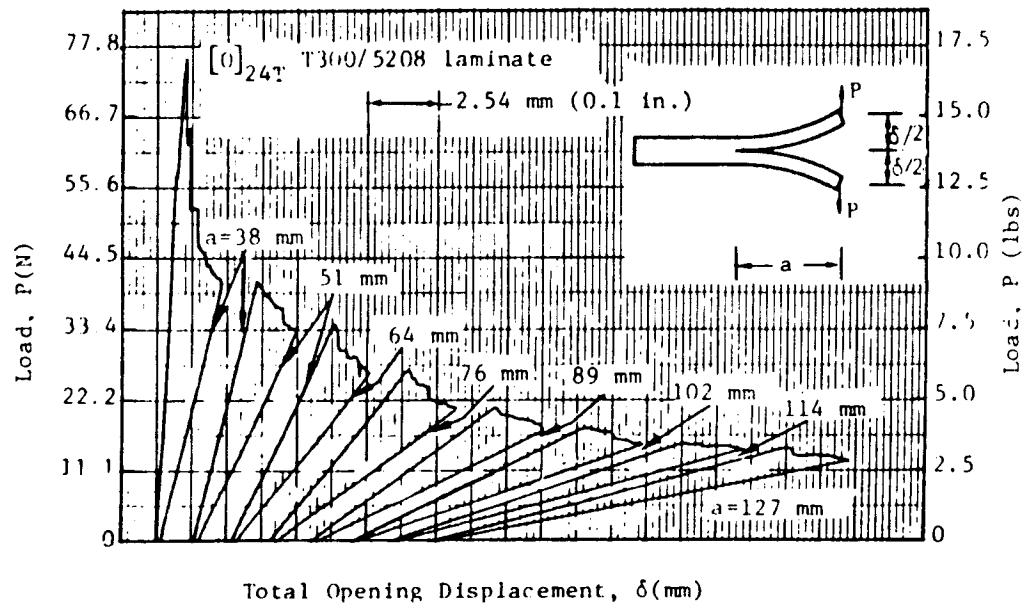


Fig. 2.6 - An example of a load-displacement plot resulting from repeated incremental growth of the crack. This data is used to determine the change in compliance as a function of crack length, and the critical Strain Energy Release Rate ( $G_{IC}$ ). [32]

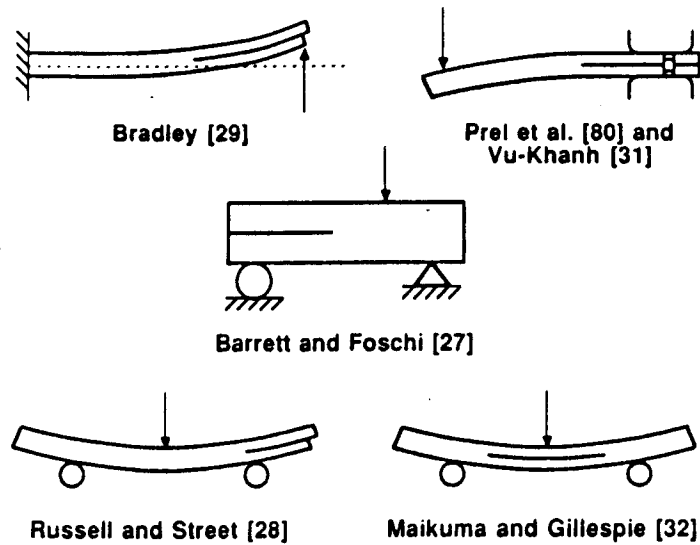
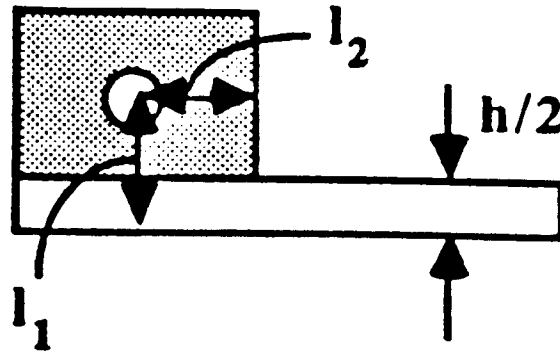


Fig. 2.7 - Several test specimen configurations that have been used for conducting flexural measurement of Mode II interlaminar fracture resistance. [44]



### Mode I DCB

$$\Theta_1 = 0.30 \quad (\text{note } L=a)$$

$$\Theta_2 = 1.50$$

$$\Theta_3 = 1.0$$

$$\Theta_4 = 9/8 (1 - (l_2/a)^2)$$

$$\Theta_5 = 9/35$$

### Mode II ELS

$$\Theta_1 = 0.15 (15 + 50 (a/L)^2 + 63 (a/L)^4) / (1 + 3 (a/L)^3)^2$$

$$\Theta_2 = -3 \cdot [(1 + 3 (a/L)^2) / (1 + 3 (a/L)^3)^3] \cdot (L/a)$$

$$\Theta_3 = 4 / (1 + 3 (a/L)^3)$$

$$\Theta_4 = -9/4 \left\{ (1 - a/L)(1 + 3 (a/L)^3) + 4 (1 - (l_2/a)^2) \cdot (a/L)^2 \cdot (1 + 3 (a/L)^2) \right\} / (1 + 3 (a/L)^3)^2$$

$$\Theta_5 = 36/35 \left\{ 1 + 3/8 (a/L)^3 [35 + 70 (a/L)^2 + 63 (a/L)^4] \right\} / (1 + 3 (a/L)^3)^3$$

Fig. 2.8 - Definition of the variables used by Williams in correcting the classical beam theory equations for calculating compliance and G. [33]

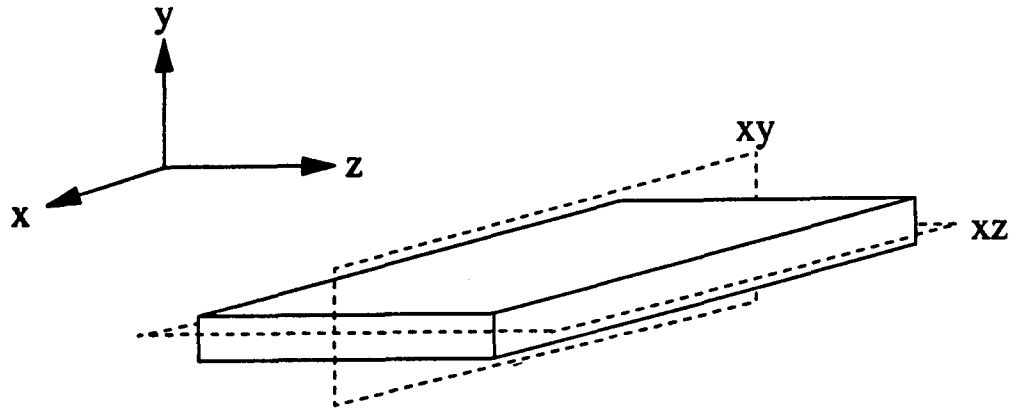


Fig. 2.9 - Definition of the planes of symmetry that exist in a specially orthotropic laminate. The fibres run in the x-direction.

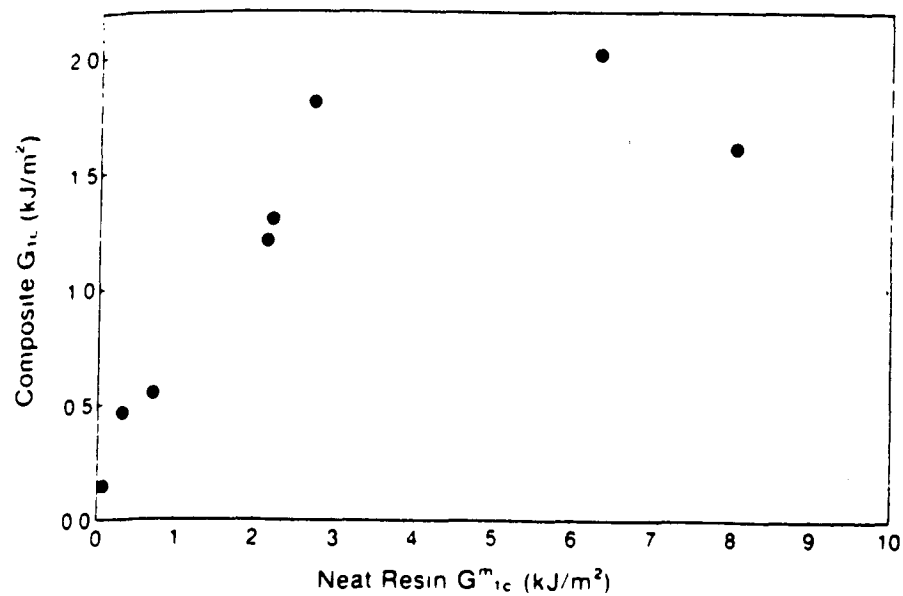


Fig. 3.1 - Mode I delamination fracture toughness of a composite as a function of the toughness of its resin. This graph shows that there is a practical limit above which increased resin toughness does not translate into significantly increased composite toughness. [11]

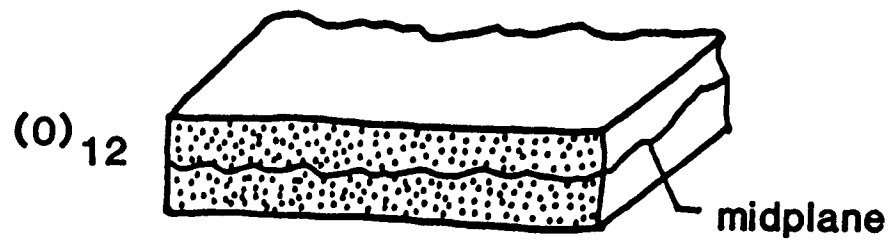


Fig. 3.2 - Schematic showing fibre nesting between two layers of a unidirectional laminate. [27]

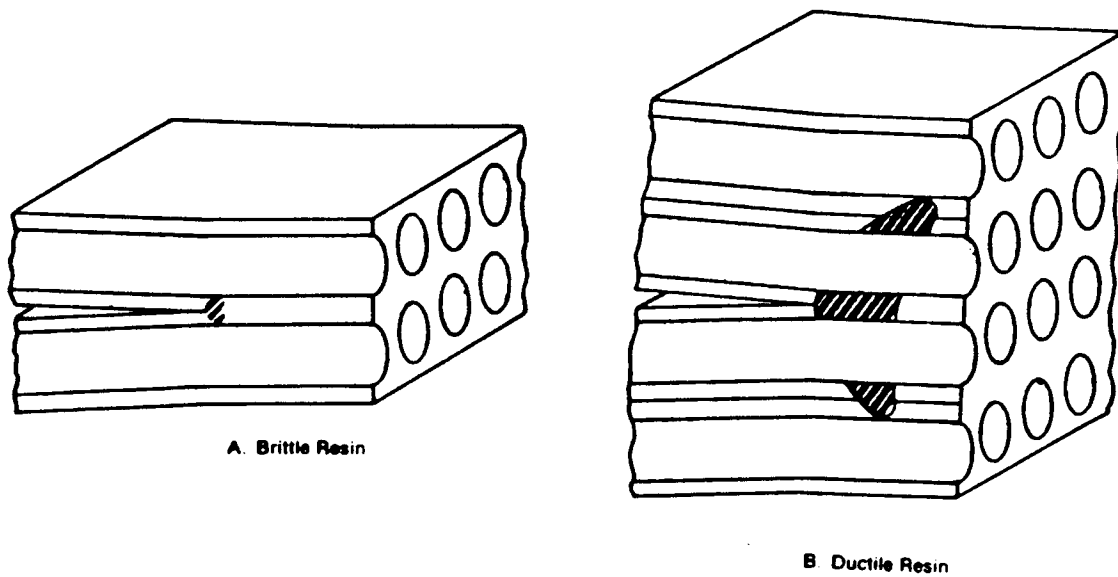


Fig. 3.3 - Schematic showing the difference in crack tip damage zone size between a brittle and a ductile resin system. [13]

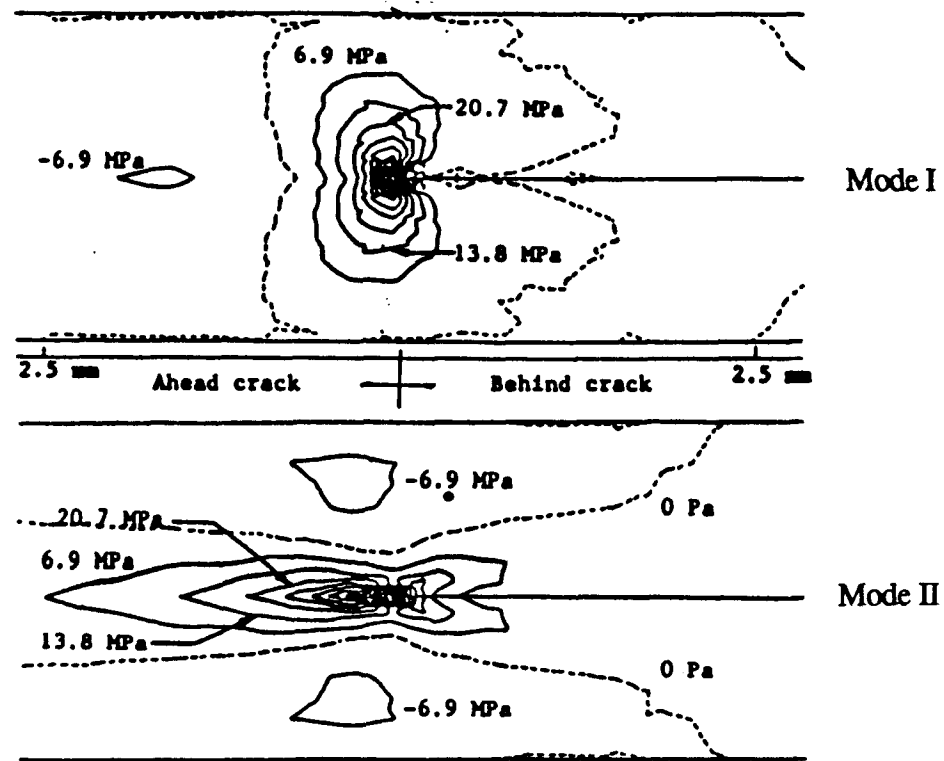


Fig. 3.4 - Stress contour plots near the crack tip in both Mode I and Mode II. Note the different shapes of the contours, and how the Mode II stresses extend further ahead of the crack tip. Thus we would expect the  $r^{1/2}$  singularity to dominate further ahead of the crack tip in Mode II. [45]

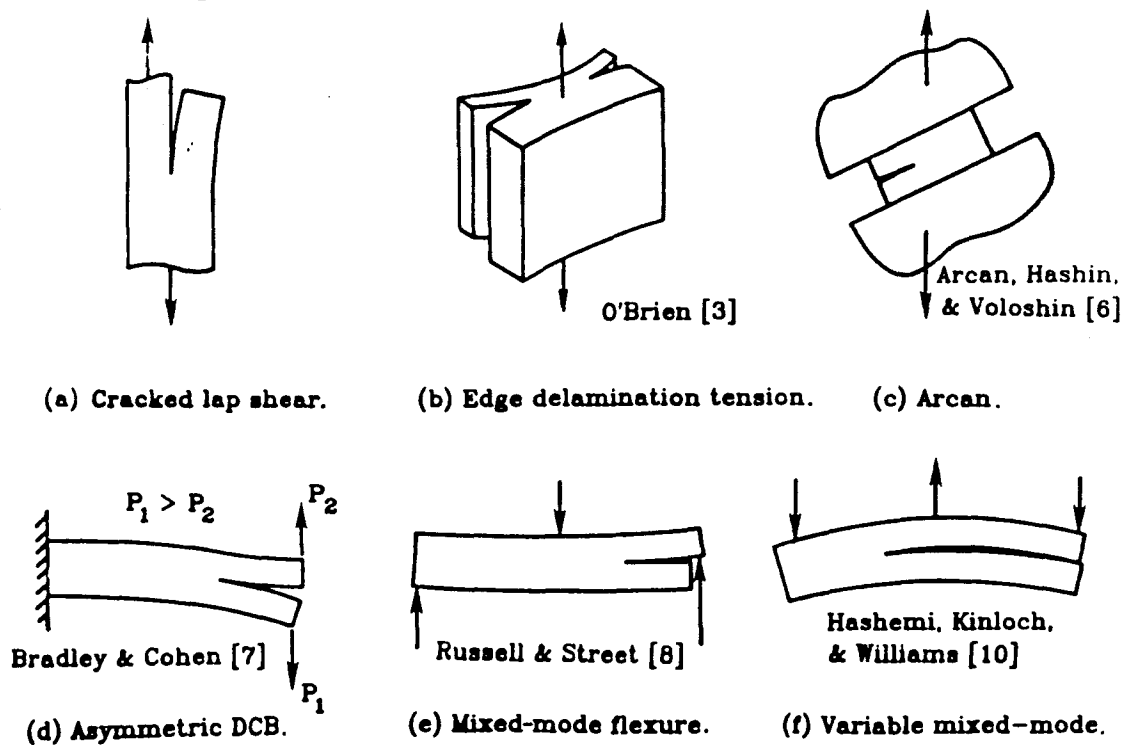


Fig. 3.5 - Schematic showing several test specimen geometries that have been used to conduct testing under mixed Mode I and II loading. [48]

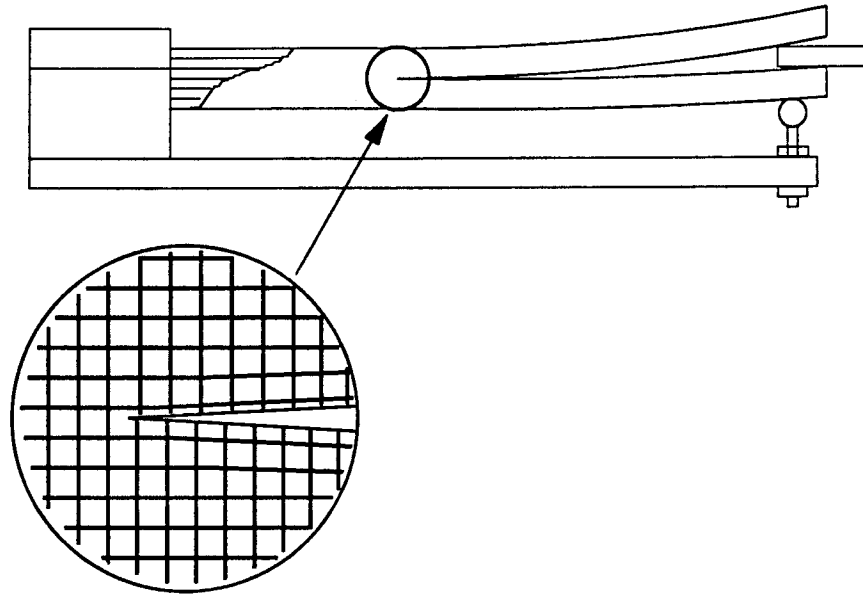


Fig. 4.1 - Schematic of the loading jig used in this study for applying both Mode I and II loads. Inset depicts the grid at the crack tip under load.



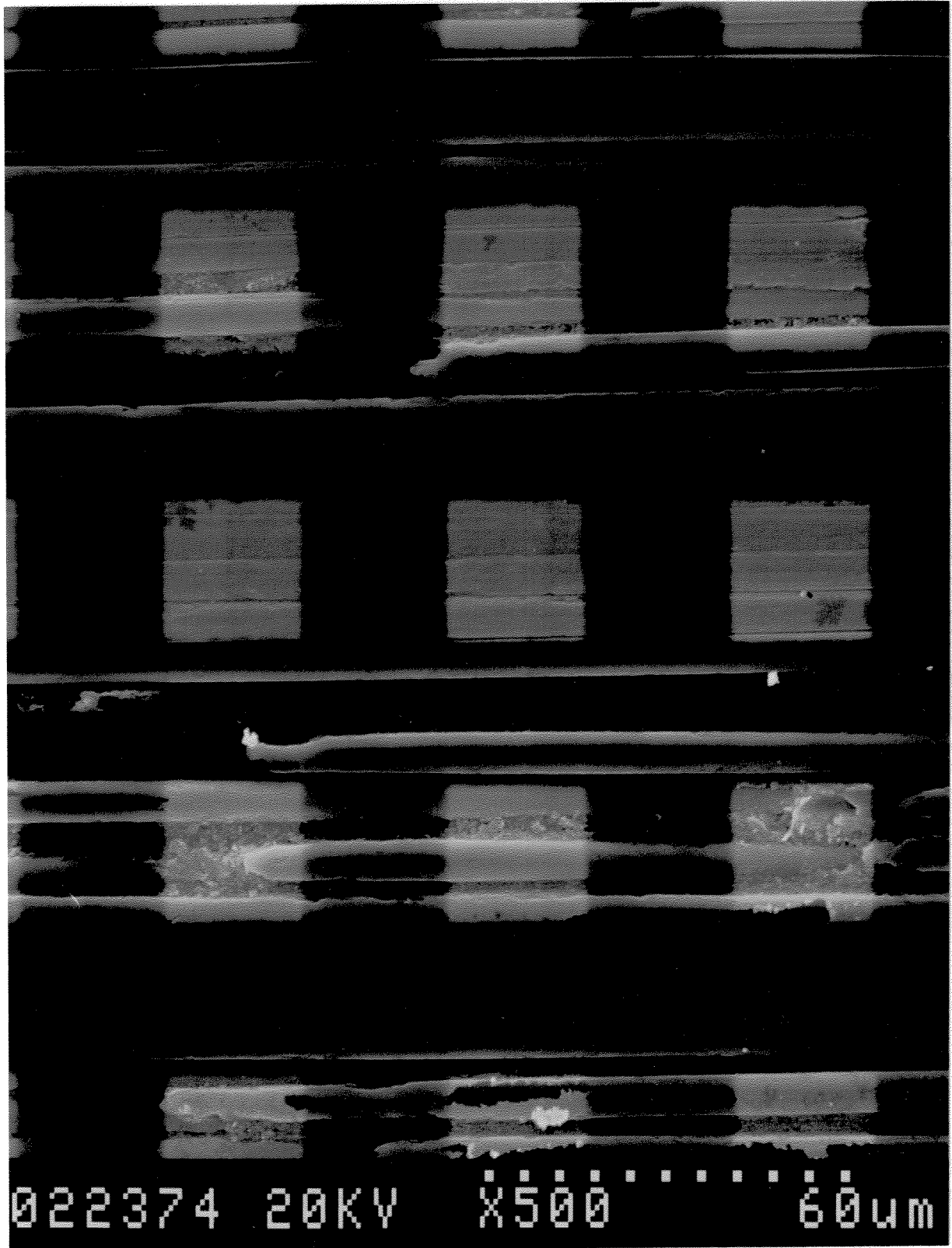


Fig. 4.2 - Photograph of an undeformed grid as was used for measurements.

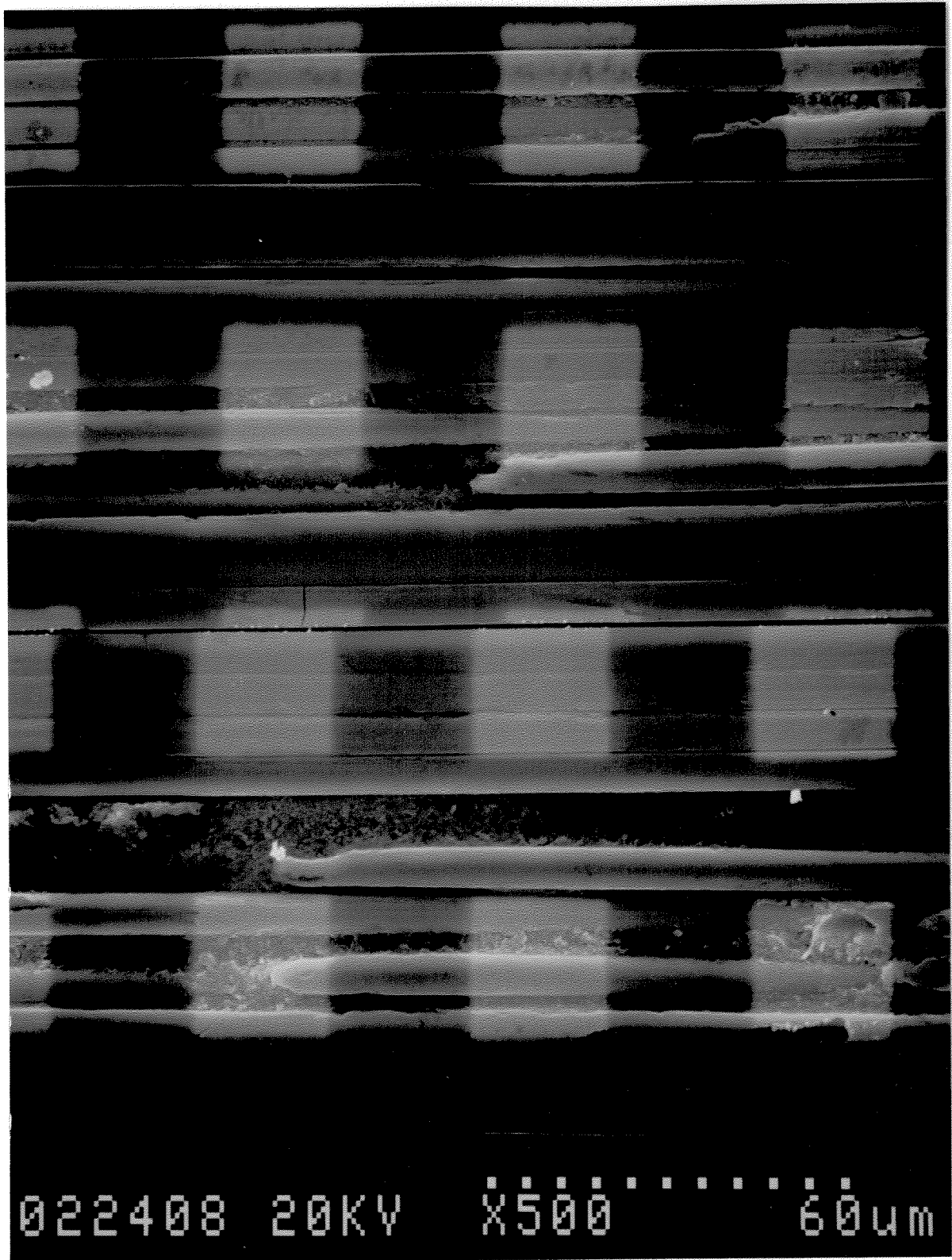


Fig.4.3 - Photograph of a deformed grid as was used for the measurements.

Offset (microns)	$\alpha_I$ $\times 10^4$ ( $m^{1/2}$ )	$\beta_I$ ( $m^{-1/2}$ )	$R^2$
-50	1.55	0.184	0.939
-40	1.67	0.164	0.941
-30	1.80	0.142	0.944
-20	1.94	0.114	0.946
-10	2.09	0.081	0.946
0	2.26	0.042	0.944
10	2.40	0.011	0.891
20	2.53	-0.019	0.868
30	2.66	-0.048	0.844

Table 1 - Effect on the constants of moving crack tip location of the curve fit of COD vs  $r^{1/2} + r^{3/2}$ .

Range (microns)	$\alpha_1$ $\times 10^4$ ( $m^{1/2}$ )	$\beta_1$ ( $m^{-1/2}$ )	$R^2$
167.9	2.88	-0.428	0.895
223.9	2.79	-0.326	0.922
279.9	2.5	-0.108	.0906
335.8	2.36	-0.014	.0925
391.8	2.26	0.042	.0944
447.8	2.29	0.028	0.949
503.7	2.28	0.031	0.960
559.7	2.26	0.037	0.967
615.7	2.14	0.077	0.965
671.6	2.01	0.118	0.964
727.6	1.95	0.135	0.969
783.6	1.99	0.125	0.972
839.6	1.96	0.131	0.973
895.5	1.92	0.141	0.976
951.5	1.90	0.145	.0980

Table 2 - Effect on the constants of varying the range over which the curve fit of COD vs  $r^{1/2}+r^{3/2}$  is done.

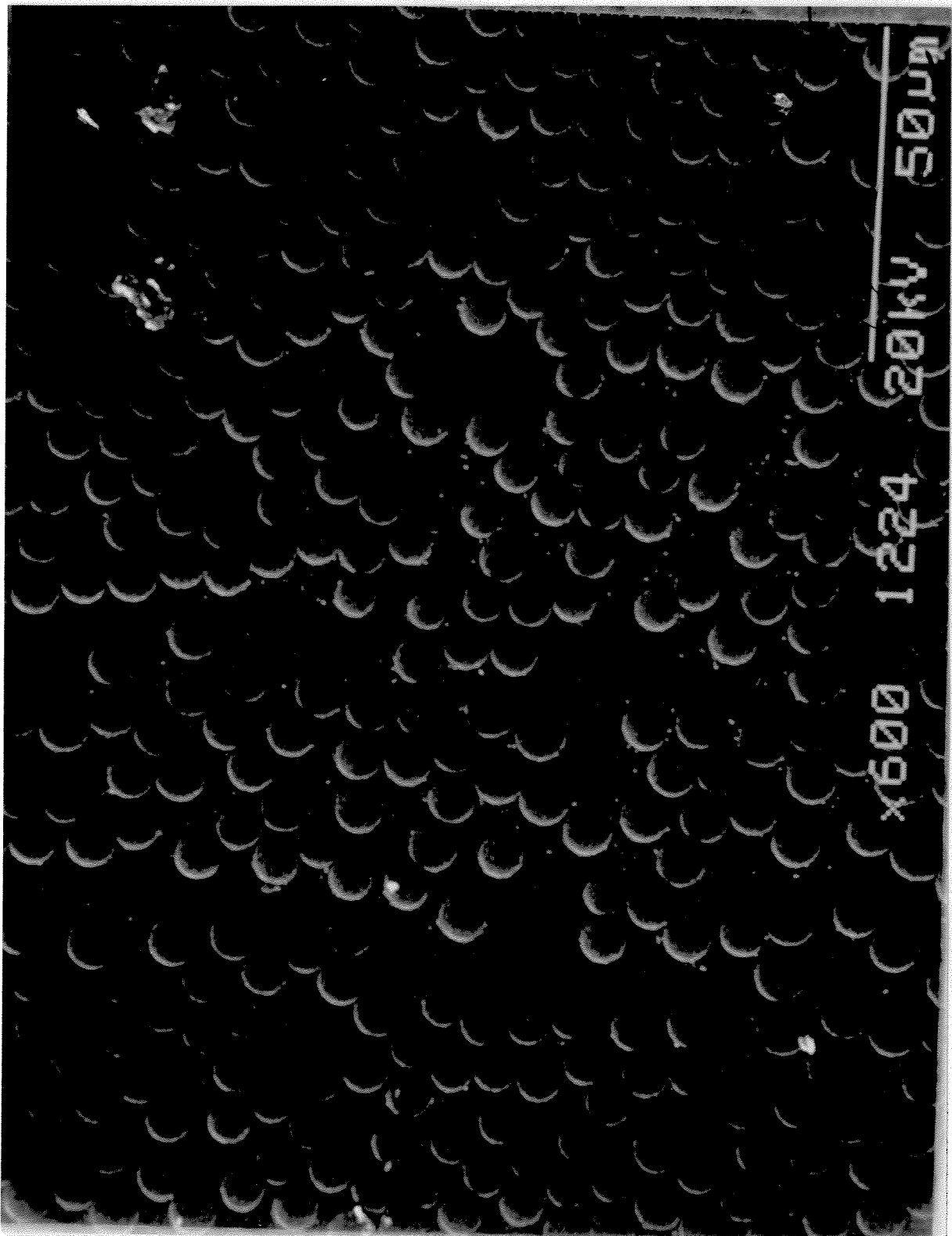


Fig. 4.4 - Photograph of cross-section of DREP specimen 1 used to determine the fibre volume fraction.

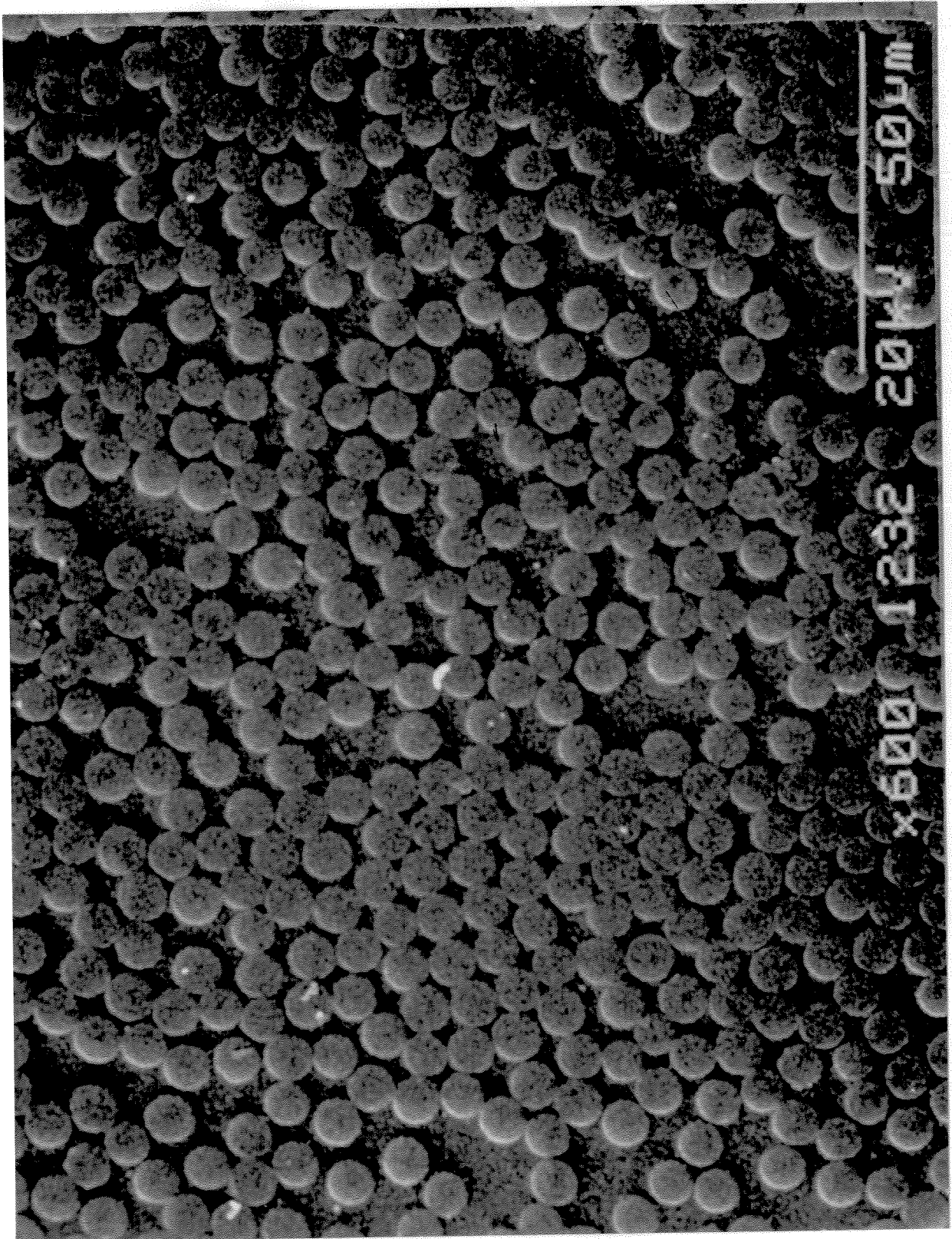


Fig. 4.5 - Photograph of cross-section of NASA specimen 4 used to determine the fibre volume fraction.

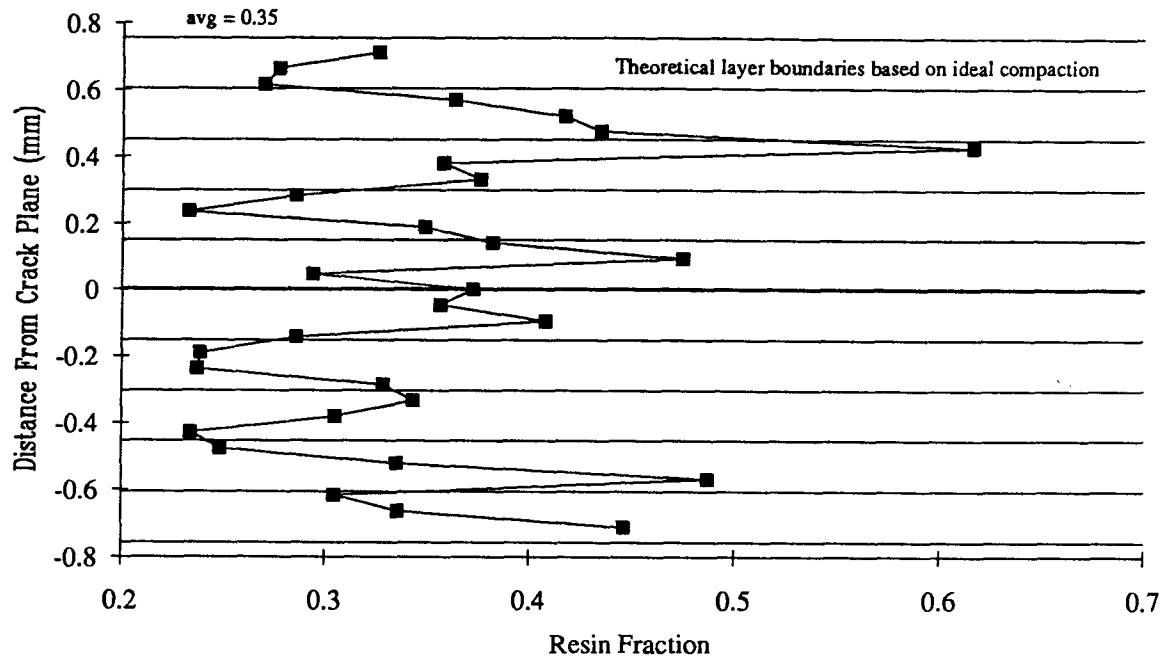


Fig. 4.6 - Plot of the variation of resin fraction through the thickness of specimen 1, near the crack plane. Horizontal lines indicate the locations of layer boundaries assuming uniform compaction, calculated as total thickness divided by the number of plies.

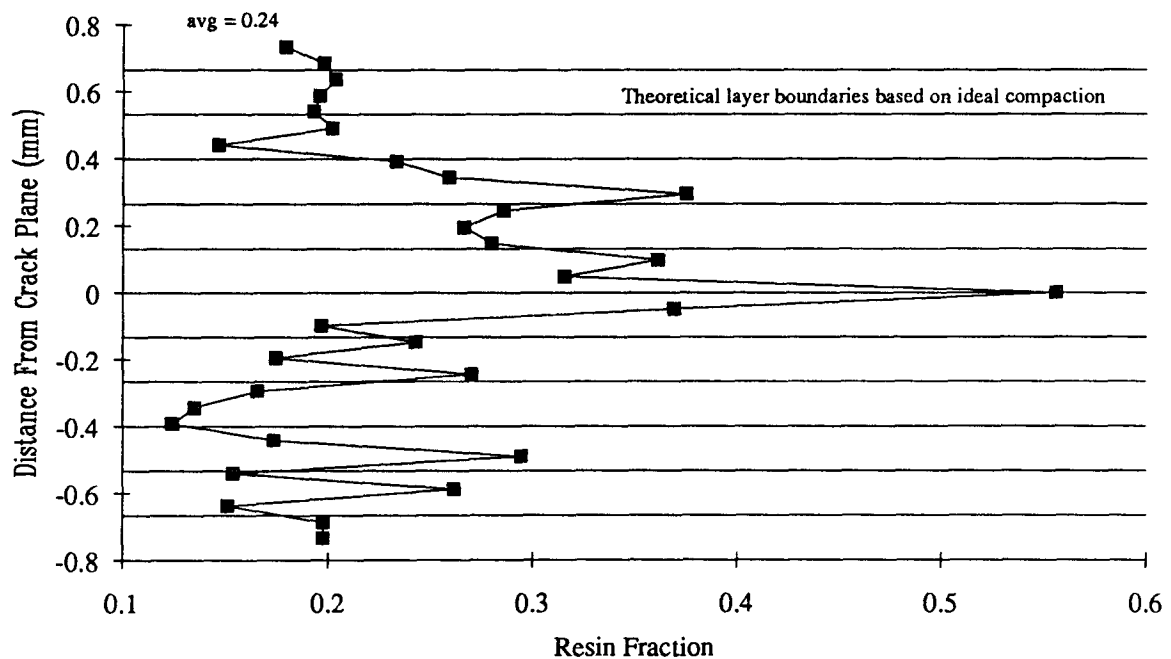


Fig. 4.7 - Plot of the variation of resin fraction through the thickness of specimen 4, near the crack plane. Horizontal lines indicate the locations of layer boundaries assuming uniform compaction, calculated as total thickness divided by the number of plies.

Specimen	1 (DREP)	3 (DREP)	4 (NASA)
Total Thickness(mm)	3.517	3.480	3.007
upper 1/2 beam(%)	1.646(46.8)	1.739(49.97)	1.461(48.59)
lower 1/2 beam(%)	1.871(53.2)	1.741(50.03)	1.547(51.41)
Applied Deflection(mm)	1.64	1.01	1.27
Traced Projection(mm)			
upper 1/2 beam(%)	0.87(56.5)	0.44(44.4)	0.68(53.5)
lower 1/2 beam(%)	0.67(43.5)	0.55(55.6)	0.59(46.5)
Base Clearance(mm)			
upper 1/2 beam(%)	0.91(55.5)	0.39(38.7)	0.64(50.4)
lower 1/2 beam(%)	0.73(44.5)	0.62(61.3)	0.63(49.6)

Table 3 - Variation in specimen dimensions and response, as found for two DREP and one NASA specimens.



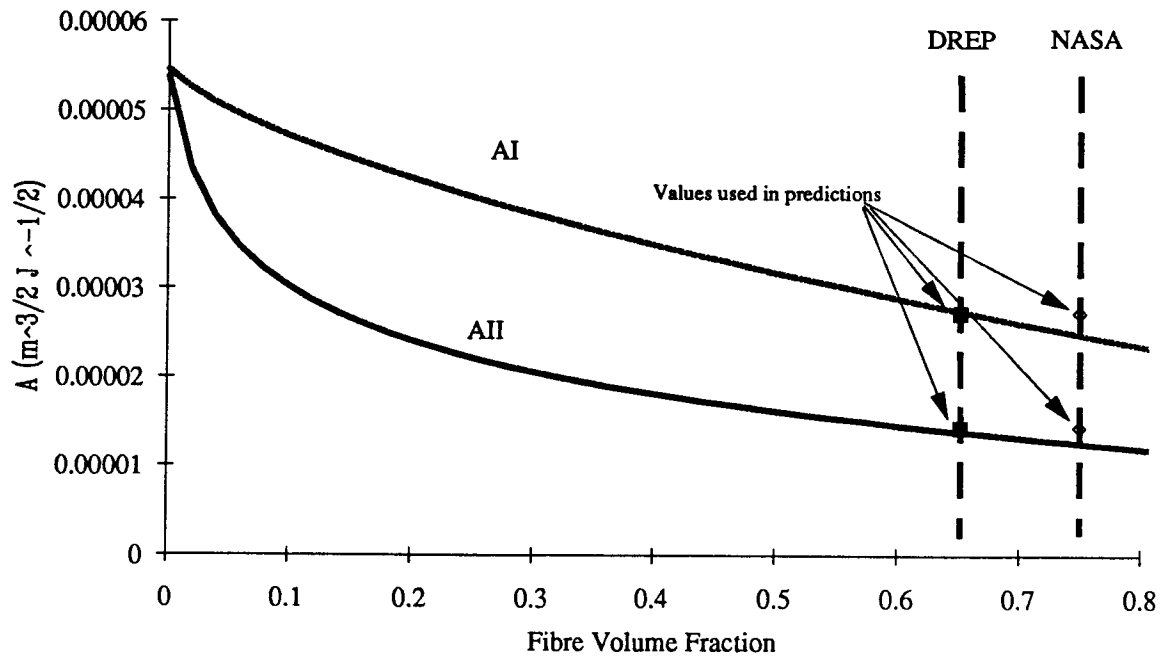


Fig.4.8 - Plot of the orthotropic constants,  $A_I$  and  $A_{II}$  as a function of fibre volume fraction. Vertical lines represent the average volume fractions for the DREP and NASA specimens, while the markers indicate the actual values used in the LEFM calculation of  $G$ .

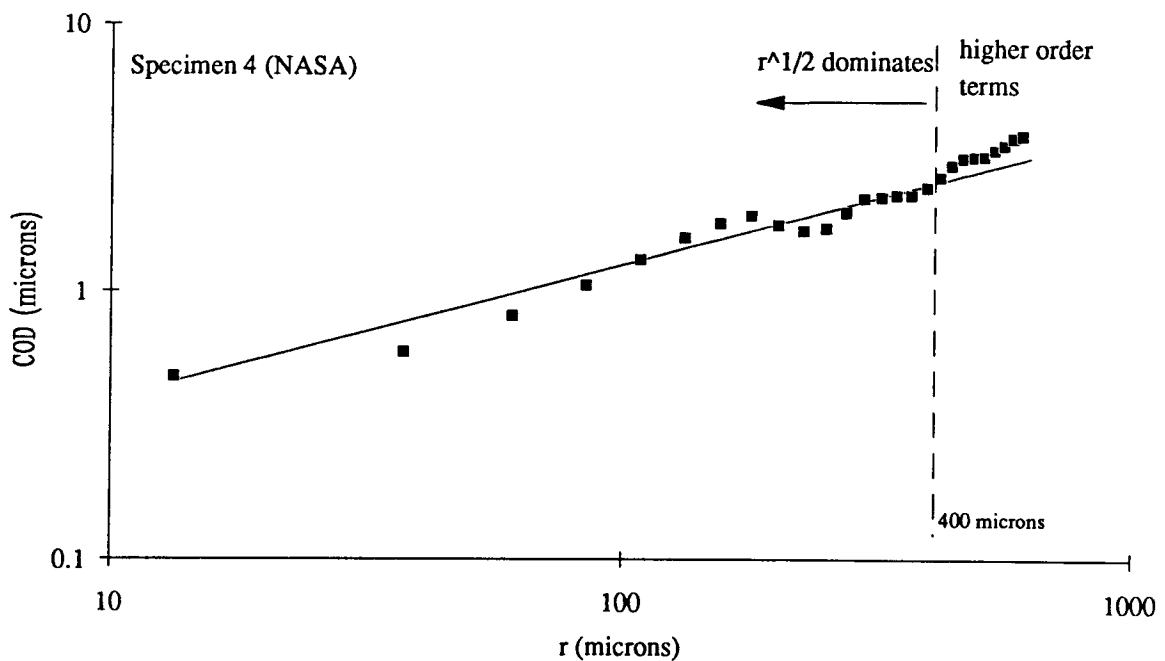


Fig. 5.1 - Log-log plot of COD vs  $r$  for an applied  $G_I$  of  $33 \text{ J/m}^2$  on specimen 4 (NASA). A square root displacement singularity fits the data over the first 400 microns.

Specimen	SEM Crack Length (mm)	Visual Crack (mm)		
		Front	Center	Back
1	44.12	44.20		38.60
1	52.04	47.98		40.35
1	59.91	56.38		51.99
3	37.62	40.06		38.90
3	73.97	71.48		67.65
4	57.31	57.65	59.10	55.56
4	67.44	71.20	71.61	63.09
5	47.47	51.89	53.13	51.00
7	40.69	41.91	42.32	39.81
7	53.72	53.99	55.16	50.69

Table 4 - Crack front curvatures measured visually after specimens were pulled apart. Front refers to the side of the specimen on which the measurements were made. Where there is no center measurement it indicates that the crack front did not bow out in the middle.

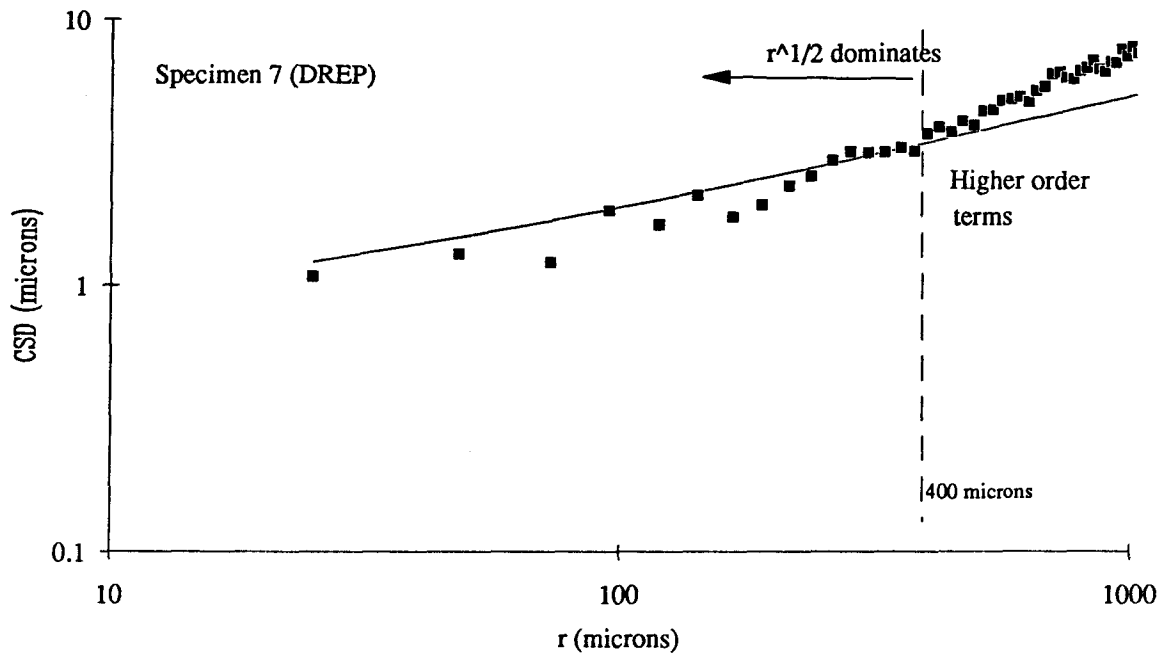


Fig. 5.2 - Log-log plot of CSD vs  $r$  for an applied  $G_{II}$  of  $350 \text{ J/m}^2$  on specimen 7 (DREP). A square root displacement singularity fits the data over the first 400 microns.

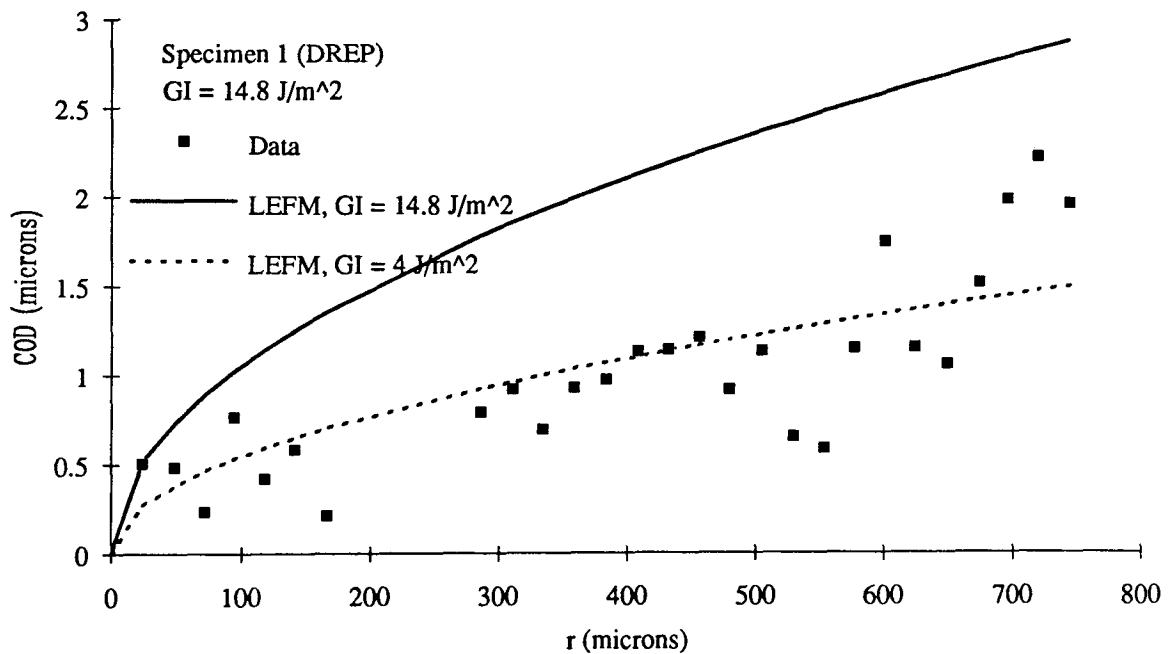


Fig. 5.3 - Plot of COD vs  $r$  for an applied  $G_I$  of  $14.8 \text{ J/m}^2$  on specimen 1 (DREP). Solid line shows orthotropic prediction based on globally applied  $G$ . Dashed line represents best fit line and gives local  $G$  seen at the crack tip.

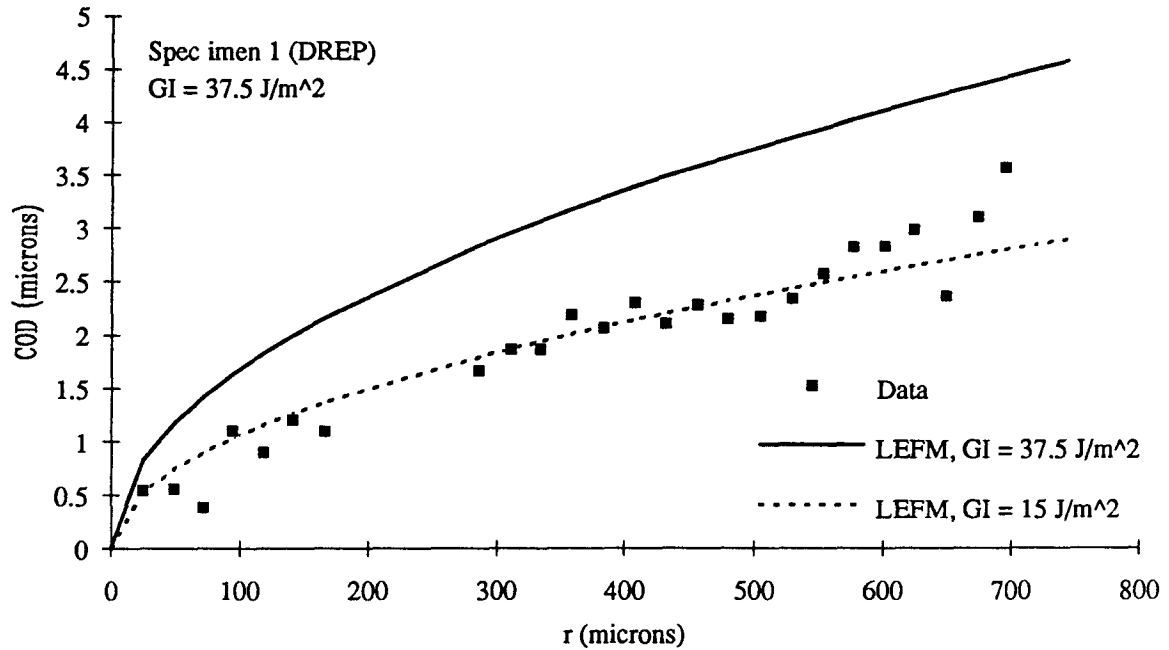


Fig. 5.4 - Plot of COD vs r for an applied  $G_I$  of 37.5 J/m<sup>2</sup> on specimen 1 (DREP). Solid line shows orthotropic prediction based on globally applied  $G$ . Dashed line represents best fit line and gives local  $G$  seen at the crack tip.

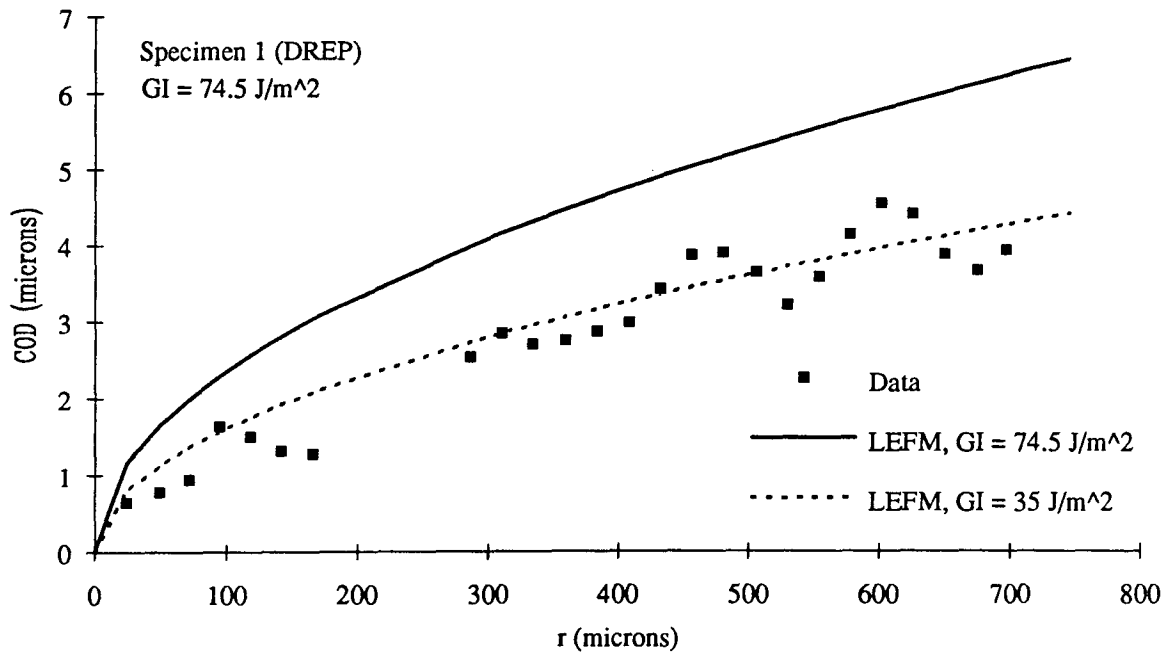


Fig. 5.5 - Plot of COD vs r for an applied  $G_I$  of 74.5 J/m<sup>2</sup> on specimen 1 (DREP). Solid line shows orthotropic prediction based on globally applied  $G$ . Dashed line represents best fit line and gives local  $G$  seen at the crack tip.

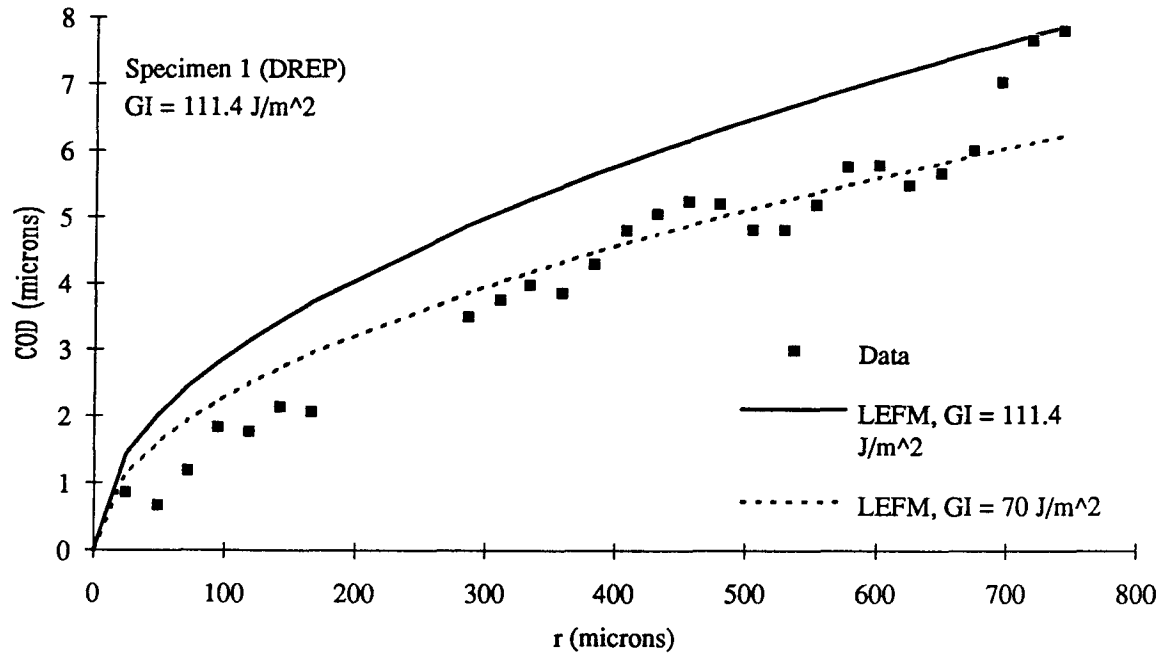


Fig. 5.6 - Plot of COD vs  $r$  for an applied  $G_I$  of  $111.4 \text{ J/m}^2$  on specimen 1 (DREP). Solid line shows orthotropic prediction based on globally applied  $G$ . Dashed line represents best fit line and gives local  $G$  seen at the crack tip.

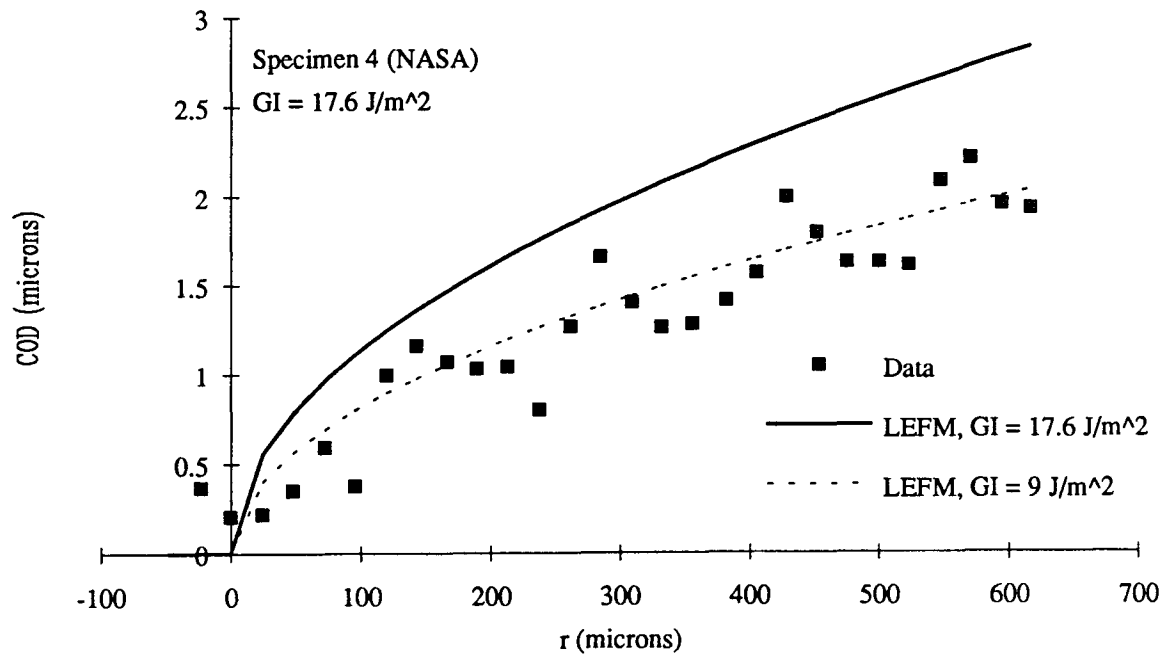


Fig. 5.7 - Plot of COD vs  $r$  for an applied  $G_I$  of  $17.6 \text{ J/m}^2$  on specimen 4 (NASA). Solid line shows orthotropic prediction based on globally applied  $G$ . Dashed line represents best fit line and gives local  $G$  seen at the crack tip.

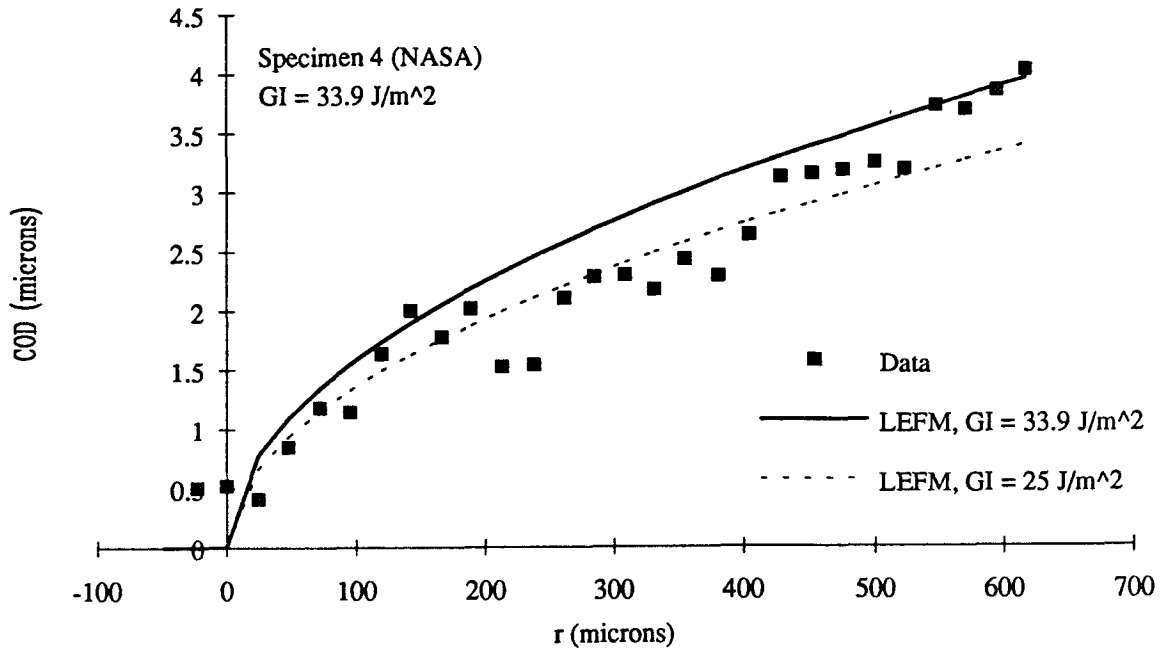


Fig. 5.8 - Plot of COD vs  $r$  for an applied  $G_I$  of 33.9 J/m<sup>2</sup> on specimen 4 (NASA). Solid line shows orthotropic prediction based on globally applied  $G$ . Dashed line represents best fit line and gives local  $G$  seen at the crack tip.

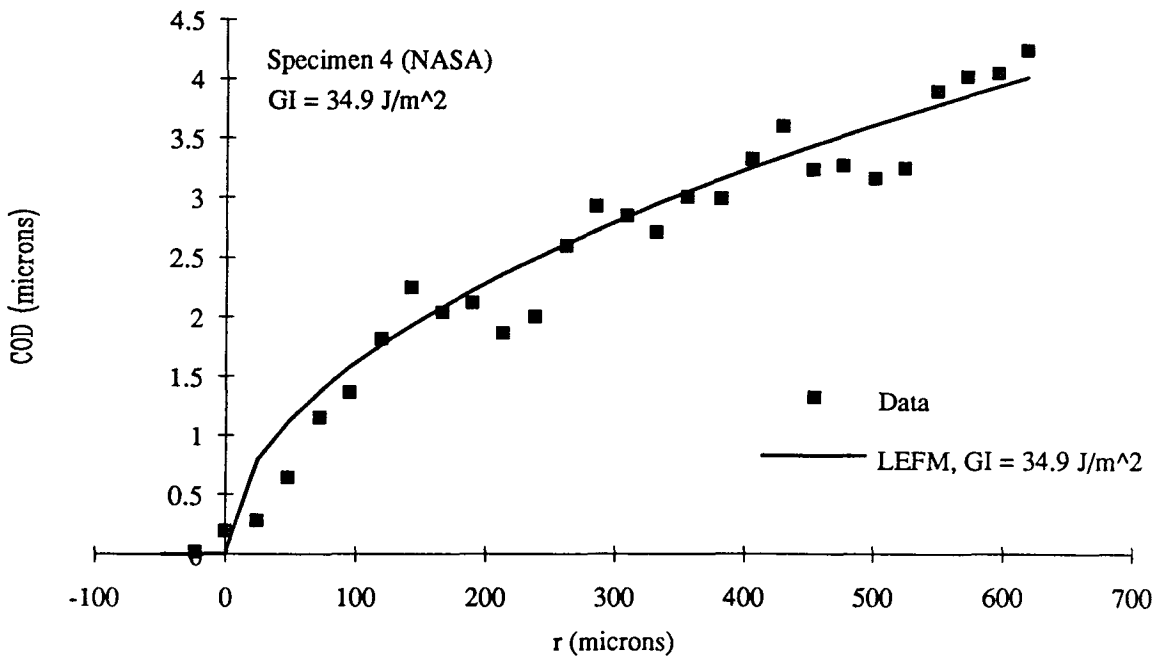


Fig. 5.9 - Plot of COD vs  $r$  for an applied  $G_I$  of 34.9 J/m<sup>2</sup> on specimen 4 (NASA). In this case the orthotropic prediction provides a reasonable fit to the data.

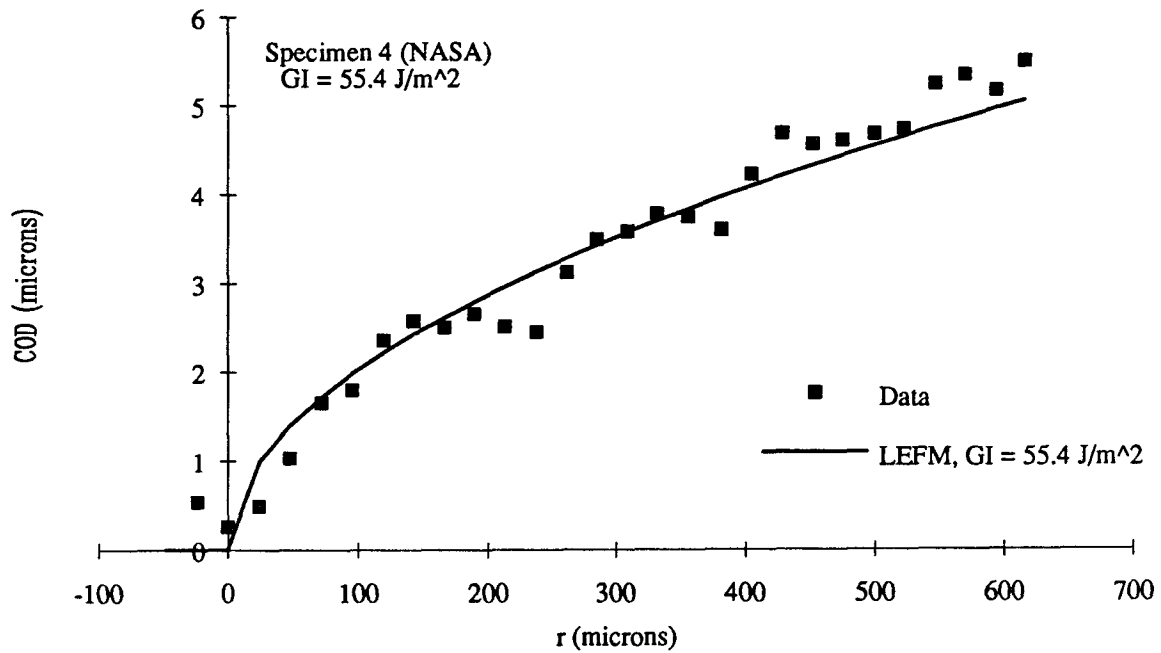


Fig. 5.10 - Plot of COD vs  $r$  for an applied  $G_I$  of  $55.4 \text{ J/m}^2$  on specimen 4 (NASA). In this case the orthotropic prediction provides a reasonable fit to the data.

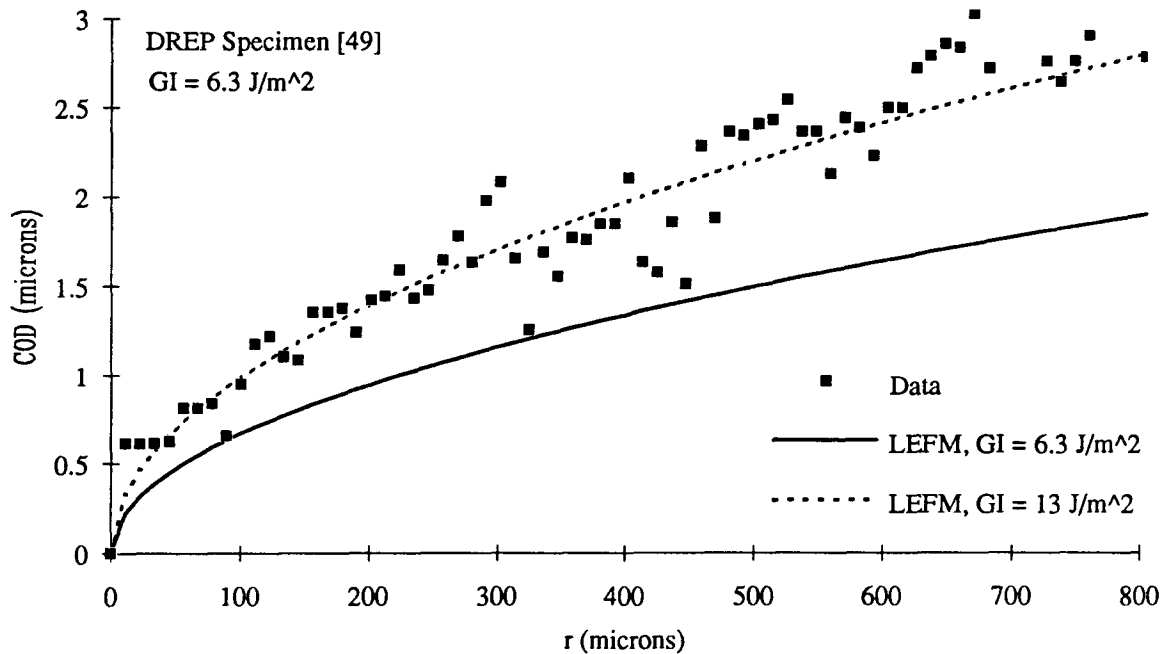


Fig. 5.11 - Plot of COD vs  $r$  for an applied  $G_I$  of  $6.3 \text{ J/m}^2$  on a DREP specimen [49]. Solid line shows orthotropic prediction based on globally applied  $G$ . Dashed line represents best fit line and gives local  $G$  seen at the crack tip.

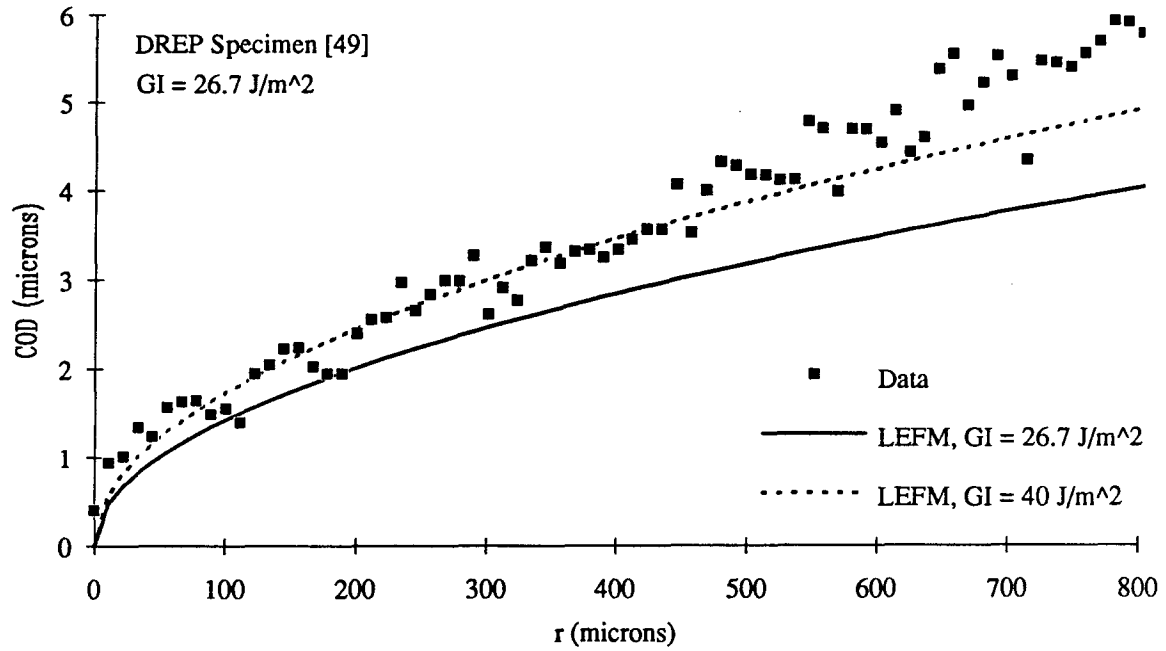


Fig. 5.12 - Plot of COD vs  $r$  for an applied  $G_I$  of  $26.7 \text{ J/m}^2$  on a DREP specimen [49]. Solid line shows orthotropic prediction based on globally applied  $G$ . Dashed line represents best fit line and gives local  $G$  seen at the crack tip.

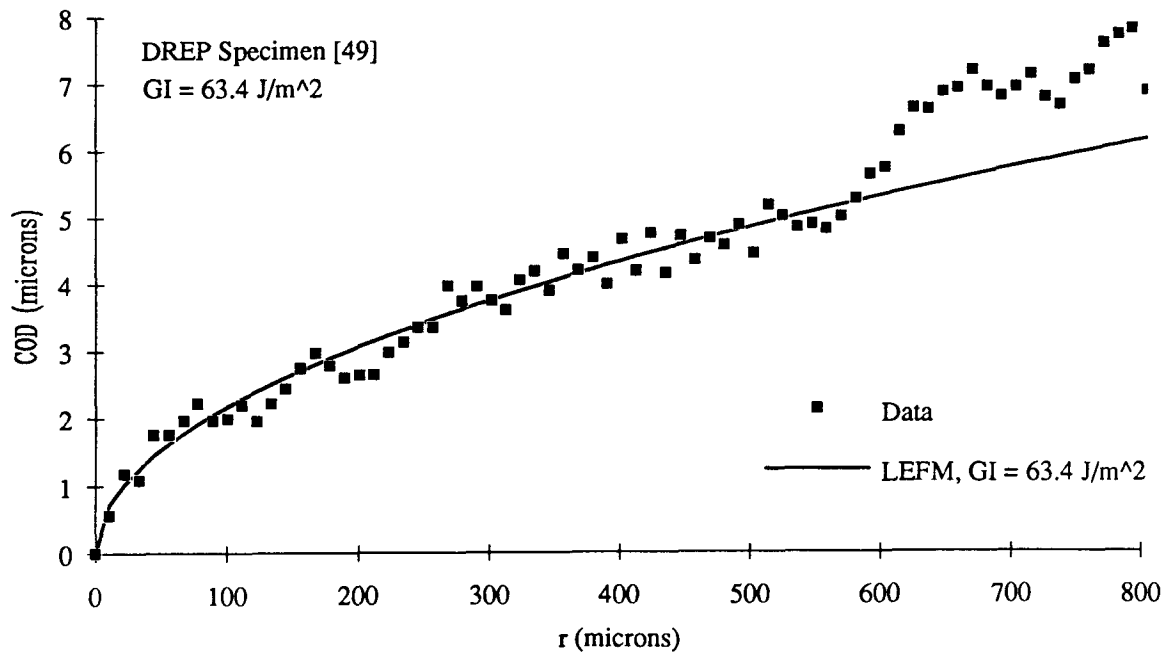


Fig. 5.13 - Plot of COD vs  $r$  for an applied  $G_I$  of  $63.4 \text{ J/m}^2$  on a DREP specimen [49]. In this case the orthotropic prediction provides a good estimate of the data.



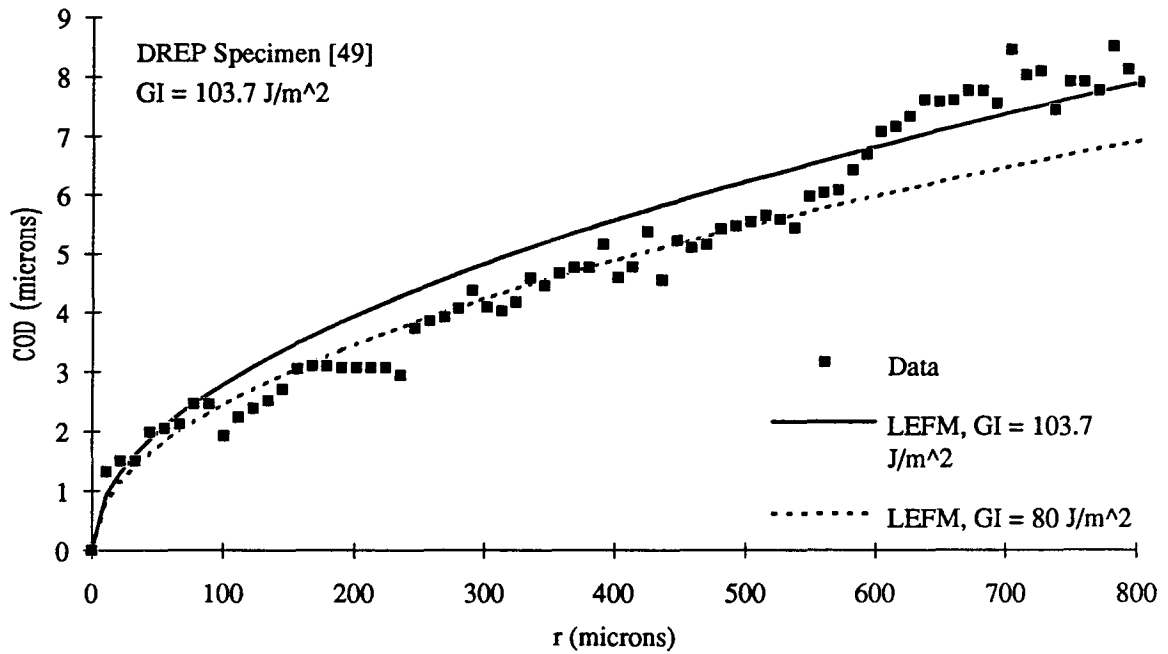


Fig. 5.14 - Plot of COD vs  $r$  for an applied  $G_I$  of  $103.7 \text{ J/m}^2$  on a DREP specimen [49]. Solid line shows orthotropic prediction based on globally applied  $G$ . Dashed line represents best fit line and gives local  $G$  seen at the crack tip.

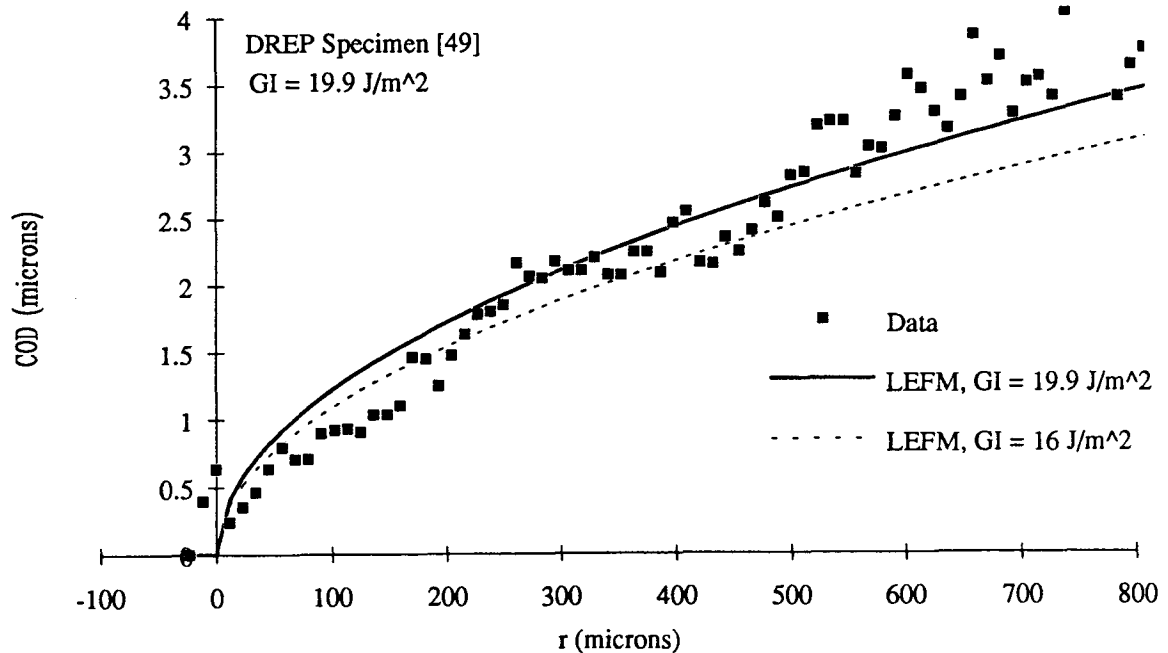


Fig. 5.15 - Plot of COD vs  $r$  for an applied  $G_I$  of  $19.9 \text{ J/m}^2$  on a DREP specimen [49]. Solid line shows orthotropic prediction based on globally applied  $G$ . Dashed line represents best fit line and gives local  $G$  seen at the crack tip.

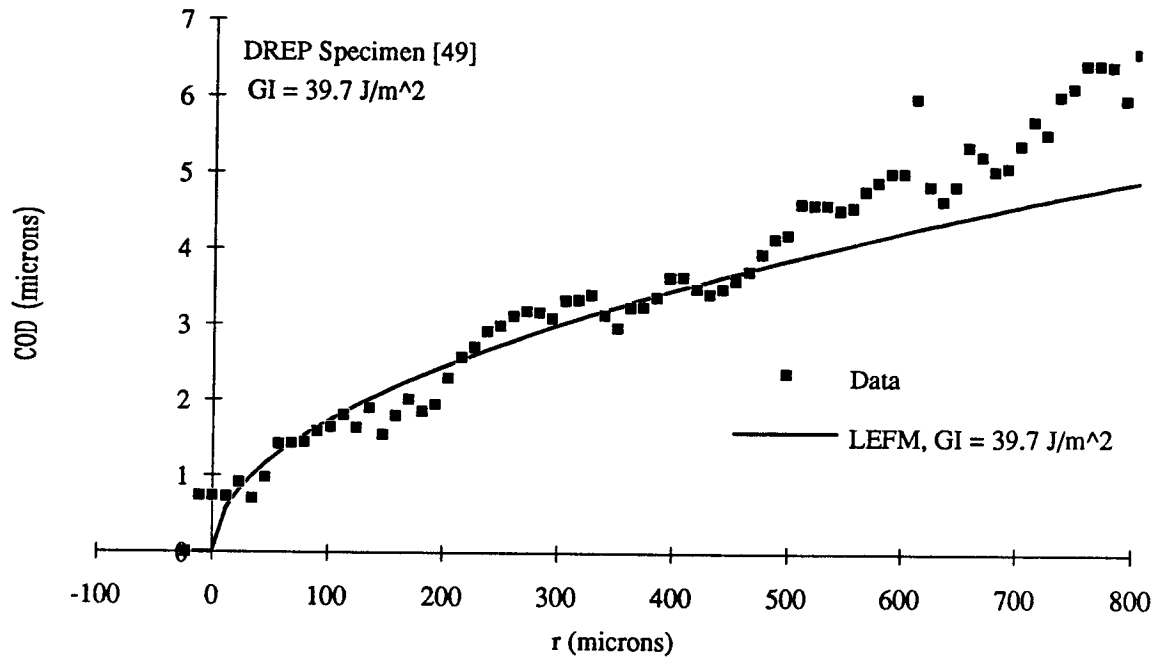


Fig. 5.16 - Plot of COD vs  $r$  for an applied  $G_I$  of  $39.7 \text{ J/m}^2$  on a DREP specimen [49]. In this case the orthotropic prediction provides a good estimate of the data.

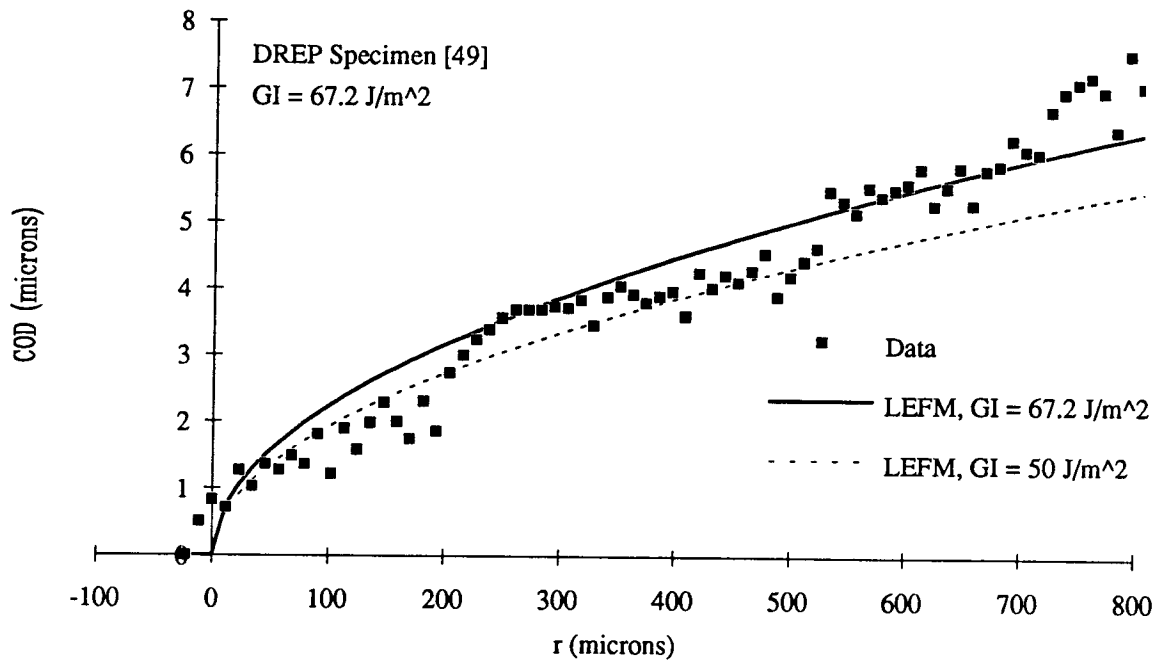


Fig. 5.17 - Plot of COD vs  $r$  for an applied  $G_I$  of  $67.2 \text{ J/m}^2$  on a DREP specimen [49]. Solid line shows orthotropic prediction based on globally applied  $G$ . Dashed line represents best fit line and gives local  $G$  seen at the crack tip.

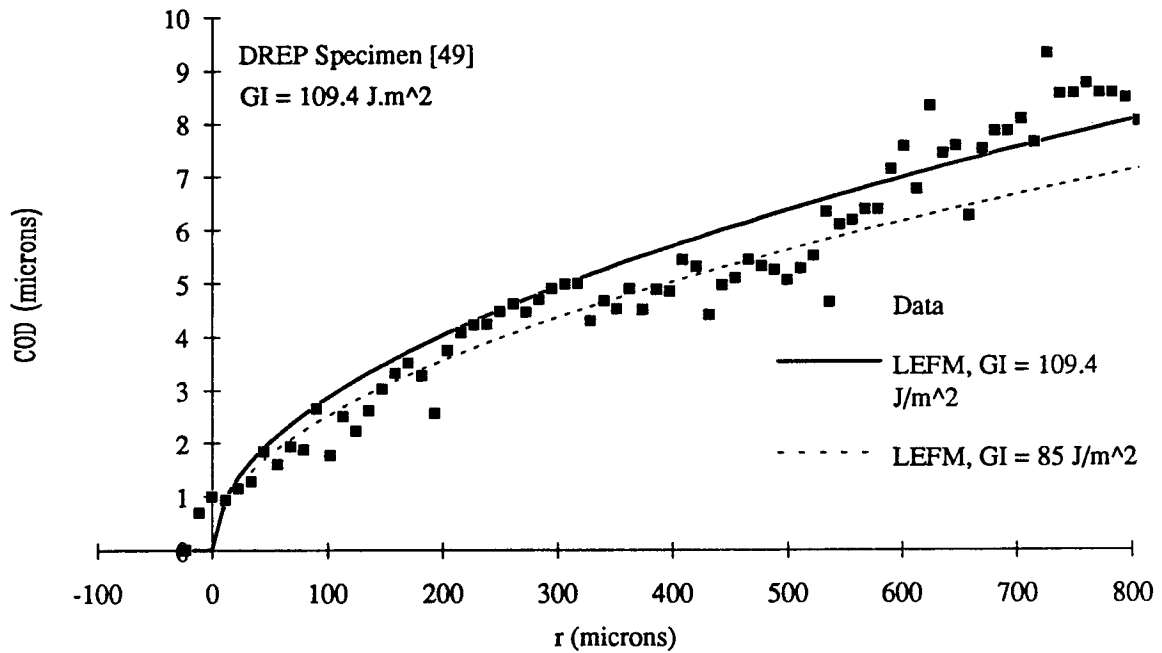


Fig. 5.18 - Plot of COD vs  $r$  for an applied  $G_I$  of  $109.4 \text{ J/m}^2$  on a DREP specimen [49]. Solid line shows orthotropic prediction based on globally applied  $G$ . Dashed line represents best fit line and gives local  $G$  seen at the crack tip.

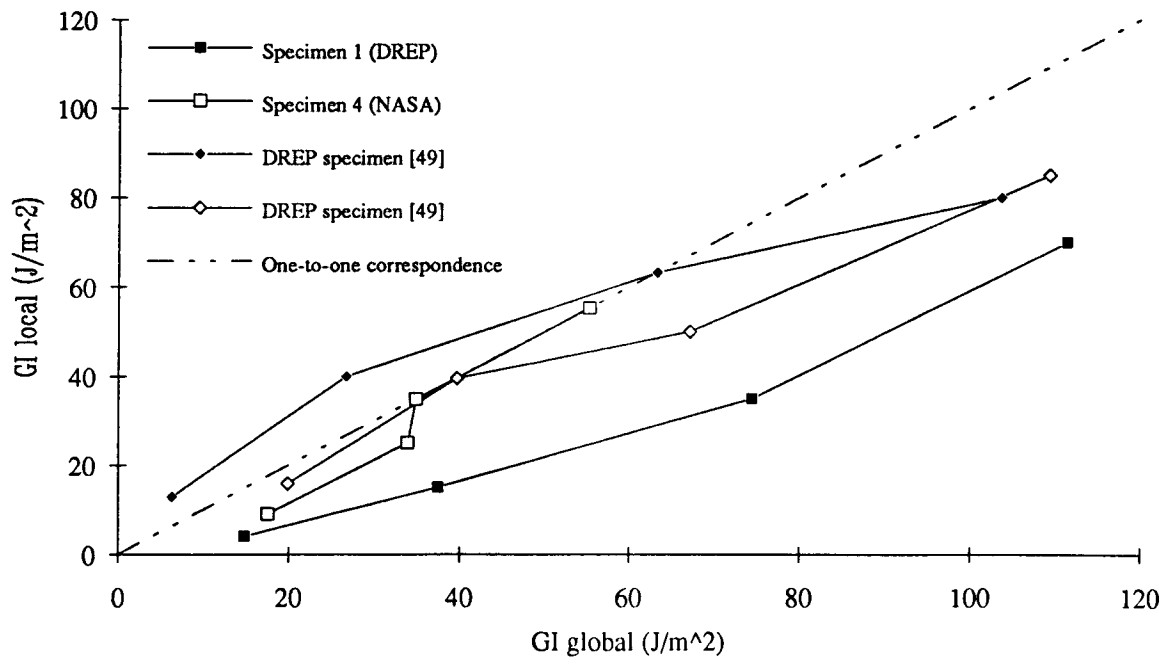


Fig. 5.19 - Plot of  $G_{I \text{ local}}$  vs  $G_{I \text{ global}}$ . Dashed line represents a 1-to-1 correspondence.

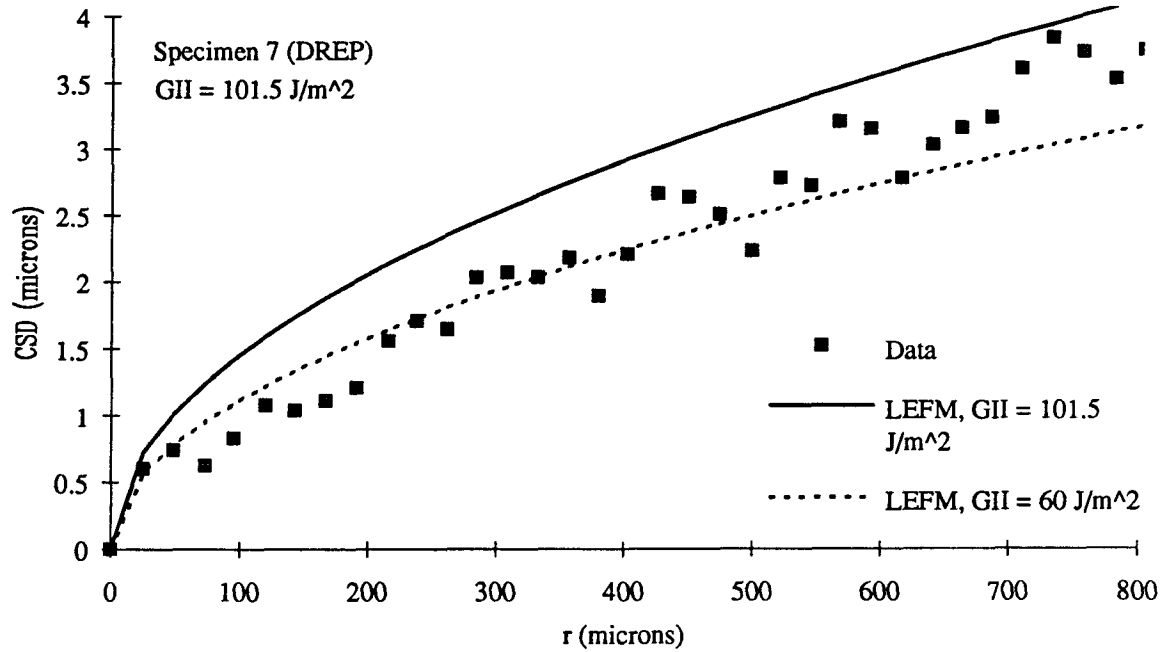


Fig. 5.20 - Plot of CSD vs  $r$  for an applied  $G_{II}$  of  $101.5 \text{ J/m}^2$  on specimen 7(DREP). Solid line shows orthotropic prediction based on globally applied  $G$ . Dashed line represents best fit line and gives local  $G$  seen at the crack tip.

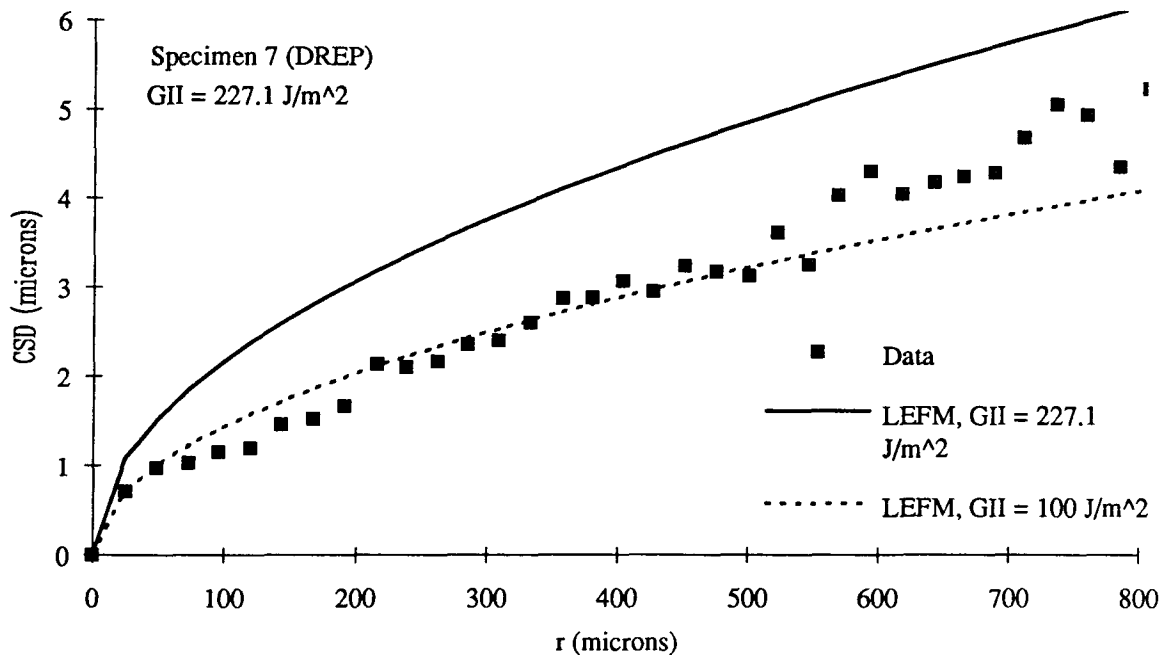


Fig. 5.21 - Plot of CSD vs  $r$  for an applied  $G_{II}$  of  $227.1 \text{ J/m}^2$  on specimen 7(DREP). Solid line shows orthotropic prediction based on globally applied  $G$ . Dashed line represents best fit line and gives local  $G$  seen at the crack tip.

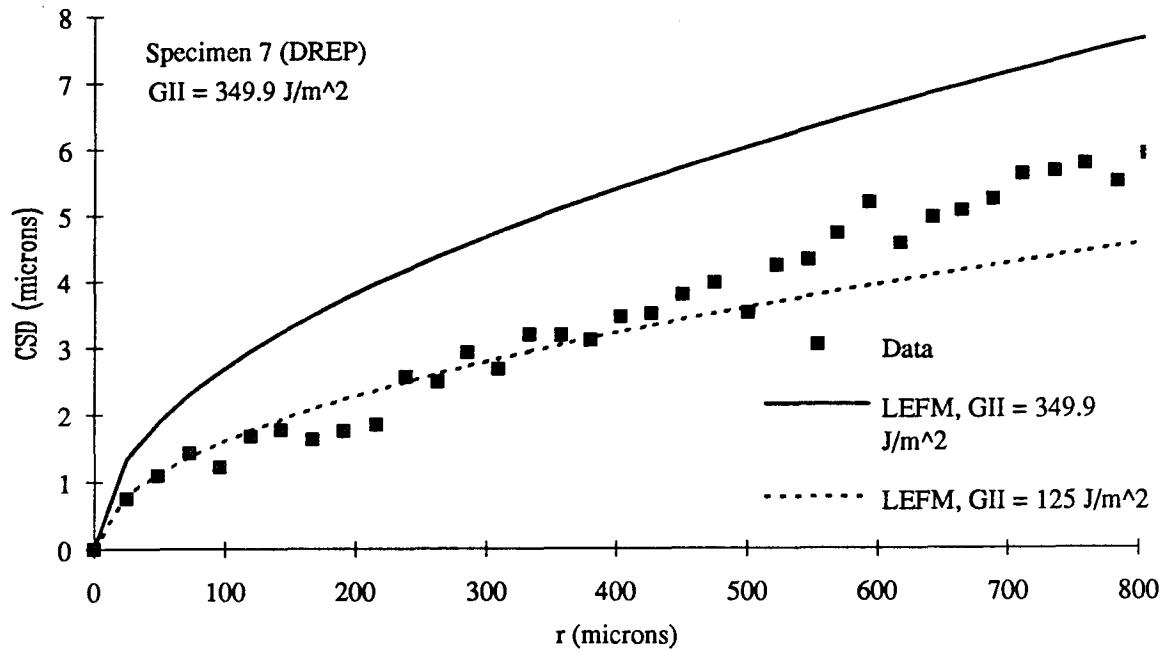


Fig. 5.22 - Plot of CSD vs  $r$  for an applied  $G_{II}$  of  $349.9 \text{ J/m}^2$  on specimen 7(DREP). Solid line shows orthotropic prediction based on globally applied  $G$ . Dashed line represents best fit line and gives local  $G$  seen at the crack tip.

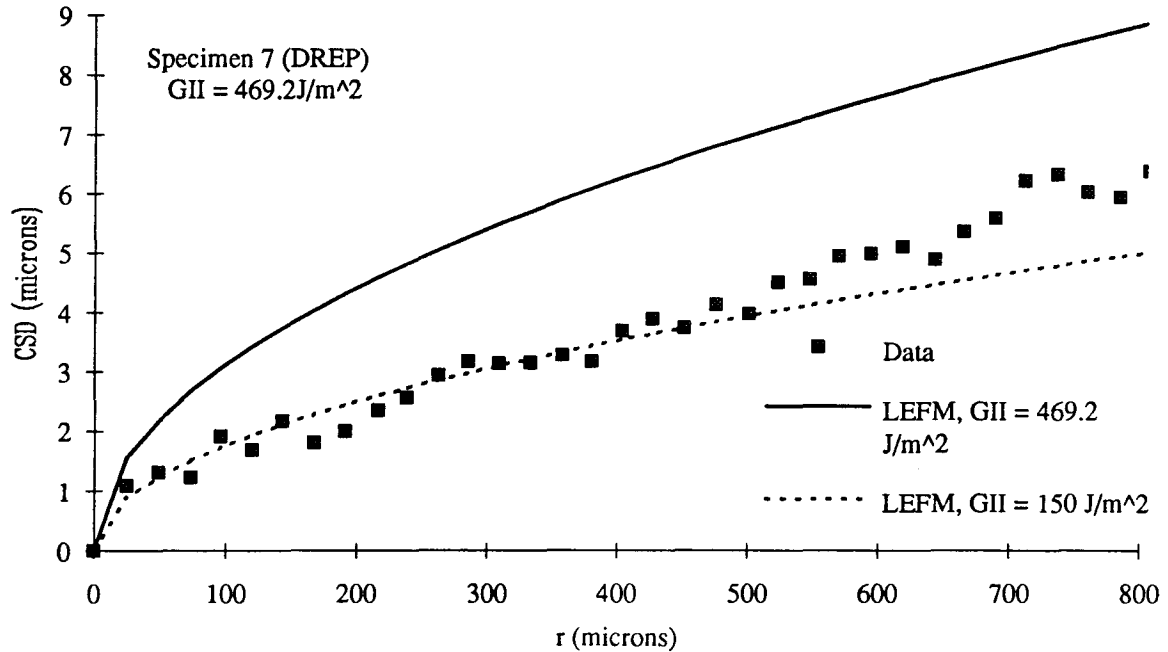


Fig. 5.23 - Plot of CSD vs  $r$  for an applied  $G_{II}$  of  $469.2 \text{ J/m}^2$  on specimen 7(DREP). Solid line shows orthotropic prediction based on globally applied  $G$ . Dashed line represents best fit line and gives local  $G$  seen at the crack tip.

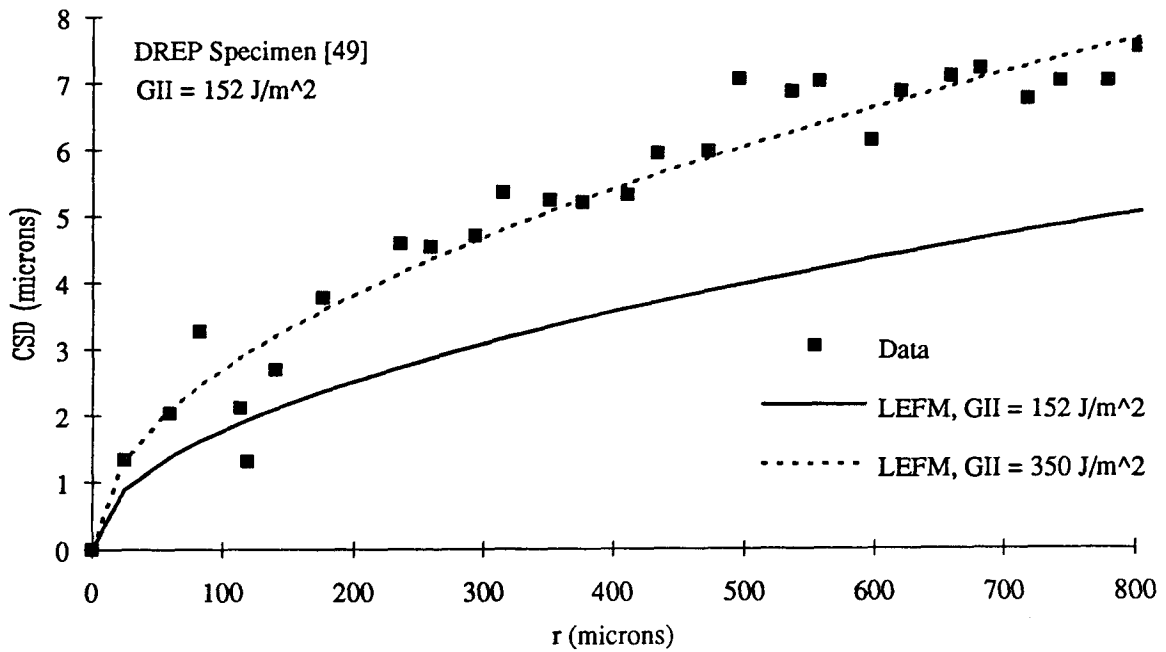


Fig. 5.24 - Plot of CSD vs  $r$  for an applied  $G_{II}$  of  $152 \text{ J/m}^2$  on a DREP specimen [49]. Solid line shows orthotropic prediction based on globally applied  $G$ . Dashed line represents best fit line and gives local  $G$  seen at the crack tip.

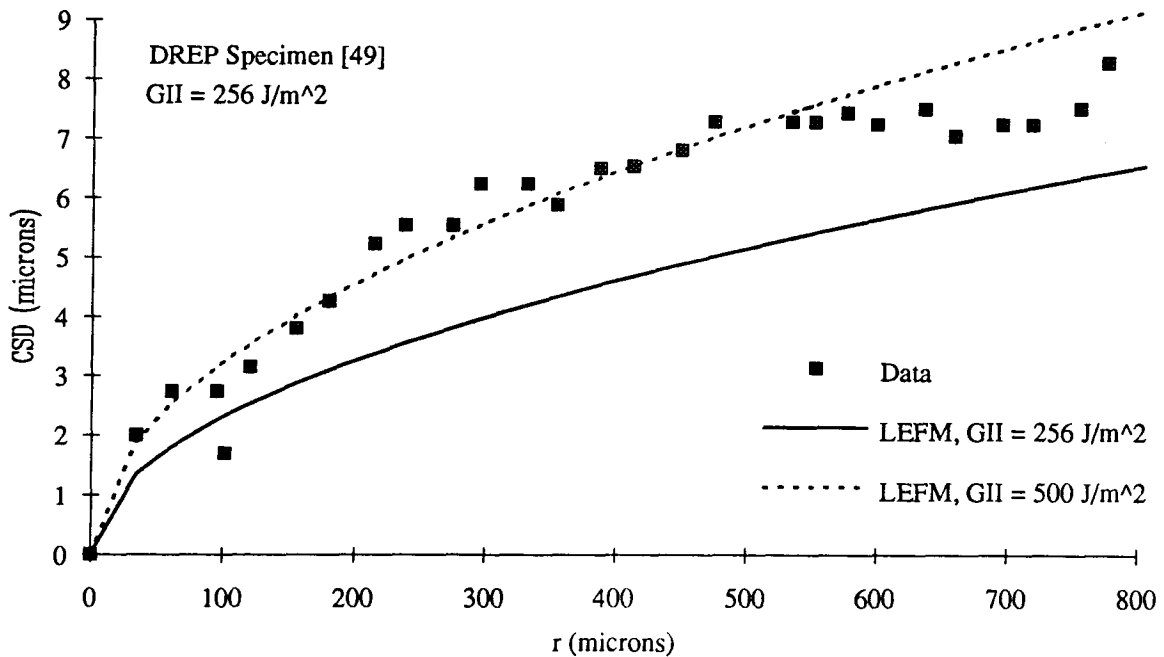


Fig. 5.25 - Plot of CSD vs  $r$  for an applied  $G_{II}$  of  $256 \text{ J/m}^2$  on a DREP specimen [49]. Solid line shows orthotropic prediction based on globally applied  $G$ . Dashed line represents best fit line and gives local  $G$  seen at the crack tip.

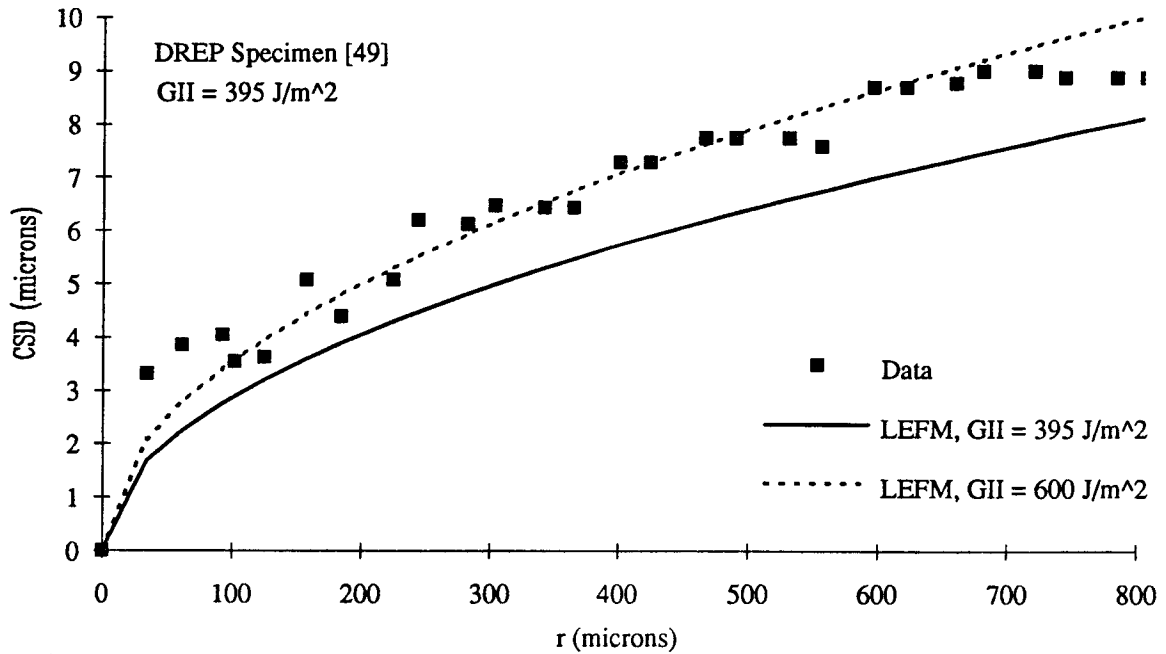


Fig. 5.26 - Plot of CSD vs  $r$  for an applied  $G_{II}$  of  $395 \text{ J/m}^2$  on a DREP specimen [49]. Solid line shows orthotropic prediction based on globally applied  $G$ . Dashed line represents best fit line and gives local  $G$  seen at the crack tip.

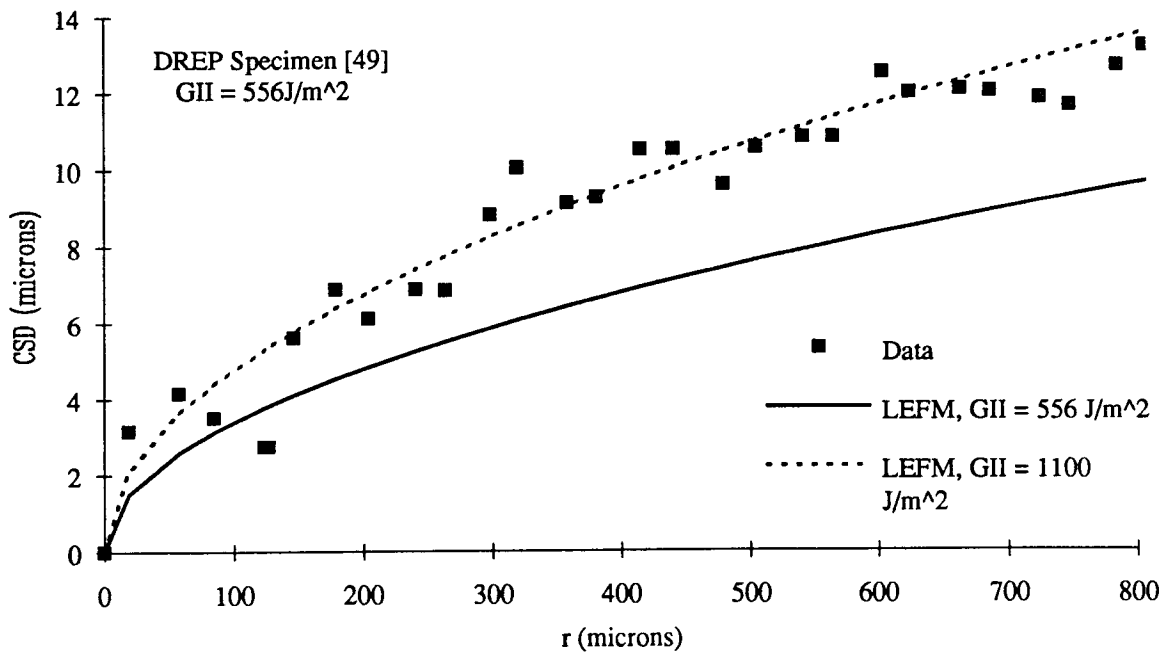


Fig. 5.27 - Plot of CSD vs  $r$  for an applied  $G_{II}$  of  $556 \text{ J/m}^2$  on a DREP specimen [49]. Solid line shows orthotropic prediction based on globally applied  $G$ . Dashed line represents best fit line and gives local  $G$  seen at the crack tip.

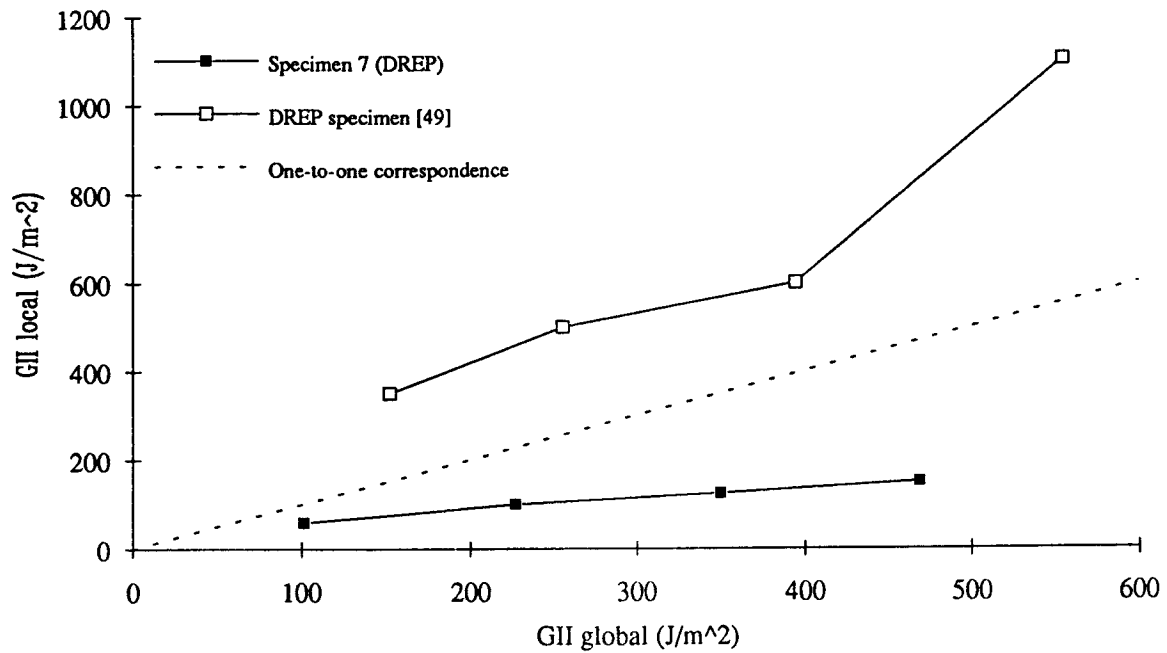


Fig. 5.28 - Plot of  $G_{II}$  local vs  $G_{II}$  global. Dashed line represents a 1-to-1 correspondence.

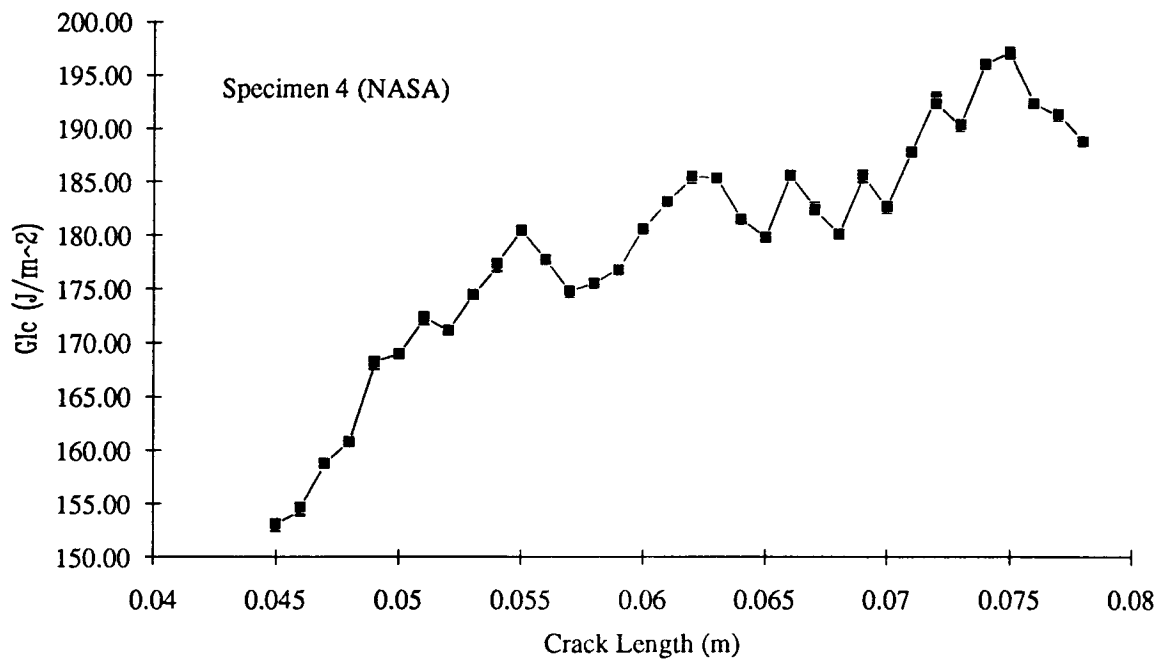


Fig. 5.29 - R-curve measured for a NASA specimen. This clearly shows the increase in  $G_{IC}$  as a function of crack growth.



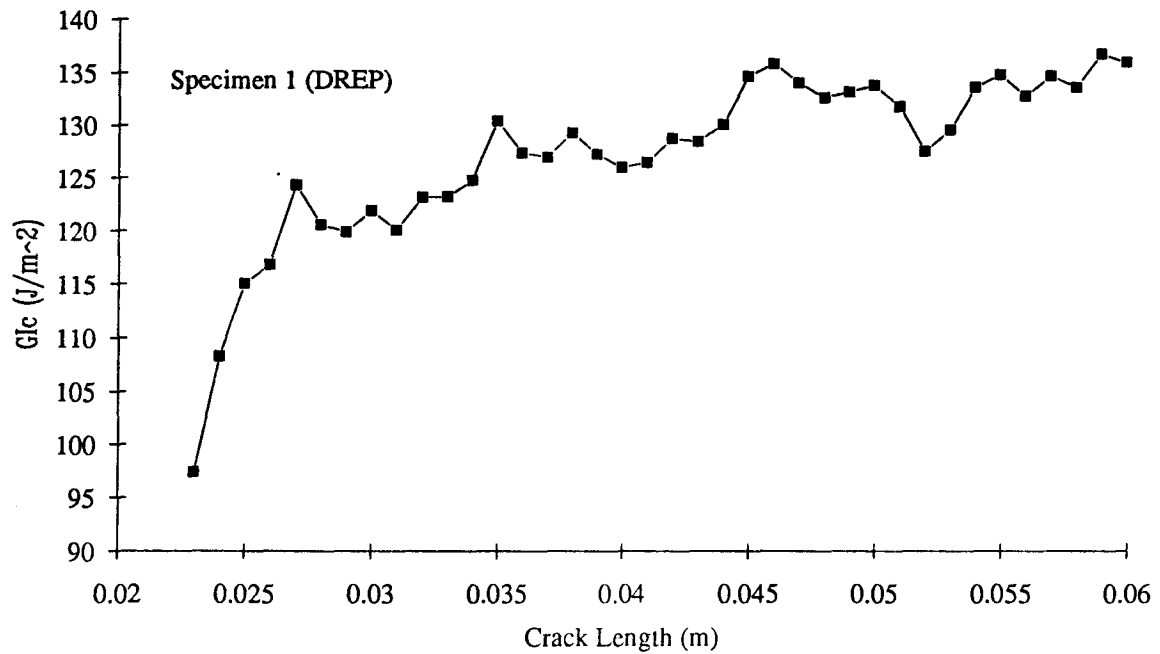


Fig. 5.30 - R-curve measured for a DREP specimen. This clearly shows the increase in  $G_{Ic}$  as a function of crack growth.

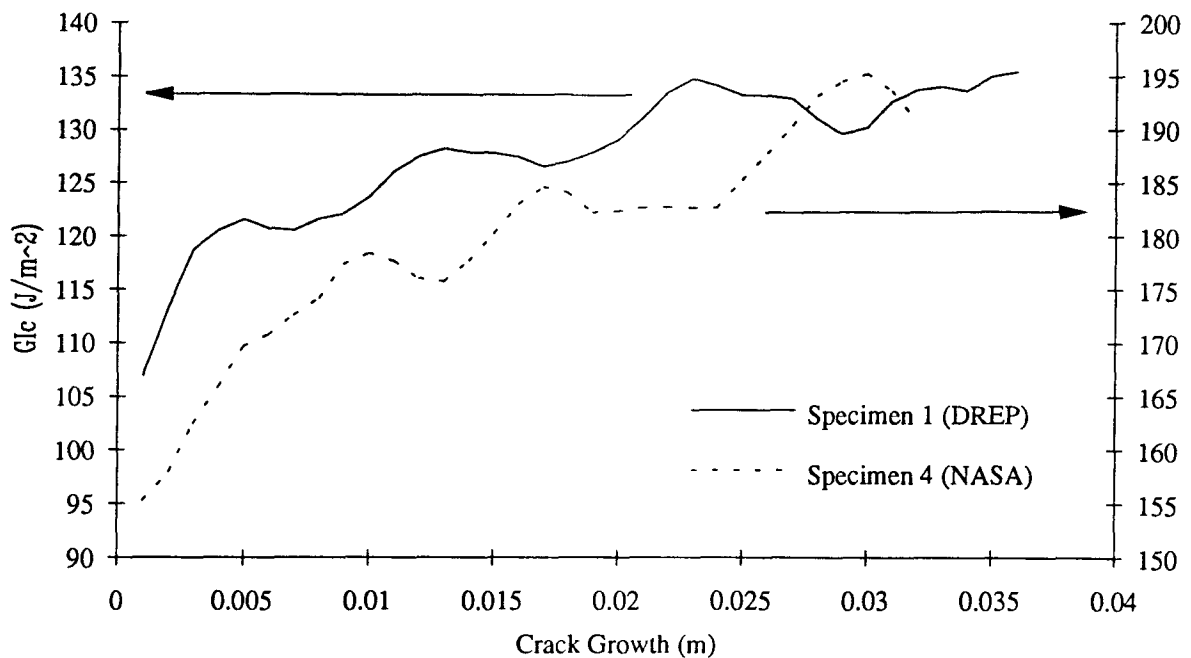


Fig. 5.31 - Combined plot of the two R-curves showing the difference in the rates of increase of  $G_{Ic}$  with crack growth for the specimens from different sources.

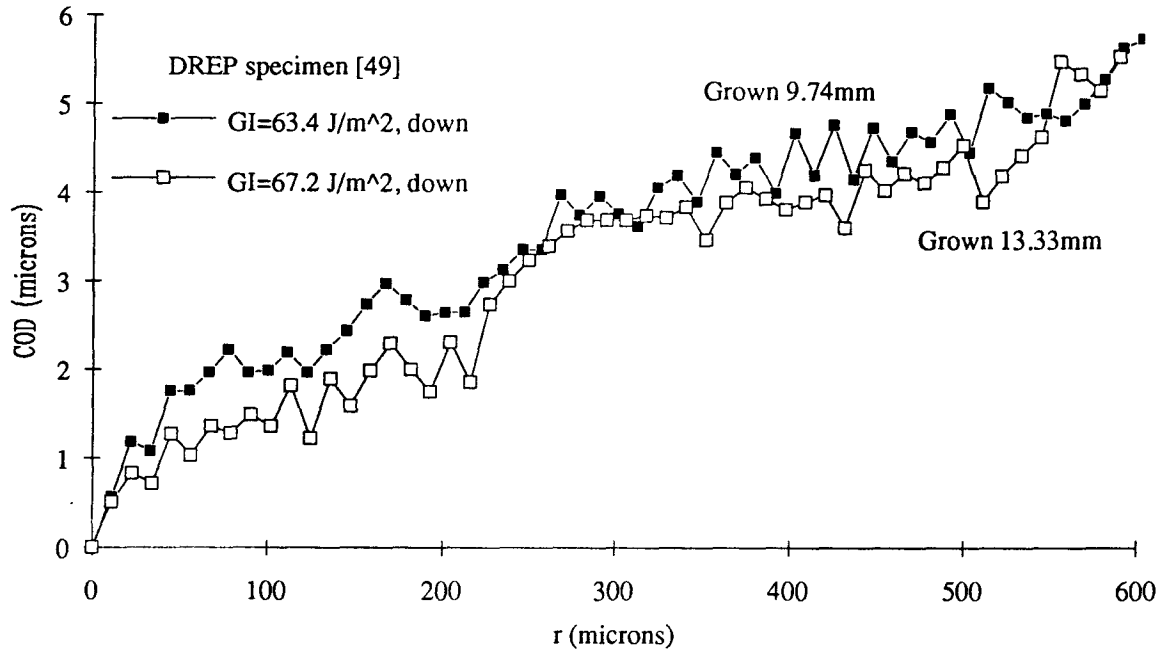


Fig. 5.32 - Plot of COD vs  $r$  containing data for two different crack lengths from a DREP specimen [49], with approximately the same  $G$  applied. In this case there is little difference in magnitude between the displacements.

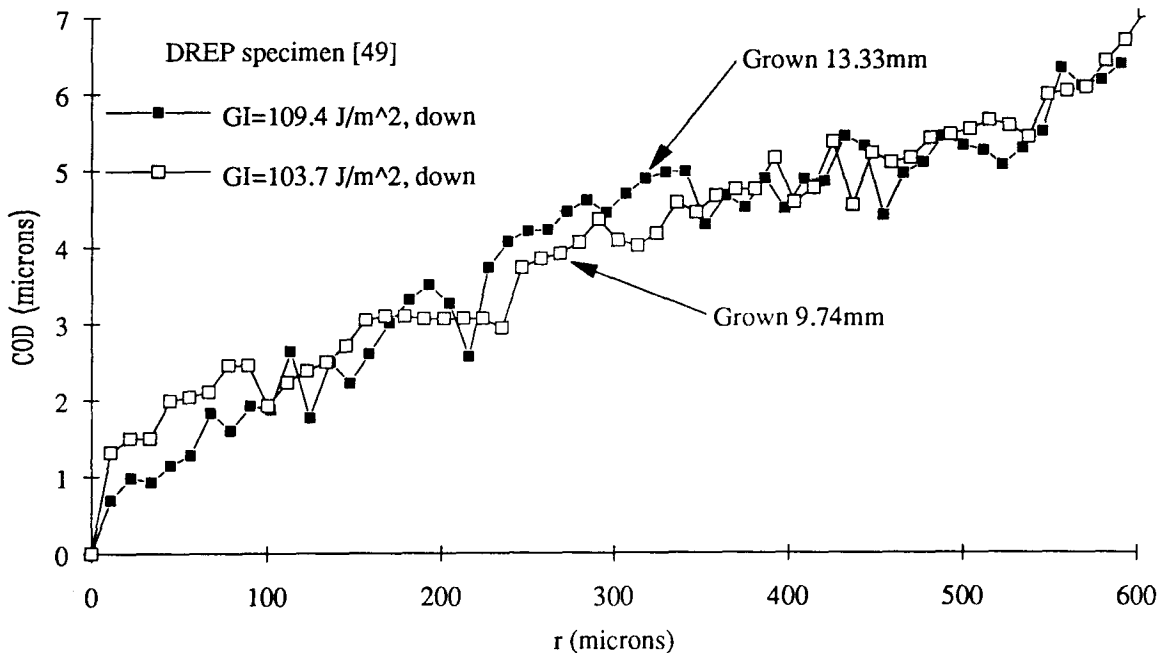


Fig. 5.33 - Plot of COD vs  $r$  containing data for two different crack lengths from a DREP specimen [49], with approximately the same  $G$  applied. In this case there is little difference in magnitude between the displacements.

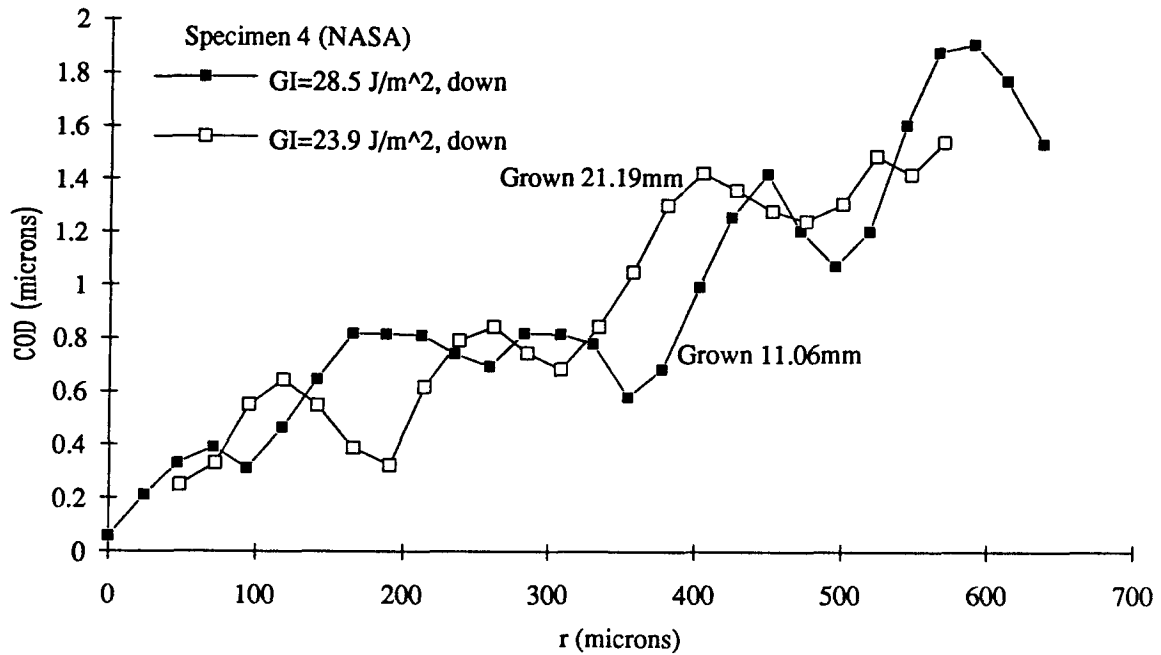


Fig. 5.34 - Plot of COD vs r containing data for two different crack lengths from specimen 4 (NASA), with approximately the same G applied. In this case there is little difference in magnitude between the displacements.

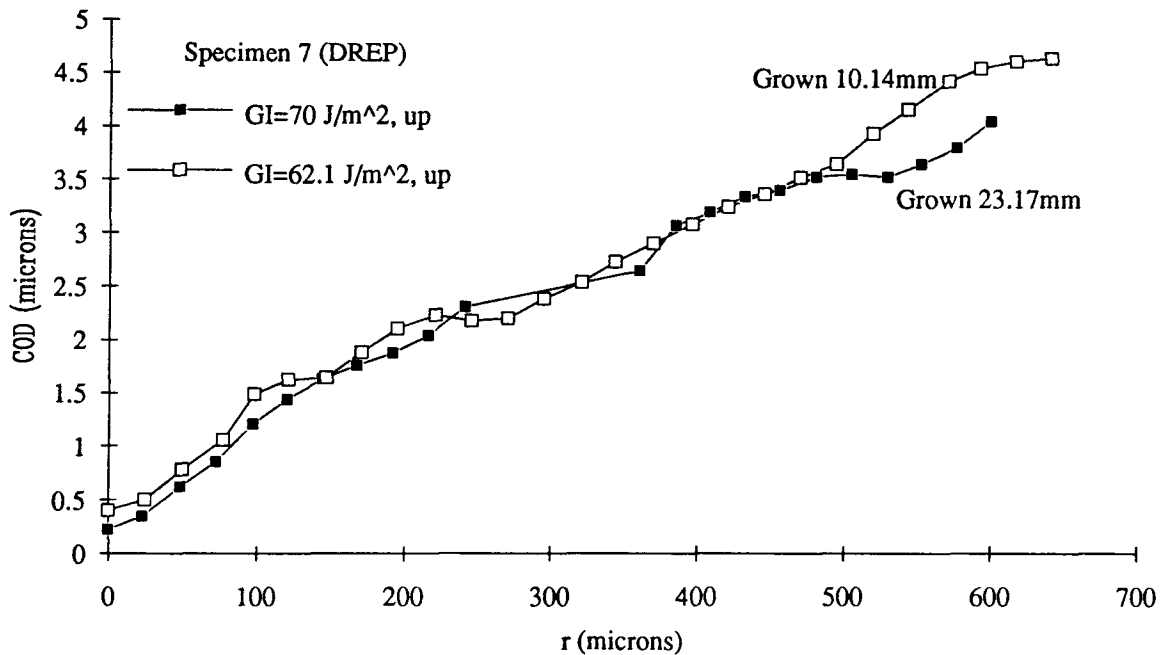


Fig. 5.35 - Plot of COD vs r containing data for two different crack lengths from specimen 7 (DREP), with approximately the same G applied. In this case there is little difference in magnitude between the displacements.

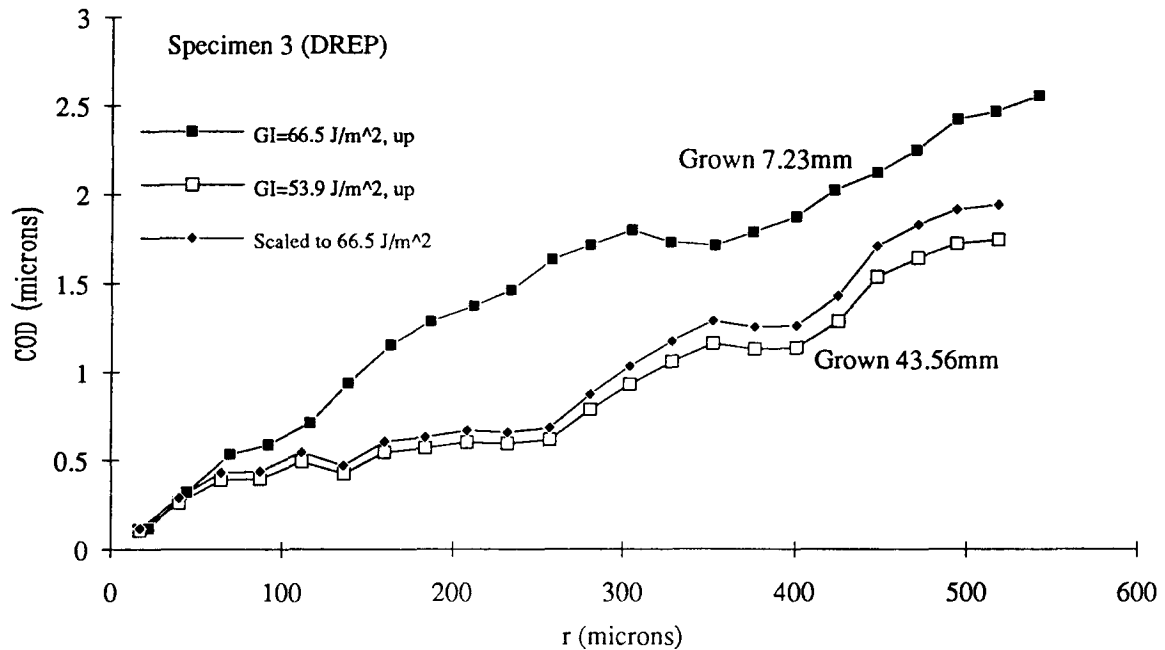


Fig. 5.36 - Plot of COD vs  $r$  containing data for two different crack lengths from specimen 3 (DREP). In this instance the smaller  $G$  has been scaled to the same magnitude as the larger  $G$ . The longer crack displays a smaller displacement field indicating more fibre bridging.

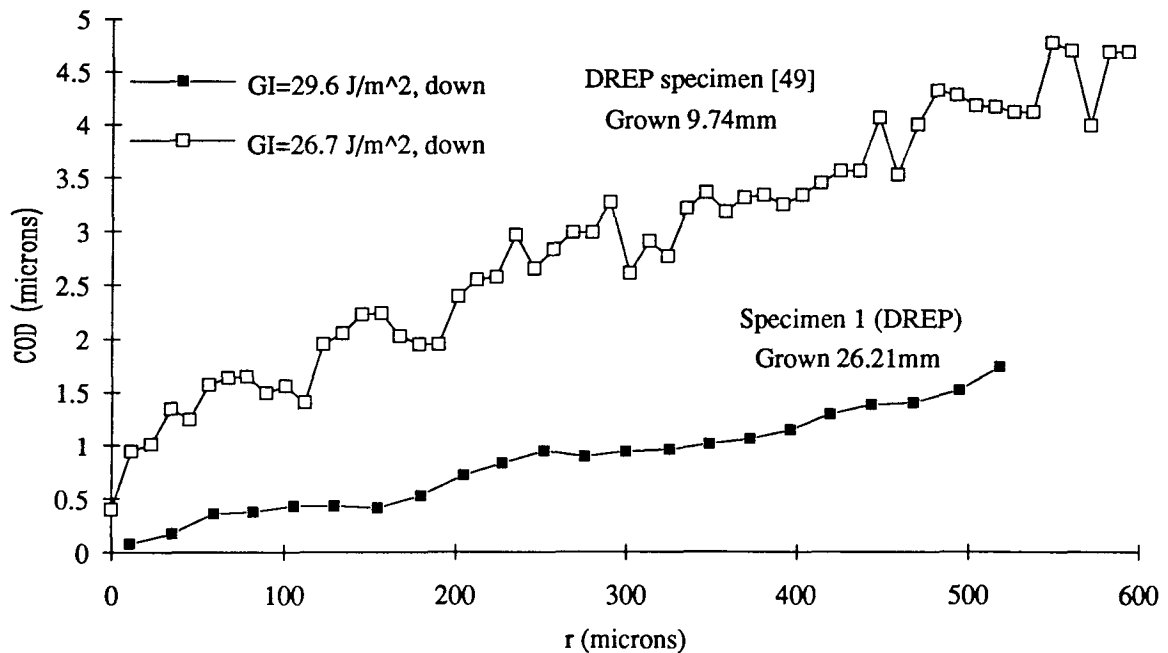


Fig. 5.37 - Plot of COD vs  $r$  containing data for two different crack lengths from specimens from the same manufacturer, with approximately the same applied  $G$ . The longer crack exhibits a smaller displacement indicating more fibre bridging.

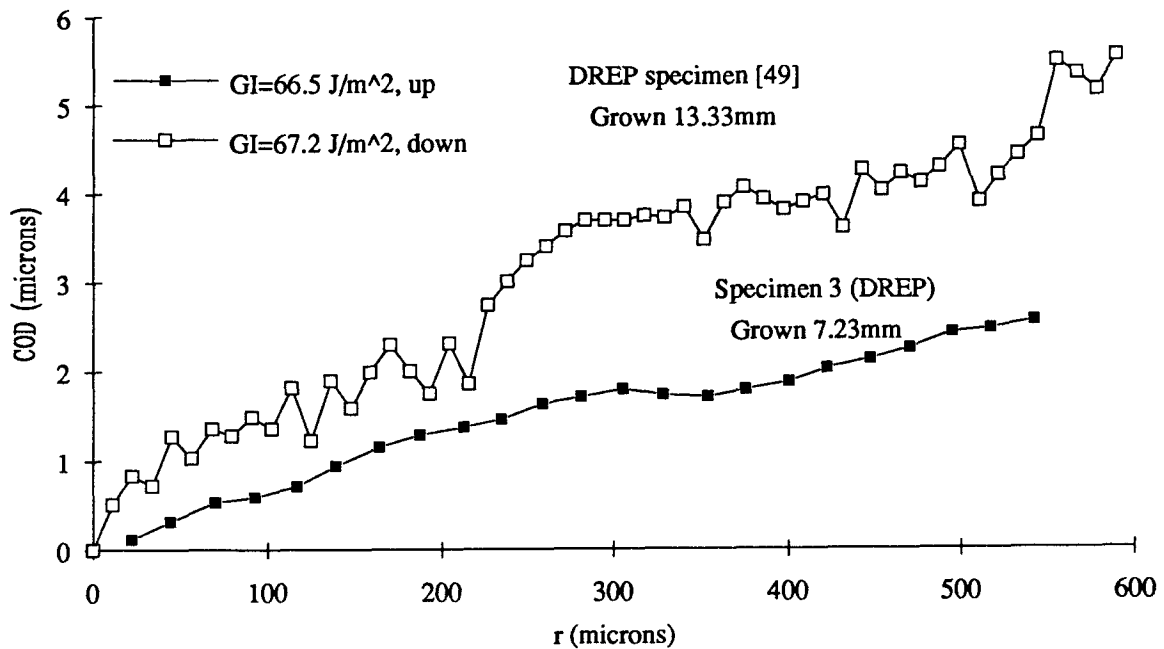


Fig. 5.38 - Plot of COD vs  $r$  containing data for two different crack lengths from specimens from the same manufacturer, with approximately the same applied  $G$ . The longer crack exhibits a smaller displacement indicating more fibre bridging.

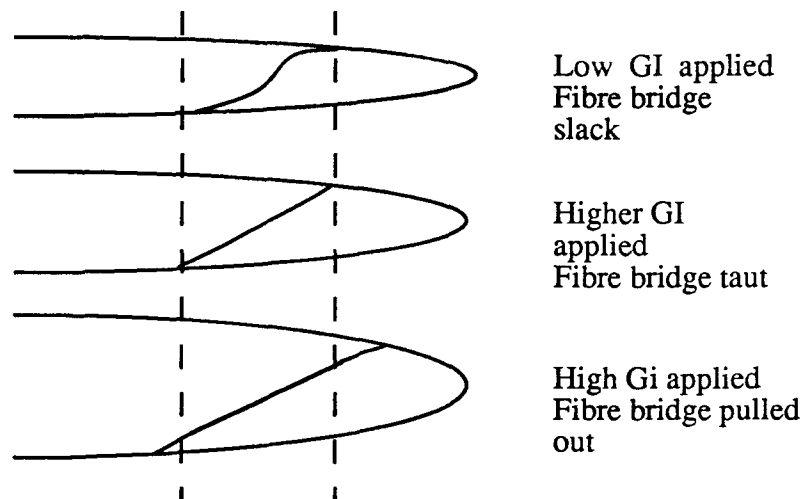


Fig. 5.39 - A schematic of a fibre bridge near the crack tip. At low  $G$  the bridge is slack and has little effect on the displacement. At higher  $G$  it becomes taut and essentially shields the tip from seeing the full applied load. At very high  $G$  the taut bridge is ripped from the matrix, both shielding the tip and consuming energy.

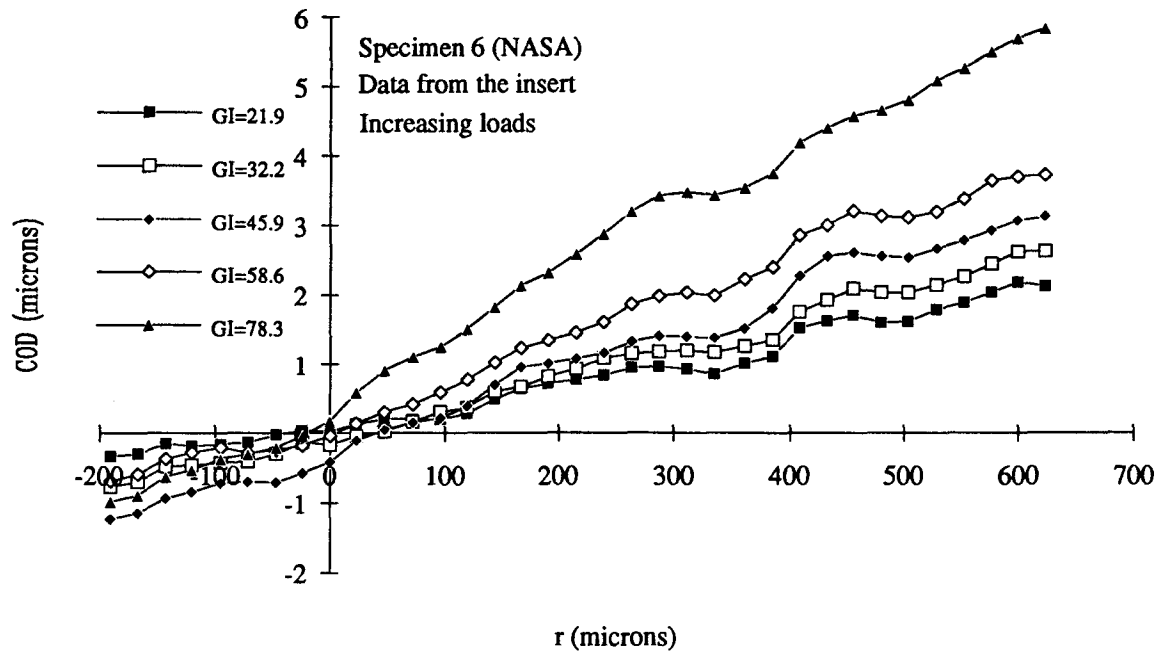


Fig. 5.40 - Plot of COD vs  $r$  for a series of increasing  $G$ s applied to specimen 6 (NASA) when there was no crack growth from the insert.

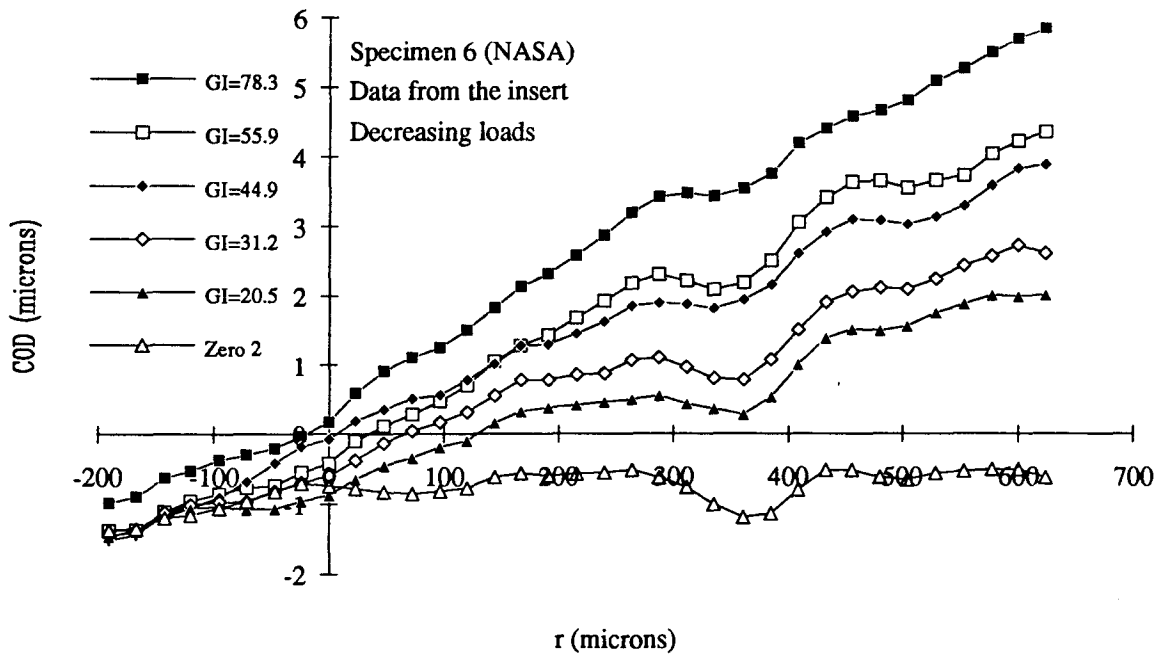


Fig. 5.41 - Plot of COD vs  $r$  for a series of decreasing  $G$ s applied to specimen 6 (NASA) when there was no crack growth from the insert.

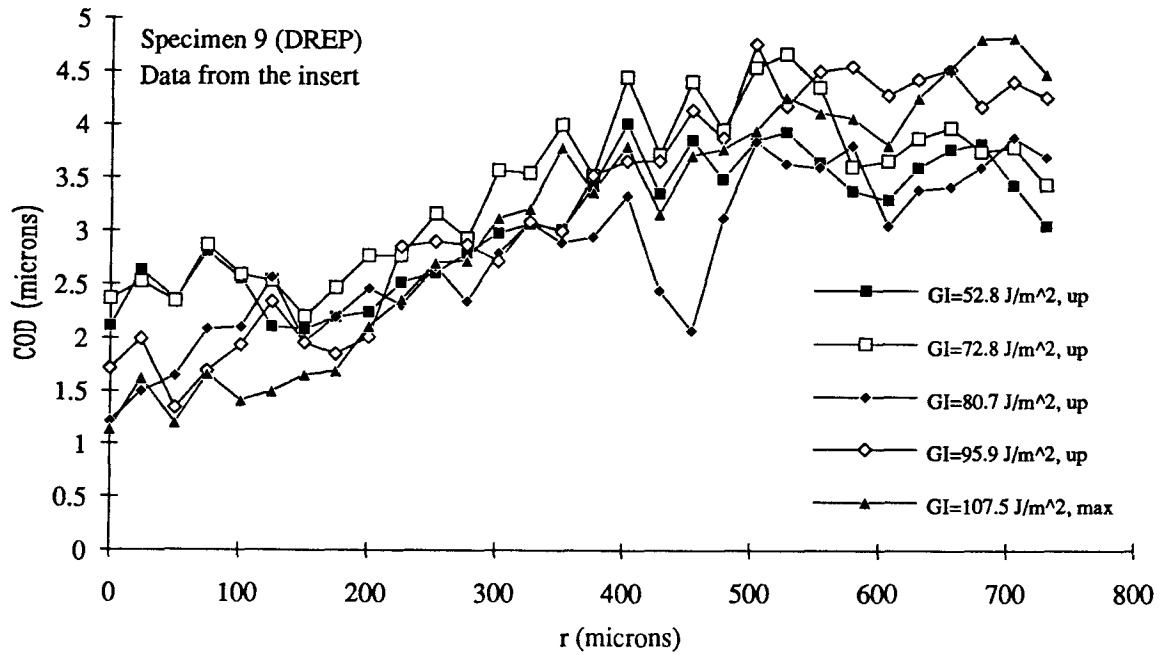


Fig. 5.42 - Plot of COD vs r for a series of increasing  $G_s$  applied to specimen 9 (DREP) when there was no crack growth from the insert.

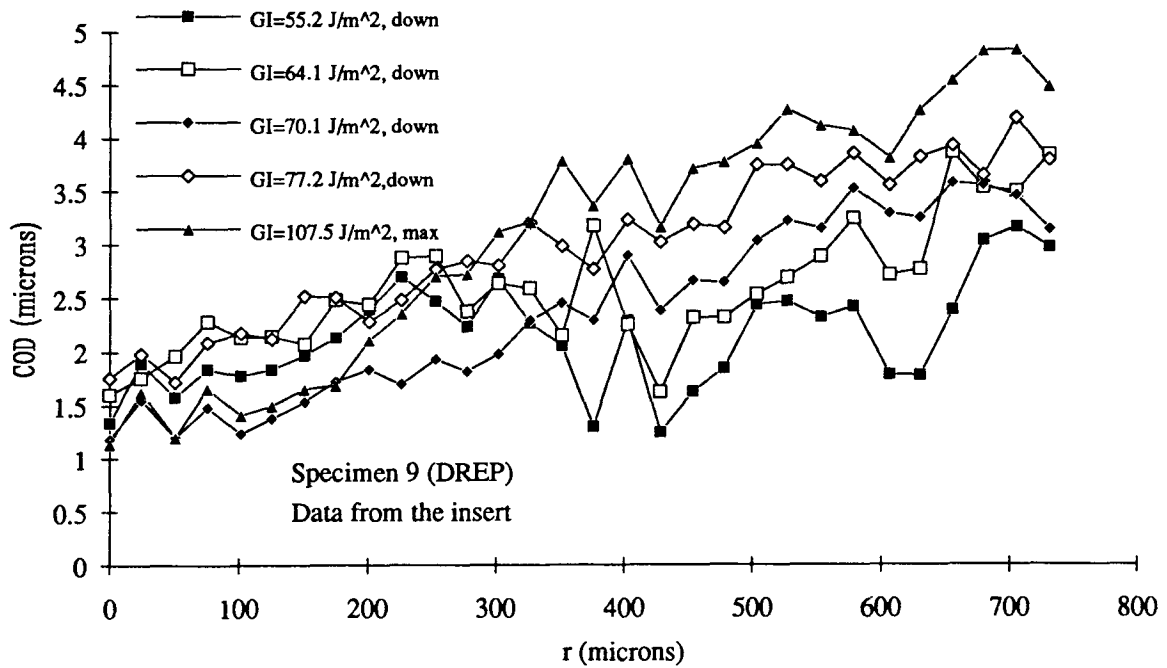


Fig. 5.43 - Plot of COD vs r for a series of decreasing  $G_s$  applied to specimen 9 (DREP) when there was no crack growth from the insert.

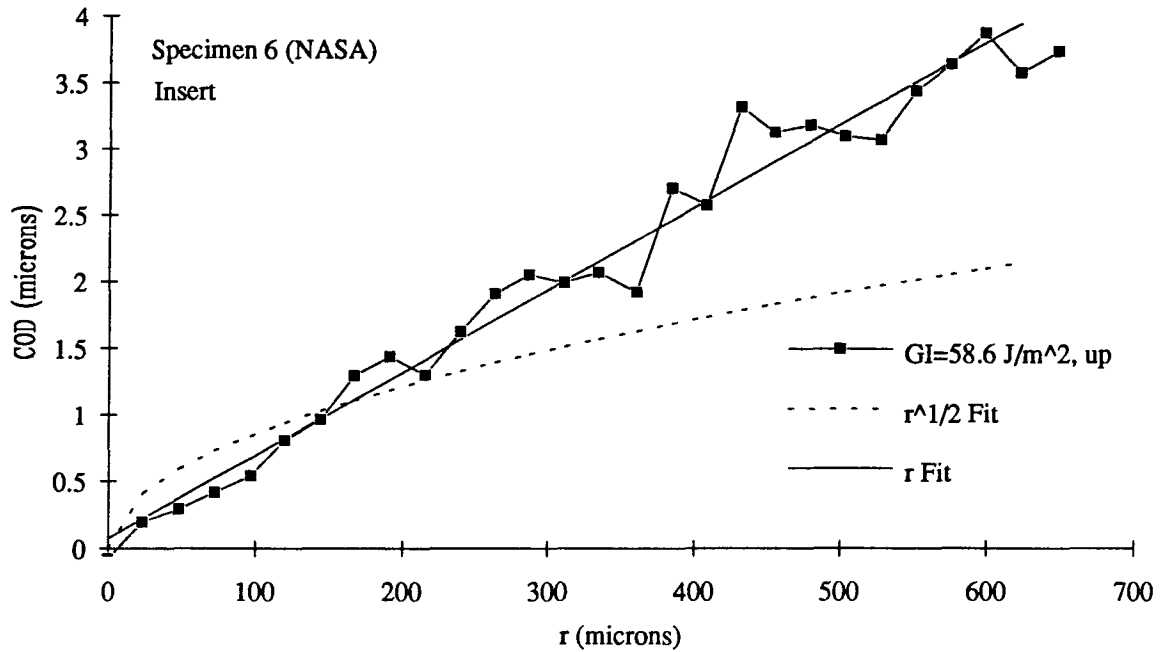


Fig. 5.44 - Plot of COD vs  $r$  from the specimen 6 (NASA) data at the insert, for an applied  $G_I$  of 58.6 J/m<sup>2</sup>. The solid line represents a linear fit vs  $r$ , while the dashed line is the expected fit vs  $r^{1/2}$ .

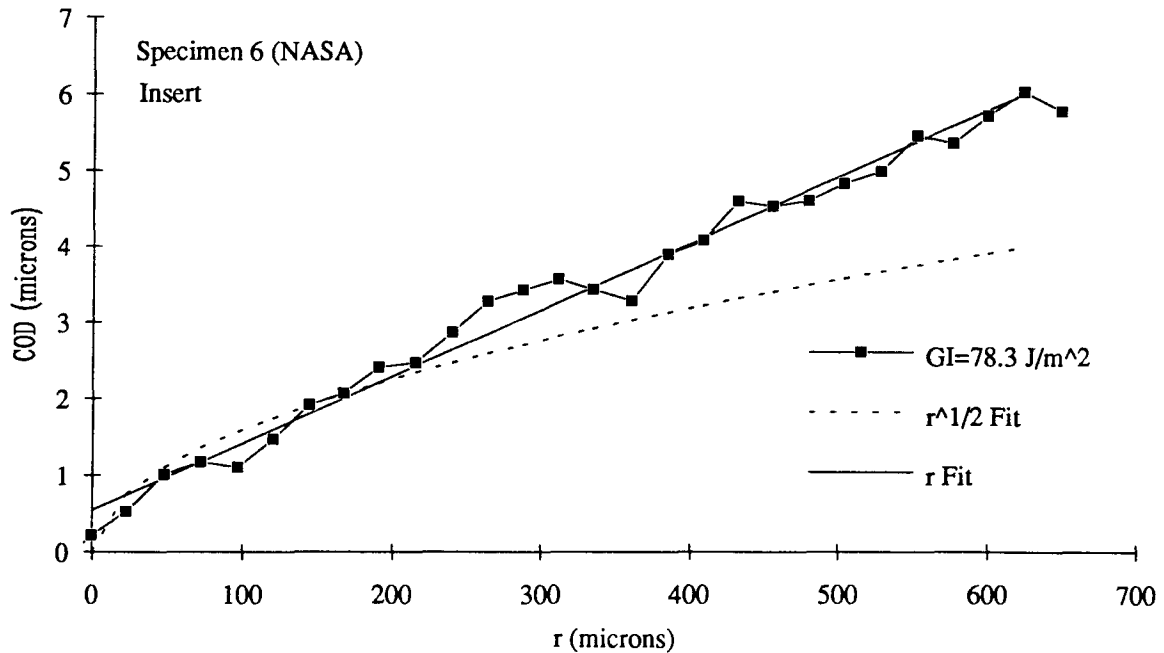


Fig. 5.45 - Plot of COD vs  $r$  from the specimen 6 (NASA) data at the insert, for an applied  $G_I$  of 78.3 J/m<sup>2</sup>. The solid line represents a linear fit vs  $r$ , while the dashed line is the expected fit vs  $r^{1/2}$ .



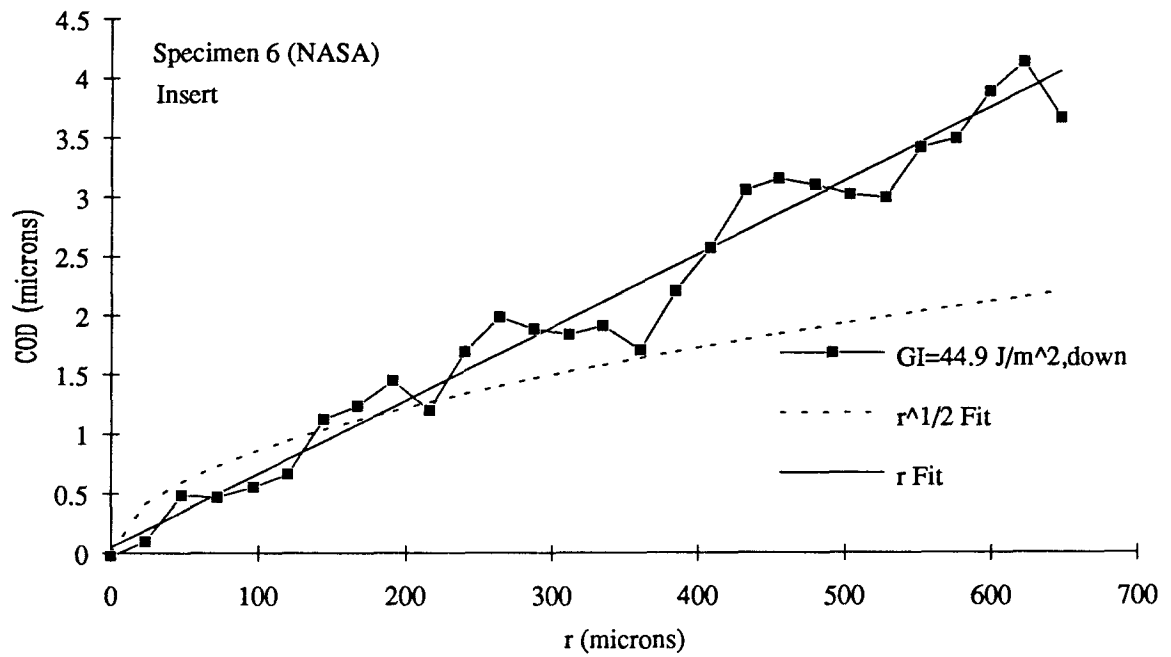


Fig. 5.46 - Plot of COD vs  $r$  from the specimen 6 (NASA) data at the insert, for an applied  $G_I$  of 44.9 J/m<sup>2</sup>. The solid line represents a linear fit vs  $r$ , while the dashed line is the expected fit vs  $r^{1/2}$ .

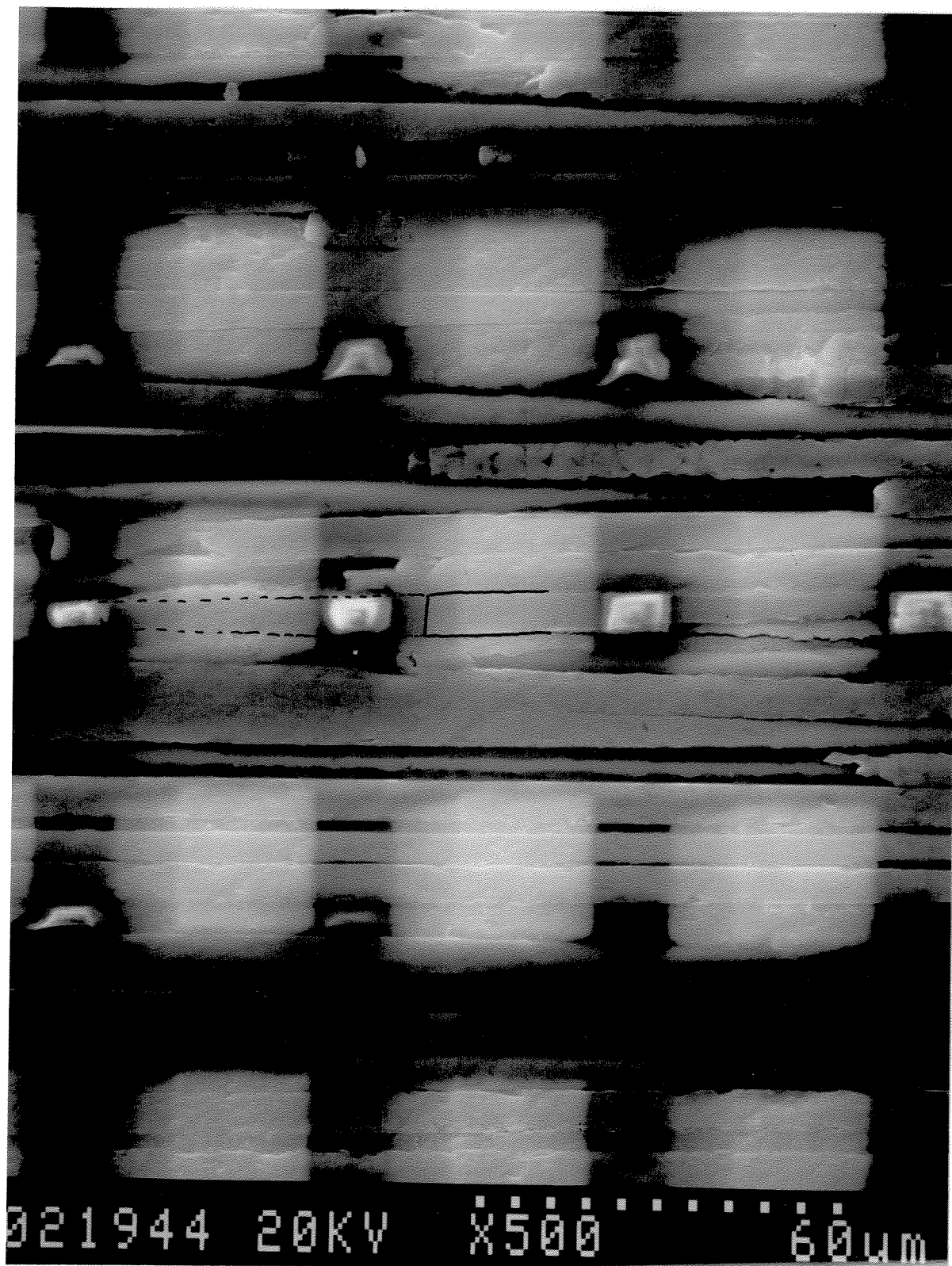


Fig. 5.47 - Photograph at the end of the insert in specimen 6. Note the blunt insert tip, and the small pocket of resin ahead of it.

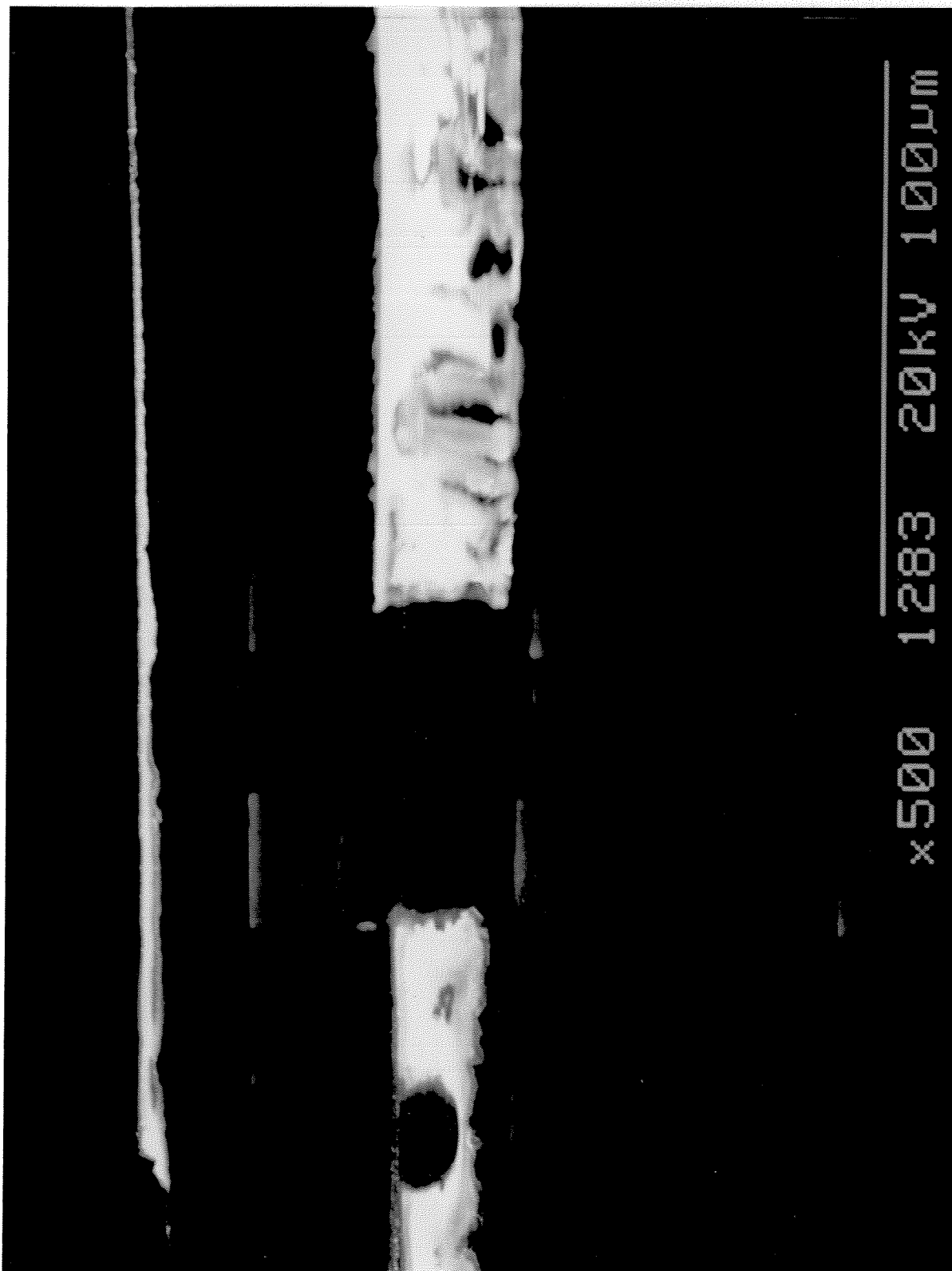


Fig. 5.48 - Photograph of the end of the insert in specimen 9. Note the blunt insert tip and the large resin pocket ahead.

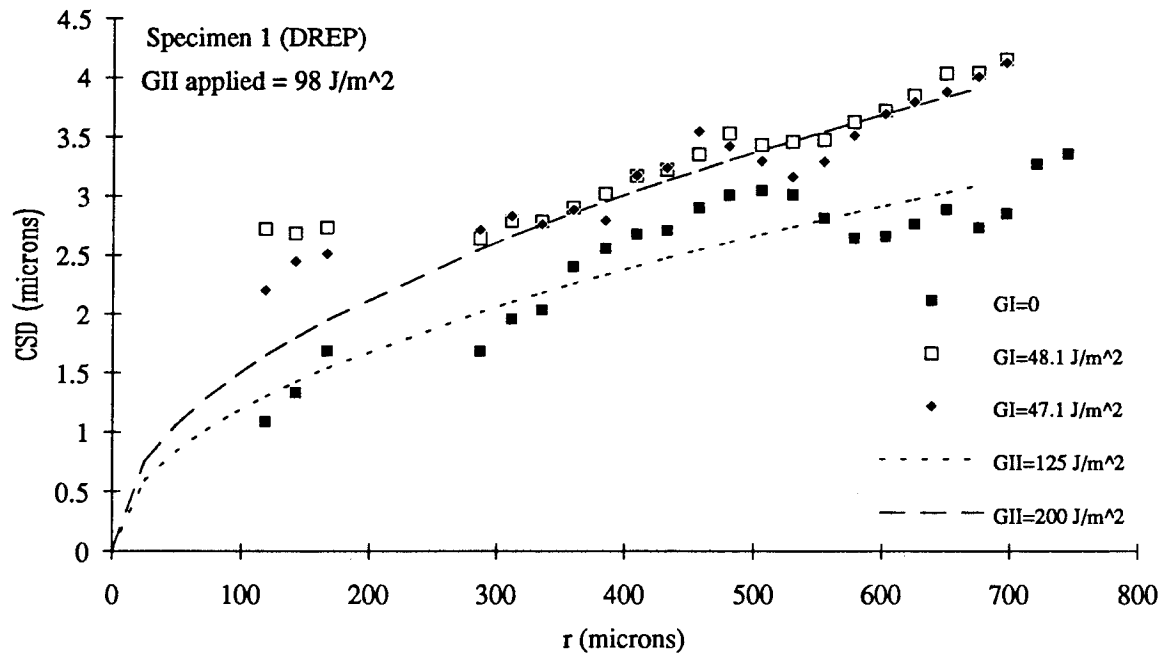


Fig. 5.49 - Plot of CSD vs  $r$  for pure Mode II and mixed Mode I and II loads on specimen 1 (DREP). This shows that CSDs increase under mixed-mode loading. Dashed lines represent best fit determinations of  $G_{II}$  local.

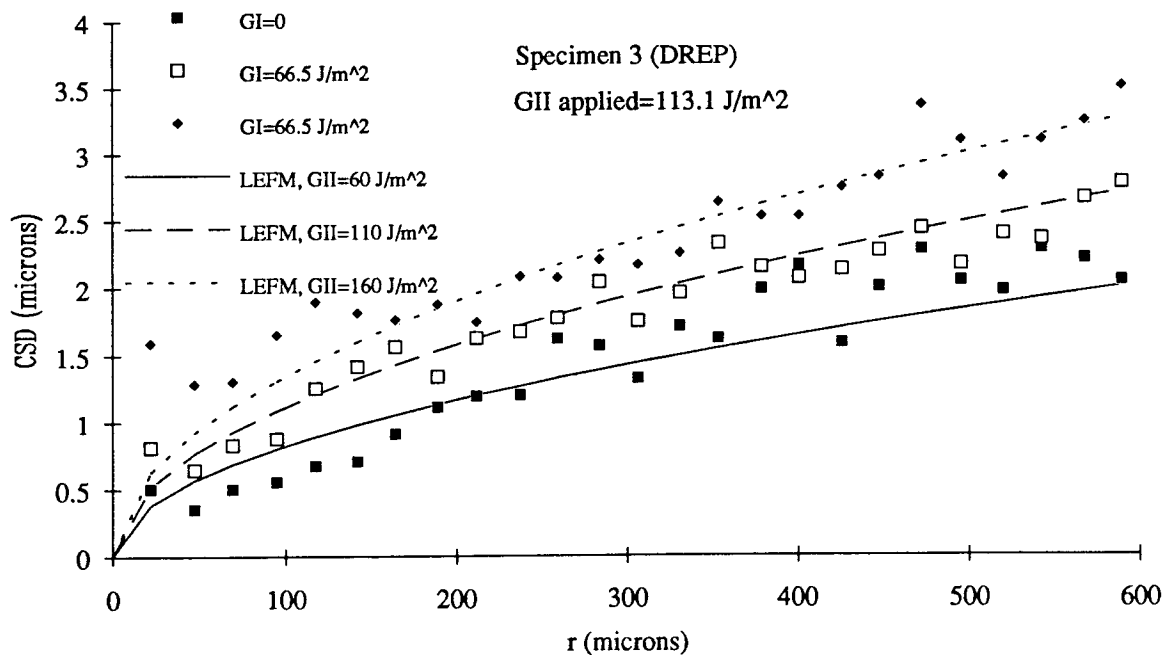


Fig. 5.50 - Plot of CSD vs  $r$  for pure Mode II and mixed Mode I and II loads on specimen 3 (DREP). This shows that CSDs increase under mixed-mode loading. Dashed lines represent best fit determinations of  $G_{II}$  local.

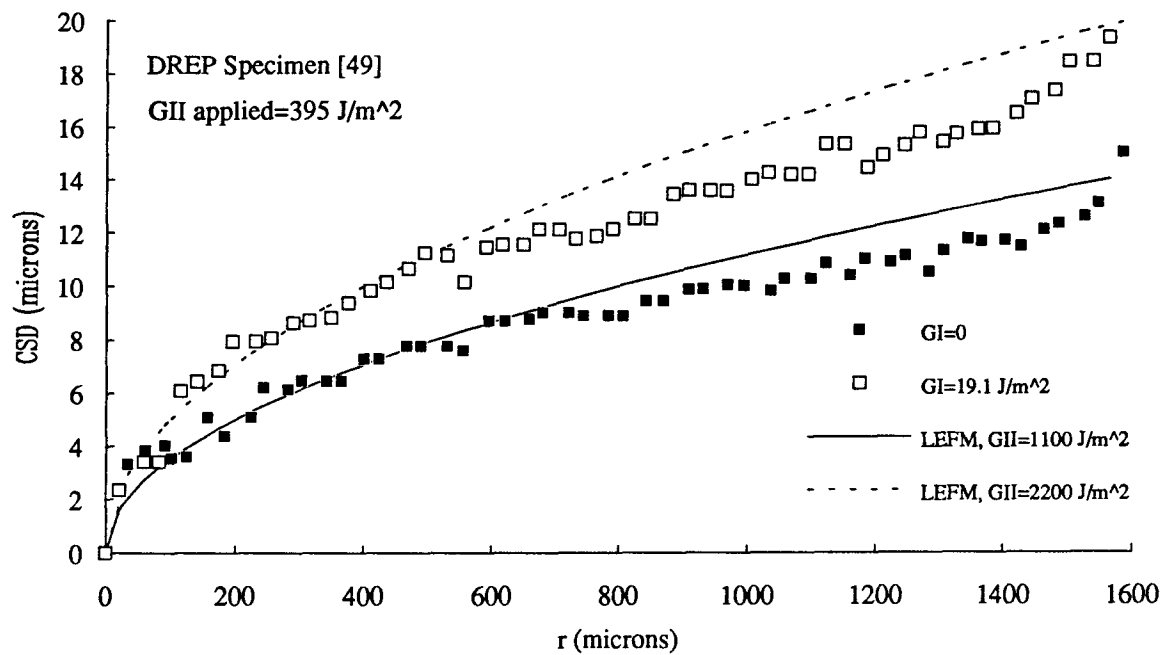


Fig. 5.51 - Plot of CSD vs  $r$  for pure Mode II and mixed Mode I and II loads on a DREP specimen [49]. This shows that CSDs increase under mixed-mode loading. Dashed lines represent best fit determinations of  $G_{II}$  local.

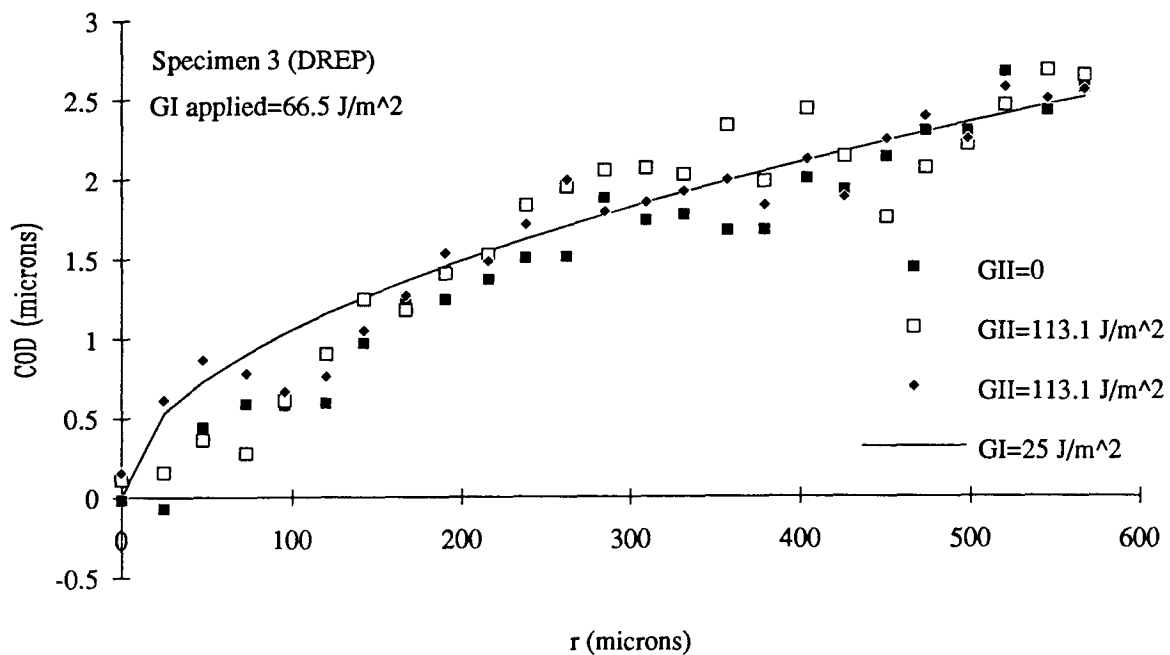


Fig. 5.52 - Plot of COD vs  $r$  for pure Mode I and mixed Mode I and II loads on specimen 3 (DREP). In this case there is no change in the magnitudes of the CODs in mixed-mode loading.

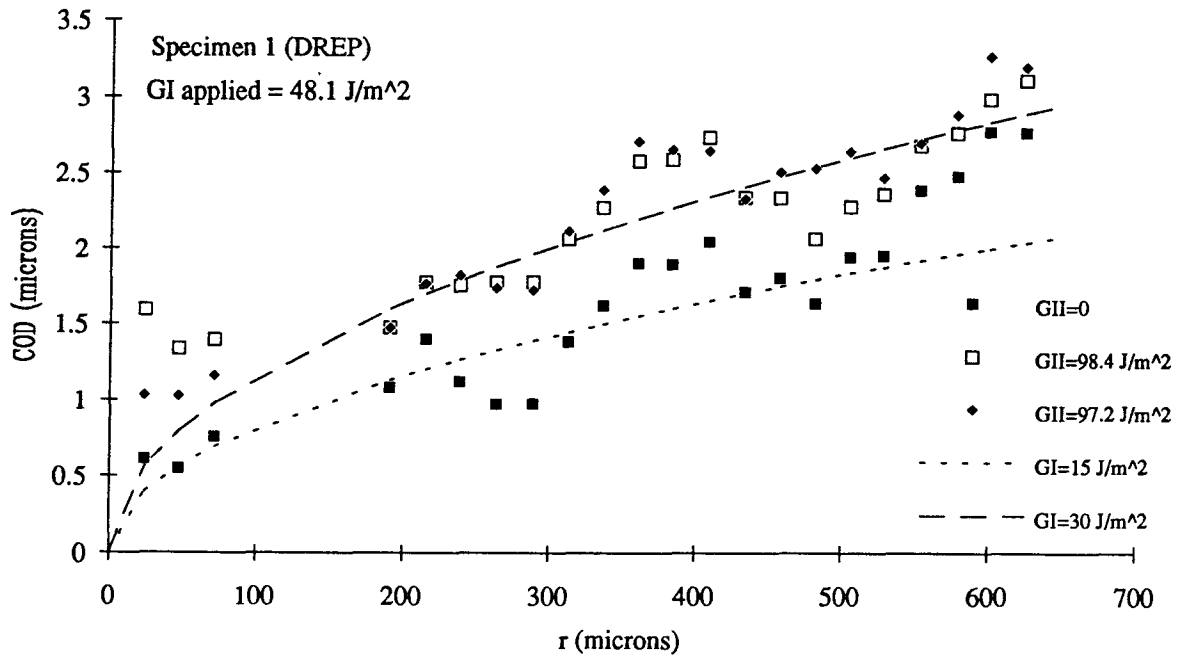


Fig. 5.53 - Plot of COD vs r for pure Mode I and mixed Mode I and II loads on specimen 1 (DREP). In this case the CODs increase in mixed-mode loading.

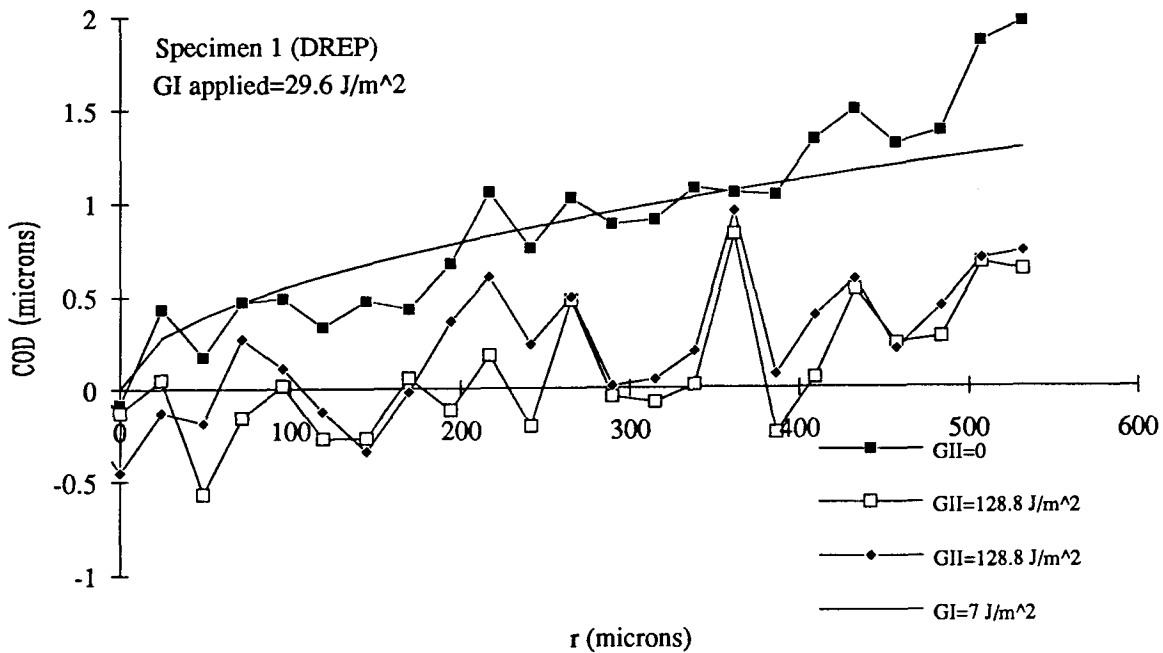


Fig. 5.54 - Plot of COD vs r for pure Mode I and mixed Mode I and II loads on specimen 1 (DREP). In this case the CODs decrease in mixed-mode loading.

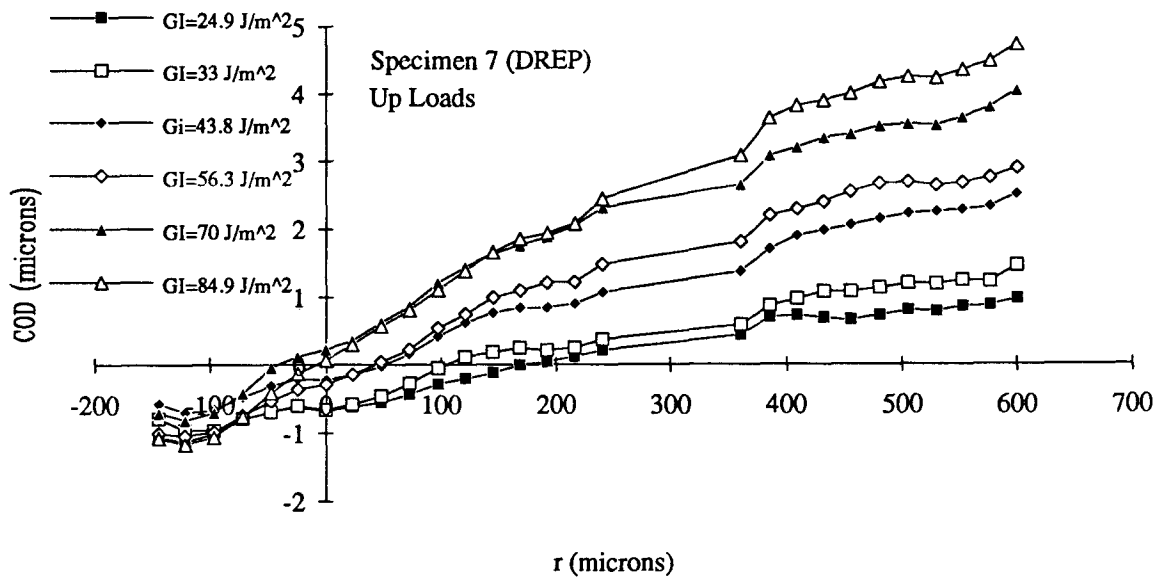


Fig. 5.55 - Plot of COD vs r for a series of increasing Mode I loads on specimen 7 (DREP). Note the apparent shift of the crack tip as the applied G is increased.

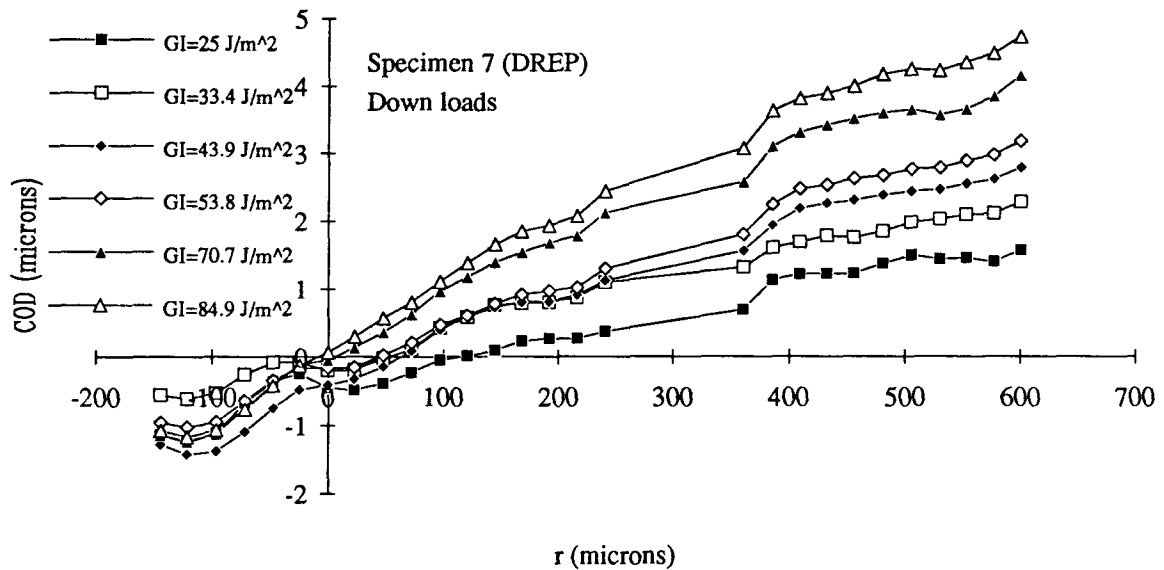


Fig. 5.56 - Plot of COD vs r for a series of decreasing Mode I loads on specimen 7 (DREP). Note that the crack tip appears to shift back to the right on the removal of the loads. This is similar to the crack closure phenomenon observed in metals.

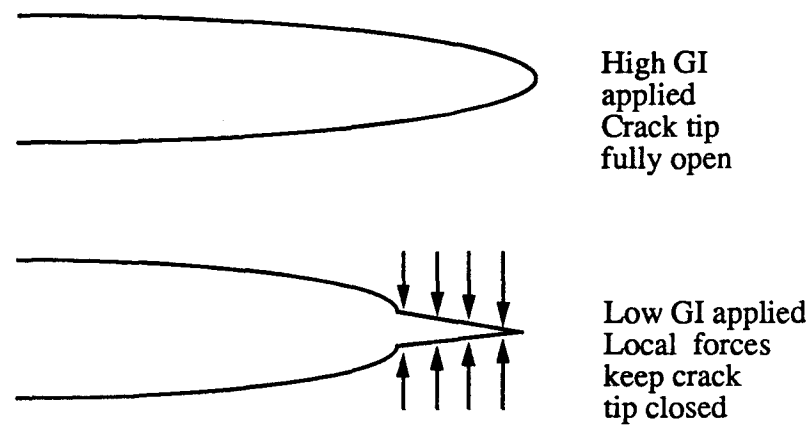


Fig. 5.57 - Schematic representation of the crack closure phenomenon where local forces, such as fibre bridges, may act to keep the crack tip closed at low loads.

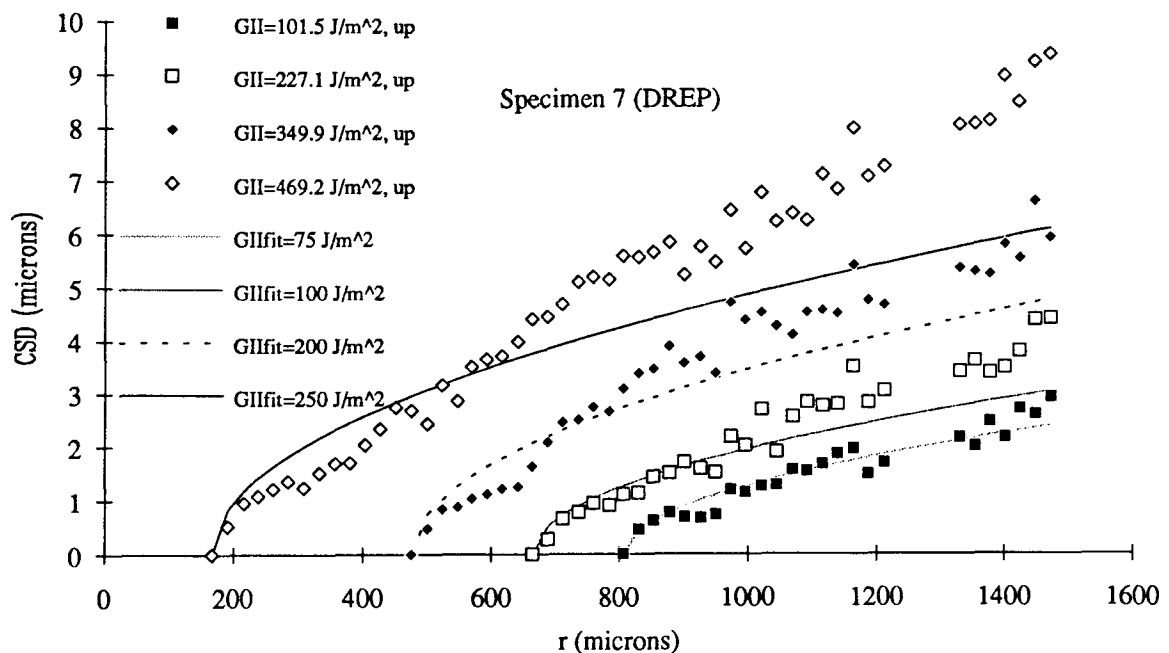


Fig. 5.58 - Plot of CSD vs  $r$  for increasing Mode II loads on specimen 7 (DREP). In this case there is subcritical crack growth taking place as the crack tip location remained constant during the subsequent unloading sequence. There was apparently also some static growth, as the crack tip moved from its position at 175 microns to the shown zero under constant applied  $G$  over a 48 hour period.



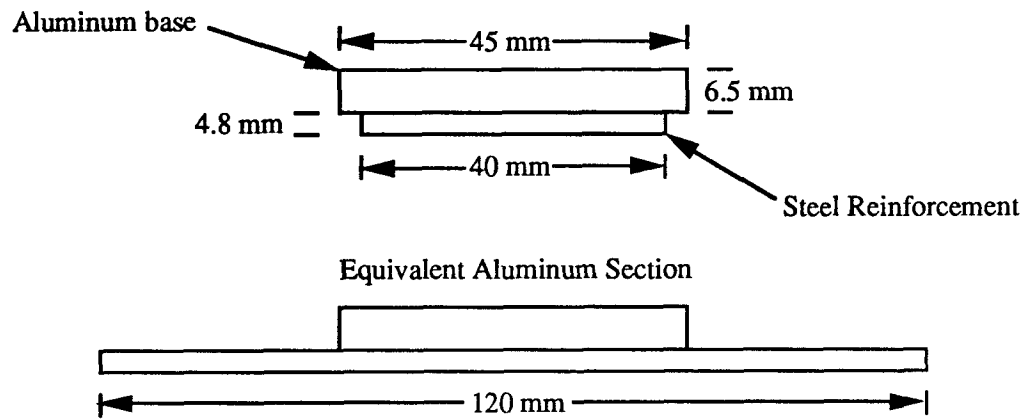


Fig. A2.1 - Schematic showing the actual dimensions of the base of the reinforced loading jig, and the equivalent sections used for calculating the base deflection correction.